

In-situ Structural Evolution of Polyurethane Elastomer under Deformation

Dissertation with the aim of achieving a doctoral degree
at the Faculty of Mathematics, Informatics and Natural Sciences

Department of Chemistry
of University Hamburg
submitted by Xuke Li

2015 in Hamburg

Date of oral defense: 28.08.2015

The following evaluators recommended the acceptance of the dissertation:

Prof. Dr. Almut Stribeck

Prof. Dr. Martin Trebbin

Nomenclature

[]	Slicing mapping
*	Convolution operator
1D	One-dimensional
2D	Two-dimensional
3D	Three-dimensional
$A(\mathbf{s})$	Scattering amplitude
$\rho(\mathbf{r})$	Electron density
SAXS	Small-angle X-ray scattering
WAXS	Wide-angle X-ray scattering
IDF	Interface distribution function
CDF	Chord distribution function
ε	Mechanical elongation ($\varepsilon = \ell/\ell_0 - 1$)
ℓ	In straining experiments: actual length of sample
ℓ_0	In straining experiments: initial length of sample
$I(\mathbf{s})$	Scattering intensity
Python	Open source programming language
$\mathbf{s} = (s_1, s_2, s_3)$	Scattering vector in Cartesian coordinates
s	Magnitude of the scattering vector
$\mathbf{r} = (r_1, r_2, r_3)$	Real space vector
$Q = k/V$	Invariant (SAXS)
PV-WAVE	Commercial programming system for image data processing
FFT	Fast Fourier transform
$\mathcal{F}_n()$	n -dimensional Fourier transform
$g_1(r_i)$	one-dimensional interface distribution function
$\gamma(\mathbf{r}) = \rho^{*2}(\mathbf{r})/k$	Normalized correlation function
BESSY	Berliner Elektronenspeicherring-Gesellschaft für Synchrotronstrahlung
Δ	Laplacian operator
∇	Gradient operator
λ	X-ray wavelength
DESY	Deutsches Elektronen-Synchrotron
L	Lattice repeat (in SAXS: long period or long spacing)
MDI	Methylene diphenyl diisocyanate
BD	1,4-Butanediol
PTHF	Polytetrahydrofuran
TOPAS	Scattering curve evaluation program by N. Stribeck
$z(\mathbf{r}) = -\Delta P(\mathbf{r})$	Chord distribution function
PUE	Polyurethane elastomer
PCL	Polycaprolactone

TPU	Thermoplastic Polyurethane
AFM	Atomic force microscopy
HSC	Hard segment content
TEM	Transmission electron microscopy
WAE	Well-arranged ensembles
PAR	Poorly-arranged region

Abstract

In this thesis, in-situ small-angle X-ray scattering (SAXS) is employed to track the nanostructure evolution of polyurethane elastomers during uni-axial stretching. Because various chemical components can be used to synthesize a polyurethane, it would be helpful to predict materials properties based on its composition and processing. Therefore mechanical and morphological data are collected in order to identify mechanisms of morphology evolution and their relation to mechanical properties. Chord distribution function (CDF) computed from the recorded SAXS pattern facilitates us to identify fundamental morphological features without having to apply a structural model. CDF visualizes the local structure in the neighborhood of a domain: Each peak shows, in which direction and distance neighbor domains are found that generate a long period. The integral of a peak is a measure of the population density. Furthermore, fitting interface distribution function (a meridian slice from the CDF) estimates the quantitative analysis of polyurethane morphology. The in-situ small-angle X-ray scattering is a versatile technique to track the structure evolution of polymer material under deformation.

Hand-cast thermoplastic polyurethanes exhibit broad distribution of hard domains and soft gaps. The hard domains are sacrificed with increasing the strain, the volume fraction v_h of hard domains can be determined as a function of strain and a simple empirical equation is found. This linear equation is valid for the 6 materials of different composition. It says that the materials break when all hard domains have been destroyed, i.e. $v_h(\varepsilon_b) = 0$ with ε_b the strain at break.

The hard domain content of machine-cast polyurethane which is aged at 150 °C decreases with increasing the ageing time. During stretching, the correlated hard domains in well-arranged ensembles (WAEs) are destructed into uncorrelated hard domains nested in poorly-arranged regions (PARs). All the hard domains are sacrificed to achieve the macroscopic elongation of material. The periodic stacks of hard domain and soft domain are extended up to a constant size, and then these outstretched entities are destructed without any further extension in order to achieve the macroscopic elongation.

The polyurethanes with multi-functionality (>3) polyols are thermosets that to be poorly phase separated whereas a 2-functional polyol is thermoplastic. The developed morphology and the deformation of the hard domains under stress are strongly depending on the architecture of polyol employed.

Zusammenfassung

In dieser Arbeit wird *in situ* Röntgenkleinwinkelstreuung (RKWS) eingesetzt, um die Nanostrukturentwicklung in Polyurethan-Elastomeren während der uniaxialen Dehnung zu verfolgen. Weil Polyurethane aus sehr verschiedenen chemischen Komponenten synthetisiert werden können, wäre es ein großer Fortschritt die Materialeigenschaften vorherzusagen zu können. Eine solche Vorhersage müsste die Zusammensetzung und das Herstellungsverfahren berücksichtigen. Deshalb werden hier mechanische und morphologische Daten zusammen getragen, um die Mechanismen der Morphologieentwicklung zu identifizieren und in Beziehung zu den mechanischen Eigenschaften zu stellen. Die Durchschusslängenfunktion (engl.: chord distribution function, (CDF)) wird aus den Streubildern berechnet. Sie ermöglicht es, fundamentale morphologische Parameter zu identifizieren, ohne ein Strukturmodell zu benutzen. Die CDF visualisiert die lokale Struktur in der Umgebung einer Domäne¹: Jeder Peak zeigt, in welcher Richtung und Entfernung sich Nachbardomänen befinden, die den Langperiodenpeak der RKWS erzeugen. Das Integral des CDF-Peaks ist ein Maß für die Besetzungsdichte. Darüber hinaus werden Morphologie-Parameter quantitativ bestimmt. Dazu wird die Grenzflächenverteilung (engl.: interface distribution function (IDF)) ausgewertet. Die IDF ist der meridionale Schnitt durch die CDF. Für Polymermaterialien ist die *in situ* RKWS eine mächtige Methode zur Verfolgung der Strukturevolution während der Dehnung.

Handgegossene thermoplastische Polyurethane (TPU) zeigen breite Verteilungen von Hartdomänengrößen und Weichphasenlücken. Beim Dehnen werden die Hartdomänen zunehmend zerstört, der Volumenanteil v_h kann als Funktion der Dehnung bestimmt werden. Hierfür wird eine einfache empirische Gleichung gefunden. Diese lineare Gleichung ist gültig für alle 6 untersuchten Materialien, bei denen die Zusammensetzung stark variiert. Die Aussage der Gleichung ist, dass die Materialien zerreißen, sobald alle Hartdomänen zerstört sind, d. h. $v_h(\varepsilon_b) = 0$, wobei ε_b die makroskopische Bruchdehnung ist.

Der Hartdomänenanteil von maschinengegossenem Polyurethan, welches bei 150 °C gealtert ist, nimmt mit der Alterungszeit ab. Beim Dehnen werden Hartdomänen aus gut geordneten Ensembles (engl.: well-arranged ensembles (WAEs)) in Mitleidenschaft gezogen. Dabei geht die Regelmäßigkeit der Anordnung zu ihren Nachbarn verloren und sie gehören danach zu den schlecht geordneten Ensembles, die nur Partikelstreuung zeigen. Die makroskopische Dehnung erfolgt unter Zerstörung der Hartdomänen. Periodische Stapel von Hart- und Weichdomänen sind bis zu einem gewissen Grad dehnbar. Danach werden die ausgestreckten Entitäten zerstört.

Polyurethane, die Polyole mit Mehrfachfunktionalität (> 3) enthalten zeigen eine schlechte Phasenseparation. Die Materialien sind Thermosets. Nur das 2-funktionale Material ist thermoplastisch. Die ausgebildeten Morphologien und das Deformationsverhalten der Hartdomänen hängen sehr stark von der Polyolarchitektur ab.

¹Die Morphologie von Polyurethan wird durch Hartdomänen erzeugt, die in einer Weichphase eingebettet sind

Contents

Nonmenclature	i
Abstract	iii
Zusammenfassung	v
1 Motivation and Objectives	1
2 Background Knowledge	3
2.1 Research Status of PUE	4
2.1.1 Nanostructure of PUE	4
2.1.2 Nanostructural Evolution under Load	6
2.1.3 PUE Ageing	8
2.1.4 Cross-linked PUE	11
2.2 Knowledge of SAXS	13
2.2.1 Magic Square of SAXS	14
2.2.2 Methods of Data Evaluation	15
2.2.2.1 Model-free	15
2.2.2.2 Fitting with Ideal Model	22
2.3 Comprehending the Magic Square	24
2.3.1 Fourier Transform	24
2.3.1.1 Projection-slice Theorem	25
2.3.1.2 Spatial Frequency Filter	27
2.3.2 Gradient	28
2.3.3 Comparison of Convolution and Correlation Function	28
2.3.4 Lorentz Correction	29
3 Experimental	31
3.1 Materials	31
3.1.1 Materials Investigated in Section 4.1	31
3.1.2 Materials Investigated in Section 4.2	31
3.1.3 Materials Investigated in Section 4.3	32
3.2 Wide Angle X-ray Scattering	34
3.3 Transmission Electron Microscopy	34
3.4 Fourier Transform Infrared Spectroscopy (FTIR)	34
3.5 Tensile Testing	34
3.5.1 Tensile Testing at DESY	34

3.5.2	Tensile Testing at BESSY II	35
3.6	SAXS Setup	36
3.6.1	Experiments Carried out at DESY	36
3.6.2	Experiments Carried out at BESSY II	36
3.7	Data Evaluation	37
3.8	Code	41
4	Results and Discussion	43
4.1	Morphology Variation of TPUs Monitored by SAXS Related to Strain-at-break	43
4.1.1	Properties of the TPU Materials	43
4.1.2	Tensile Tests	44
4.1.3	TEM	44
4.1.4	Wide-angle X-ray Scattering Scans	45
4.1.5	SAXS Data Accumulated during the Tests	46
4.1.6	Nanostructure from CDF Analysis	48
4.1.7	Bonart's Longitudinal Scattering	51
4.1.8	Conclusion	60
4.2	Ageing Effect on Morphological Evolution of PUE under Strain	61
4.2.1	Mechanical Performance	61
4.2.2	Screening the SAXS Data from the Straining Experiments	61
4.2.3	Quantitative Analysis of the SAXS Data	65
4.2.4	Conclusion	69
4.3	Failure Mechanisms of Crosslinked PUE with Poorly Developed Domain Structure	69
4.3.1	Amorphous Materials	70
4.3.2	Stress-strain Curve	70
4.3.3	Features of the SAXS Patterns Related to Strain and Material	70
4.3.4	Long Periods	74
4.3.5	Lateral Hard Domain Extension	75
4.3.6	Analysis of Bonart's Longitudinal Structure	75
4.3.7	Polyol Architecture and Microstructure	80
4.3.8	Conclusion	81
5	Summary and Outlook	83
	Bibliography	96
	List of Hazardous Substances	97
	Curriculum Vitae	101
	Publications	103
	Acknowledgments	105

1 Motivation and Objectives

The structure-property relationship assists material scientists in design, synthesis and processing of new material, in particular, polymer material. The polyurethane elastomer (PUE), which combines the properties of rubber and plastics, has been developed since 1937 by Otto Bayer and his coworkers. By altering types of diisocyanates, chain extenders and polyols, and their proportion, numerous types of polyurethane are synthesized. The isocyanate and short-chain diol form a rigid or hard segment. Correspondingly, the polyol forms soft segment. Because of the thermodynamic incompatibility between hard segments and soft segments, the PUE exhibits micro-phase separated morphology of hard domains (aggregation of hard segment) and soft domains (aggregation of soft segment or single diisocyanate). The morphology of PUE could affect material performance under load, such as thermal load, ageing load, mechanical load, environmental load. How the PUE morphology varies under mechanical load is still an unsolved problem when the PUEs have different chemical constituents.

PUE presents multiphase morphology and the inhomogeneity of multiphase morphology is in the tens of nanometer scale. The morphology variation under mechanical load has been investigated by small-angle X-ray scattering (SAXS) by Bonart et al.[1, 2, 3, 4] from several decades ago. In the past, polymer scientists only can measure the static or quasi-static morphology because of low intensity of the laboratory X-ray source. Today, high brilliance X-ray is generated from synchrotron radiation source, it facilitates to collect SAXS pattern with a high signal-to-noise ratio and to track the in-situ morphology evolution under fast strain.

The improvement of X-ray brilliance enhances the track of morphology evolution under strain, the SAXS data evaluation procedures developed in Stribeck's group (chord distribution function) broaden the morphology information extracted from the SAXS pattern. The chord distribution function (CDF) visualizes the local structure in the 2D neighborhood of a domain.[5] CDF could assist to gain an insight into morphology evolution with ease. The procedures to evaluate data are written in the commercial programming language PV-WAVE. These procedures have been converted into open-source and high-level programming language Python codes by the author in order to share the procedures of data processing in the research community.

Based on the development of hardware and software, how the morphology evolution of PUE under strain is investigated, meanwhile this issue also attracts the interests from industry. In fact, this thesis is cooperated with BASF who supplied the samples.

2 Background Knowledge

Polyurethane elastomers (PUE)[6, 7, 8] are superior materials combining high mechanical strength and elastic property that is applied widely like skate board wheels, industrial rolls, seals, car body panels and protective coatings. They are typically produced by reacting a high molecular weight polyol, a low molecular weight diol (“chain extender”) and an isocyanate using e.g. reaction injection molding, casting or spray processes. The isocyanate and chain extender react to form an effective hard module. Blocks of hard modules are usually called hard segments. They are linked through the the soft segment which is a high molecular weight polyol to form the final polymer structure that can be described as a segmented block copolymer[9] of the (A-B)_n type. Soft module and soft segments are identical, but chemists tend to call an alternating sequence of soft and hard modules a long soft segment.[10, 11]

As the hard and soft segments are thermodynamically incompatible (inherent immiscibility), it results in the formation of domains that are either rich in soft or hard segments, a phase-separated morphology may be obtained. The exact nature of the final morphology depends on both the molecular composition and the processing conditions. When the chemical composition is concerned, it’s commonly accepted that the extent to which phase separation takes place depends on the several factors, e.g., the distribution of hard segment and soft segment along the chain, the polarity difference or the compatibility between hard and soft chain segments, and the ability of the hard-segments to stack tightly and to establish strong intra-molecular interactions. Another generalization concerning phase separation may be that the larger the difference between the glass transition temperatures of the soft and hard segment rich domains is, the higher is the extent of phase segregation between the phases. This fact also reflects differences in polarity between the hard and soft chain segments.[7]

The formation of soft domain and hard domain are sketched in Figure 2.0.1. The morphology of PUE could affect its properties.[12, 13, 14, 15, 16, 17, 18, 19] The interaction between hard segments are hydrogen bonding of urethane group and π - π stacking of aromatic isocyanate.[20, 21] The interaction is acted upon by the configuration and mobility of the hard segment. The π - π weak interaction is strongly dependent on the alignment of the aromatic groups.[22] Establishing the relationship between morphology and PUE property is significant for optimizing the material property.

In this chapter, the research status of PUE material and how to extract the nanostructure from SAXS pattern are introduced briefly. As the SAXS theory is counter-intuitive, how to comprehend the SAXS is also discussed.

2 Background Knowledge

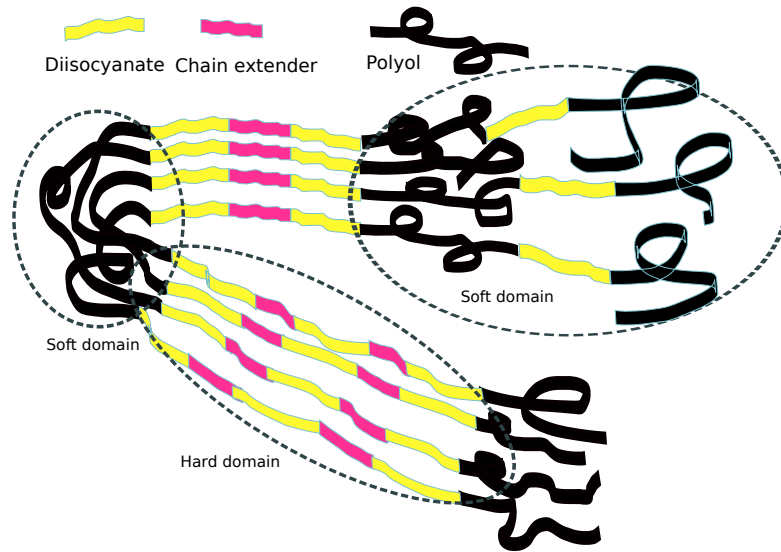


Figure 2.0.1: Soft domain and hard domain of PUE aggregated of soft blocks and hard blocks respectively. The aggregation of hard blocks is binded by hydrogen bonding. The alone diisocyanate is dissolved in the soft matrix.

2.1 Research Status of PUE

In this section, we will review the former enormous investigation of PUEs briefly. It covers the morphology of PUEs and their morphology evolution under strain, thermal-ageing effects on the morphology evolution of PUEs under strain and the failure mechanism of Crosslinked PUEs.

2.1.1 Nanostructure of PUE

The morphology of PUEs includes many aspects, such as domain size, domain shape, domain orientation, connectivity, interfacial thickness between two phases, and phase volume fraction.[7, 8] The stacking of the hard/soft segments and the extent of phase separation or mixing in the PUEs remarkably affect the volume fraction of certain phase, the absolute volume fraction of hard/soft phase is difficult to obtain. In this thesis, only a measure related to the volume fraction is discussed.

Morphology of PUE. Two-phase morphology of polyurethane was verified by a discrete peak of SAXS by Bonart[1] and Clough et al.[23] in 1968. Shortly after that, Koutsky et al. observed the two-phase morphology with electron microscopy.[24]

The morphology affected by hard segment content (HSC) was studied systematically.[25, 26, 27, 28, 29, 30] Only a few hard domains exist in the soft matrix at the low HSC level (e.g., 15%wt). The PUE with moderate level (e.g. 25%wt) of HSC exhibits the isolated hard domain nested in the soft matrix which results in the properties of low hystere-

sis and high extensibility. When the HSC is more than 30%, the PUE presents the bi-continuous (interpenetrated) morphology of hard phase and soft phase. There exists interconnectivity among the hard domains.[31] Moreover, many researchers found the bi-continuous structure by microscopy in real space. The interpenetrated morphology of PUE (e.g., 62%wt hard segment) is observed with transmission electron microscopy (TEM)[32] or atomic force microscopy (AFM)[33, 34, 35]. Saiani et al.[36], Koutsky et al.[24], Shilov et al.[37], Neff et al.[38], Rinaldi et al.[39], D'hollander et al.[40] and Boyce et al.[41] indicated the bi-continuous morphology in different PUEs.

Whether all the hard segments are arranged in the hard domain was studied by Koberstein et al.[12, 14] They proposed a model that partial hard segments is dissolved in the soft phase whose length is shorter than the critical length for phase separation. The longer hard segments would aggregate into lamellar hard microdomains whose thickness is approximated to the critical sequence length of hard segment.

The morphology of PUE is also altered by type of isocyanates[42, 43, 44], polyols[45, 46, 47], and chain extenders[48, 49, 50, 51], even processing conditions[52].

Morphology Affected by Synthetic Method. When TPUs are synthesized in a one-shot method, the raw components are simply stirred together. On a large scale, the process is carried out by machines (machine processing). “Hand-casting” refers to a process in which the components are poured into bucket and stirred. In such a “bucket and paddle mix”, the mixing quality may remain moderate. In other words, at different places in the bucket copolymer, chains with different sequence statistics will have grown. The mixture is poured onto a cool plate for curing. During this step the formation of convection cells is observed. Material taken from the center of the convection cells exhibits different compositions as compared to material from the edges of the convection cells.[53] So in the block sequences of hand-cast material a double variability is found, where the primary one is the result of the statistical nature of the polyaddition. This will probably affect even the morphology of hard and soft domains, which should exhibit greater variability of domain sizes. Ultimately, hand-casting might even have an impact on the materials properties. In studies that vary the molding conditions, effects on the materials performance have been reported for PU[54, 55, 56] or epoxy resin[57]. When the materials is synthesized in machine-casting, it exhibits quasi-periodicity of block arrangement.[58]

Domain Shape. Apart from the morphology affected by the content of hard domain, hard domain shape is also strongly dependent on the content of hard segment. The morphology of PUE with low HSC exhibits discrete domains nested in the soft matrix.[25, 59, 26, 33, 41] Stribeck et al. abstracted the shape of hard domain as the ellipsoid when it’s analyzed in SAXS.[60, 61] The bicontinuous hard phase in the PUE shows rod-like hard domain with interconnectivity when the weight fraction of hard segment is high.[62, 63] The material with high content of hard segments presents the lamellar hard domain[14, 64, 65]. The ribbon-like structure in the polyurea are observed by AFM.[33, 66, 67, 68, 69, 70, 71, 72, 73, 74, 75, 76, 77, 78] Kaushiva and Wilkes observed

2 Background Knowledge



Figure 2.1.1: The schematics of polyurethane nanostructure with different hard phase. (a) Ellipsoid-shaped hard domain. (b) Lamellar hard domain. (c) Bi-continuous network. The filled pattern indicates the hard phase.

a super large lamellar hard domain in the polyurethane by AFM.[79]

Domain Size. Domain size is related to its chemical structure directly. The size of hard domain is dominated by the critical length of a hard segment.[12, 14] For PUEs, there are several continuous MDI+ $\frac{1}{2}$ BD modules in one hard segment. The length of one extended MDI+ $\frac{1}{2}$ BD module computed from the crystallography is 3.0 nm.[80, 81, 82, 48, 49, 50, 83, 84] Longer urethane segment improves the extent of domain structure.[85, 23, 17, 86] The hard segment shorter than the critical length is supposed dissolved in the soft phase.[87, 88]

Based on the above analysis, we can abstract the PUE nanostructure as several types, ellipsoid-shaped hard domain nested in the soft phase, lamellar hard domain, bi-continuous network. The shapes of hard domain are sketched in the Figure 2.1.1.

2.1.2 Nanostructural Evolution under Load

How the morphology evolves under deformation is another issue for the structure-property relationship. The structure of PUE under deformation varies not only on the nanometer or domain scale, but also on the atomic scale.[30, 7, 89, 68, 8, 90] In this thesis, we will briefly introduce the research progresses on several aspects, e.g. orientation of hard segments, strain-induced crystallization of soft segments, failure of hard domains.

Domain Orientation. Bonart et al. studied the nanostructure of PUEs under deformation and pointed out that the periodic domains of PUE are oriented under stress.[1, 2, 3, 4, 91, 92, 93, 94]

Domain evolution model of PUEs affected by HSC under strain was investigated by Desper et al.[95, 96] They proposed three modes of domain evolution under load, shear mode, tensile mode, and rotation or translation of independent domain. Deformation mode depends upon the shape and structural integrity of hard domain. Shearing mode appears in the polyurethane with disk-shaped hard domain. Four-point SAXS pattern indicates lamellar hard domain tilting away from the elongation direction. Tensile mode appears in the polyurethane with cylindrical hard domain of comparable diameter and

thickness. Two-point SAXS pattern indicates the domain stacking of cylindrical hard domains along the elongation direction. Translation mode appears in the polyurethane with complicated shape of hard domain as the cross-linked hard segments precludes the formation of regular repeating units.

When the PUEs have bi-continuous morphology, both of the hard domain and soft domain would be deformed under stress.[97, 98, 99, 9, 100, 101] The soft segments would be oriented under the load. The hard segments would be transverse to elongation direction at small strain and turn parallel to the elongation direction at large strain. When the load is removed, the soft segments would present a nearly isotropic state, meanwhile the hard segments still exhibit the plastically deformed state. The orientation of soft segments, isolated hard segments and aggregates of hard segments are affected by the average length of hard segments.[101] Soft segments in some PUEs are slightly oriented under stress.[102] In some materials, orientation of hard segments are transverse to the elongation direction.[102, 79]

PUEs with same building blocks but synthesized in different ways present different domain orientation.[87, 88, 103] During the deformation, the SAXS pattern of PUE with random hard blocks changes from circular halo to ellipse. SAXS pattern of the PUE with mono-disperse hard blocks transforms into a four-point pattern. For the PUE with random hard blocks, the embedded particles of hard phase arranged in special lattice-like topology deform in the affine manner. But for the PUE with mono-disperse hard blocks, the interconnection prevents the affine deformation of the hard domains. When the interconnection is ruined, hard domains arranged in the four-point topology deforms in the affine manner.

The domain orientation is also affected by the strain rate[104, 105, 106] and temperature[107, 108]. The hard domains are oriented at small strain rate, but at large strain rate the hard domains are almost not oriented.

Domain Destruction. The hard domains are oriented in the elongation direction at small strain, the hard domains would be disrupted at large strain.[109, 110, 111] Fu et al. found the destruction of the hard domains by TEM.[110] Christenson et al. found the destruction of hard domains by AFM.[111]

When the hard phase is 3D network-like structure ($HSC > 40\%wt$)[112], the hard domains would experience shear-sliding plastic deformation and would be decomposed under strain. The irreversibility of interdomain spacing is ascribed to the breakdown of hard phase network structure ($HSC = 36\%wt$).[39] Lee et al.[107] figured out that a small amount of hard segments are pulled out from the hard domains during deformation. Buckley et al. ascribe the disruption of hard phase to the pull-out of the segments from the hard domains ($HSC = 40\%wt$) as well.[18] The stripping is possible due to the weak binding energy of hard segments at the boundary of the hard domains. The length of soft segment affects the critical strain of break-down of hard domains.[108]

Stribeck et al.[60, 61] illustrate the nanostructure evolution of PUEs based on the in-situ SAXS experiments. The hard domain is only correlated to its closest neighbor, namely the nanostructure is soft domain sandwiched by two hard domains. The macro-

2 Background Knowledge

scopic strain is accomplished by the failure of hard domains. The failure propagates from the disordered region to the well-arranged ensembles of hard domains.

Strain-induced Crystallization. Except the orientation and elongation of soft segments, the strain-induced crystallization of soft segments is possible.[1] The strain-induced crystallization of PUEs with different polyols exhibits completely different features.[85, 23] Polyether polyurethane shows a higher order than equivalent polyester polyurethane. Polyether polyurethane would be strain-induced crystallization under elongation but polyester polyurethane would not.

Physical and chemical properties of soft segments influence properties of PUE material dramatically.[113, 114, 115] Polytetrahydrofuran (PTHF) is a frequently-used polyol in the polyurethane chemical. The physical property of PTHF is well studied.[116, 117] The softening point of PTHF is $18 - 28$ °C, and glass transition temperature of PTHF is -77 °C. PTHF of low molecular weight solidifies between -15 °C and 30 °C. When PTHF is co-polymerized as the soft segment of a long-chain macromolecule, the chain segment of PTHF is melt at the room temperature.[118] The soft segments present the rubbery state or viscous state. However, strain-induced crystallization of PTHF is possible when the test is carried out at room temperature.[119, 110, 111] Strain-induced crystallization of PTHF becomes pronounced with increasing the content of hard segment.[120]

The crystallites induced by strain and the virgin crystallites in the PUE show different influence on nanostructure evolution under deformation.[121] The strain-induced crystallites induce the microfibril structure of PUE at strain $\varepsilon > 1$ which exhibits a two-point SAXS pattern. A small amount of virgin crystallites induce chevron-like hard domain arrangement at strain $\varepsilon > 1$ which exhibits a four-point SAXS pattern. The crystallites induced by the strain provide the reinforcing effects compared with the polyurethane without crystallizable soft segments.[122]

2.1.3 PUE Ageing

The ageing/degradation of PUE is a pervasive problem for the industry application. In particular, the environmental temperature, humidity and high-energy ray play the important roles in the degradation of PUE.[123, 124, 125, 126, 127, 128, 129, 130, 131, 132] These conditions weaken the thermal and mechanical performance during the service period of product. The investigation of ageing mechanism may predict and even extend the service lifetime of PUE parts.

General. Thermoplastic polyurethanes (TPUs) are a subcategory of the polyurethane elastomers (PUE), namely the portion which can be melted and processed. Elastic are these materials due to their two-phase morphology. A soft phase makes the TPUs deformable. Embedded hard domains act as physical crosslinks. The combination of these characteristics makes the material flexible. With PUs the topology is usually much more distorted than with comparable other polymers. For example, the shape of the hard domains cannot generally be described by simple bodies (lamella, cylinder, sphere). Microscopic images often show only a grained[133] morphology. An arrangement of these

grains can be guessed at most. The small-angle scattering, however, shows a wide long-period peak. Thus some rudimentary order exists. The respective topology may be quantified by fitting the scattering data to an appropriate morphological model.

Thermal aging tests are most frequently carried out in air at elevated temperature. They are used to assess lifetime or a loss of the functionality of the material. Closely related to aging is annealing. It is carried out in vacuum or in an inert atmosphere. The goal of annealing is, in general, a maturation of the morphological structure.

It is not a simple task to quantify the effect of aging on an already blurred morphology. This may be the reason that there are not so many reports on the influence of aging on the two-phase morphology of PU. Comparing their number with the number papers on the general subject of aging of polyurethanes, the quantification of morphological modifications appears as a field in which there are still some gaps to be closed. In particular, we have found no studies in which both the morphology of the TPU and its response to mechanical load are characterized as a function of aging duration. The corresponding effects are in the focus of our present study.

Reviews. A comprehensive review[134] is dedicated to the question of how to increase the thermal stability of PU materials. The authors conclude that the thermal decomposition of PU affects the hard domains first, because their building blocks, the hard segments, are attacked early. Yong He et al.[78] present a review on the structure and morphology of polyurethanes. They write that the hard domains do not only act as reinforcing fillers, but also improve the thermal performance of the material. Other reviews consider aging under biological conditions[135] or focus on the optimization of morphology and thermal stability by tailoring of the chemistry[136, 90].

Annealing studies in original literature. Kazmierczak et al.[137] anneal TPUs for 2 d in vacuum between 80°C and 167°C and study the morphology by SAXS. They cannot detect significant effects on the topology. Martin et al.[113] anneal TPUs under nitrogen atmosphere for 10 h between 80°C and 170°C and carry out a SAXS study. At 150°C and 170°C some aging is already observed. Temperatures between 80°C and 100°C appear to be the best choice for a maturation of the two-phase morphology. Castagna et al.[74] anneal polyureas for 8 h under vacuum at 120, 150, and 170°C and study the isotropic materials by atomic force microscopy (AFM) and scattering methods. From the 120°C experiment they conclude that the maturation transition happens above 70°C and demonstrate that it is not only temperature dependent, but also a function of time. Yanagihara et al.[35] anneal a TPU with a hard-segment content of 43 wt.-% in vacuum for 16 h between 40 and 160°C and study the isotropic material by scattering methods. They fit the SAXS curve by a Percus-Yevick[138] model assuming hard domains of ellipsoidal shape in order to be able to draw conclusions on the hard-domain growth direction. In the Percus-Yevick model the domains are placed almost at random, and in the model the observed long-period peak is imprinted by an interaction potential. Yanagihara et al. find that the additional consideration of a domain-size distribution overstrains the fit and spoils the significance of determined parameters.

Thermal aging in original literature. Tang et al.[139] age a TPU at low temperature (40 – 70°C) for up to 300 days. Its composition is quite similar to that of the original material of our present study. They report that the phase separation decreases with increasing duration of the aging. On the other hand, Gibson et al.[140] report increased phase separation and an increase of the domain sizes. They age similar materials at high temperature (90°C and 150°C), study the morphology by small-angle X-ray scattering (SAXS) and analyze their data by means of the general[141] correlation function approach.

Huitron-Rattinger et al.[142] study a TPU of completely different composition compared to ours. They subject the material to 7 temperature cycles (oscillation between 20°C and 180°C). The morphology of the aged material is studied by SAXS. The authors find domain enlargement.

Madkour and Mohamed[143] age a series of TPUs at 100°C for intervals between 2 days (2 d) and 14 d and study the resulting morphology by SAXS. SAXS curves of the isotropic materials are fitted by various models. The best-fitting model is defined by almost random arrangement of spherical hard domains according to Percus-Yevick[138]. The aging alters the morphology, but not the thermal stability. The hard domains grow.

Tian et al.[144] study isotropic TPU (Estane 5703) aged at 70°C for 60 d in dry and wet air, respectively, by means of small-angle neutron scattering (SANS). Several models are fitted to the curve. The best fit is obtained by the Percus-Yevick[138] model of spherical hard domains under consideration of a diameter distribution. The analysis returns a growth of the hard-domain size from 2.3 to 3.8 nm, and a growth of the next-neighbor distance from 8.4 to 10.6 nm.

Two papers[145, 146] find that the first stage of thermal degradation affects the hard segments. Mass loss and degradation of the mechanical properties are observed in the second stage, when the soft segments degrade.

Boubakri et al.[129] age a TPU in air for up to 270 d at 70 and 90°C. They carry out tensile tests and find that aging increases the rigidity of the material.

In summary, the studies can be divided into two groups, namely, low temperature experiments in which generally the domain sizes and the distances among them do not increase, and high-temperature studies. Our work is a high-temperature aging study.

Morphology Variation. PUE aged at high temperature for a rather long time is employed to investigate the thermal degradation, however, in the beginning stage, the ageing is also a hyperthermal annealing process.[134] The phase transition is still ongoing and morphology is varying at high temperature. Post-annealing effect of PU at high temperature increase the size of hard domain, degree of phase separation.[140] Annealing also increases the thickness of transition zone slightly and annealing at high temperature increases the interdomain spacing dramatically due to the aggregation of hard domains.[137] Post-annealing could promote the chain alignment perfection of hard domain and facilitate further phase separation of fractional hard segments dissolved in the soft matrix.[147] Koberstein-Stein coiling/folding hard-segment model[64] is used by Li et al.[147] to interpret post-annealing effects, the hard segments extending gradually with

increasing annealing temperature induce the increase in interdomain spacing. Longer soft or hard segments could develop maximal interdomain spacing at higher annealing temperature.[113] The mobility of hard segment increases with increasing annealing temperature and results in a higher degree of phase separation.[148] Domain reorganization is dependent on both time and temperature.[74] Ribbon-like morphology can be preserved after different annealing experiments and interdomain spacing and strength of ordered hydrogen-bonding increases with increasing annealing temperature. When the sample is subjected to the thermal ageing for a long time, the disruption effects of domain become more prominent. Nanostructure becomes disordered or homogeneous with increasing ageing time and temperature.[149] The number density of hard domains decreases with increasing annealing temperature and this decrease may be due to the coarsening driven by the phase separation, actually smaller hard domains disappear and redeposit onto larger hard domains. At high annealing temperature, smaller hard segments would be melt into the soft matrix.[35] The hard domain size and interdomain spacing increase with extending the ageing time and temperature, the increase of interdomain spacing is due to the disrupted hard segments migrating into the soft matrix.[144]

Chemical Variation. The chemical structure of PU varies significantly under ageing except the morphology variation. The variation of domain on the atomic scale is due to the chemical decomposition. Yellowing is an apparent variation during PU ageing.[150, 128] Bruckmoser et al. indicate that the yellowing of PU during ageing is formation of chromophores and thermal loading influences the degree of order within hard phase.[151] In the ageing, the urethane bond is unstable above 170 °C and degradation mechanism is thermal dissociation of urethane groups into free isocyanates and alcohols.[152] The concentration of free and hydrogen-bonded carbonyl group decrease and voids appear when sample is aged.[124, 125, 129] The mass loss of PU in ageing is apparent and directly related to the hard segment (HS) content and the HS is the most susceptible segment.[153] The methylene diphenylene (MDI) can be oxidized and generate benzophenone derivatives except the oxidation of soft segments.[154]

Hu and Koberstein indicated that increasing the annealing temperature and time would accelerate the branching reaction and increase the molecular weight.[155] Christenson et al. observe the chain scissoring and crosslinking of soft segments.[156] Chuang found the crosslinking of soft segment inhibits the cross-polymerization in the hard domains at high temperature.[157] Dannoux et al. indicate that the soft segment scissoring and crosslinking are in competition during degradation of PU.[127] The degradation occurs not only the hard domain but also the soft domain, the degradation also induces some chemical reactions and generates new material.[146]

2.1.4 Cross-linked PUE

Many PUEs are chemically crosslinked. This is in general achieved through the use of branched polyols[158, 159, 160], but branching may also be introduced via the isocyanate[161, 43, 162, 163]. Both, the physical and chemical crosslinks, allows PUE to be stretched and then recover to their initial shape when released. The resilience depends largely on

2 Background Knowledge

the extent to which phase separation has occurred. The ultimate tensile properties, like elongation at break, are largely governed by the level of chemical crosslinking.

The extent to which these materials are phase separated depends on the difference in solubility characteristics of the soft and hard chain segments, the molecular weight and the topology of the polyol. By varying the molecular composition of a PUE the obtained morphologies may change drastically. Some PUEs the structure may be close to a nanoscopic amorphous state. This state is a homogeneous[164] blend-phase consisting of hard and soft chain segments. Others classes of PUEs, like thermoplastic polyurethane (commonly referred to as TPU) may develop high levels of ordering[60]. Most PUEs, however, have morphologies somewhere in between: The polymers are phase separated to a certain extent, the sizes of the hard domains vary considerably and among the domains longer ranging order is rare. Nevertheless, in the vicinity of a hard domain a pretty orderly arrangement may exist as has been demonstrated by scattering experiments[23, 165]. Chemical crosslinking has a strong impact on the level to which phase separation and domain formation occurs.[43, 162, 163, 39, 166, 74]

In the literature we have found only few studies that discuss failure mechanisms in PUE. In general the amount[54] and the intrinsic stability[6] of the hard domains appear to be important. This is especially so for linear PUE like TPU. For chemically crosslinked PUE also the crosslinking density of the polymer network plays a role as crosslinking will affect the phase separation process during the synthesis of the polymer and the extensibility of the polymer network upon strain as increased levels of crosslinking reduce the extensibility of the polymer.

Concerning straining mechanisms, violation of the time–temperature equivalence with PUE materials[164] indicates that straining is accompanied by fundamental morphological changes. A second indication for such changes is related to an observation during tensile tests. The observed SAXS long period lags considerably behind the expectations [96, 87] or even decreases[96, 61] while the material is strained. Thus several authors relate failure to indications of hard-domain disruption[167, 168, 169, 102, 170]. Other authors focus on the elastomer network. Smith[164] studies quasi-homogeneous PUE materials of low connectivity. Wilkes' group[165] detects thread-like arrangements of nanoscopic dimensions that indicate one-dimensional (1D) connectivity, and Enderle et al.[112] propose a deformation theory that is based on three-dimensionally (3D) interconnected hard-domains. Due to relatively short tie molecules this network is postulated to be irreversibly decomposed under strain. Blundell et al.[87] address the short tie molecules, as well. They demonstrate that the scattering entities cannot be deformed affinely in PUE materials with monodisperse block lengths. Several of the discussed mechanisms are said to be hypothetical, so the need for additional work is claimed[30], and according to Prisacariu[8] the nature of hard domain restructuring during deformation continues to be a subject of research.

The SAXS scattering intensity of poorly ordered materials is low[23, 171]. Discrete peaks are weak as compared to the intensity in the center of the pattern. In earlier experiments[60, 61] the intensity with similar samples has been too low for good scattering patterns. In the present study our group has succeeded to collect sufficiently good data from such samples. This is due to a particularly suitable synchrotron beamline. The

instrument is set up behind a wiggler that provides a photon flux, which is three orders of magnitude higher when compared to the DORIS bending magnet of former beamline A2[172].

2.2 Knowledge of SAXS

Two-phase structure of PUE are accepted widely. How to evaluate the morphology quantitatively is a tough nut to crack. An intuitive and easy tool to visualize the nanostructure is electron microscopy (EM), however the shortcomings of EM are obvious that in-situ investigation of nanostructure evolution is not easy. SAXS is a sharp tool to extract the parameters of domain structure. It can detect the microstructure inhomogeneities on nanometer scale and perform the statistics of sample volume in several cubic millimeters. However, the SAXS pattern shows nanostructure information in reciprocal space. It's not easy to directly visualize the nanostructure in consciousness of human beings from SAXS pattern.

To overcome the nonintuitions of SAXS, methods of converting nanostructure in reciprocal space to physical space have been developed. Porod discussed the basic properties of scattering from multiphase system.[173] Debye introduced the general correlation function to analyze scattering phenomena of distorted structure, the general correlation function converts the problem in reciprocal space to structure in physical space.[174] Vonk and his coworkers pragmatized the concept of general correlation function into one-dimensional correlation function which can be utilized in a lamellar two-phase system.[175, 176, 177, 178] Based on the assumption that the layer thicknesses vary little about an average value, Strobl et al. used the graphic method to extract the average layer thickness.[179] However, the polydispersity of layer thicknesses is a quite universal issue in the polymer materials. This assumption results in a large deviation of average value of layer thicknesses from the true average value.[180]

To solve the problem of polydispersity, Mering and coworkers devised chord distribution function (CDF) which is the second derivative of correlation function.[181, 182, 183] The CDF is based on the particle size distribution which is the basic for the structural analysis. The concept of chord is first widely made applicable for of practical problem by the interface distribution function (IDF), which is deduced by Ruland and Stribeck.[184, 185, 186] The comparison between one-dimensional correlation direction and IDF is described by Cruz and Stribeck et al.[180]

Multi-dimensional CDF is an easy and effective method to determine the existence of another particle in the spatial neighborhood of one particle which is realized by Stribeck.[5] CDFs visualize the local structure in the neighborhood of a domain: Each peak shows, in which direction and distance neighbor domains are found that generate a long period. The integral of a peak is a measure of the population density.

Apart from converting the SAXS pattern to transformed functions, there is another route to establish the nanostructure in the material, fitting the scattering pattern or intermediate functions with the well-modified standard model. We will introduce the fitting of SAXS briefly in the subsequent section.

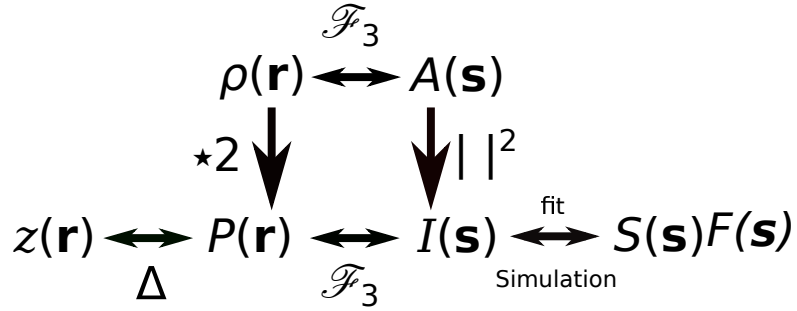


Figure 2.2.1: Magic square of scattering presenting the fundamental relations between electron density distribution $\rho(\mathbf{r})$, and the observed scattering intensity $I(\mathbf{s})$. $P(\mathbf{r})$ is the Patterson correlation function. $z(\mathbf{r})$ is the chord distribution function. \mathcal{F} is the 3-dimensional Fourier transform. $I(\mathbf{s})$ is the absolute square $||^2$ of scattering amplitude $A(\mathbf{s})$. $\star 2$ designates the auto-correlation function. $S(\mathbf{s})$ and $F(\mathbf{s})$ is the structure factor and the form factor respectively.

2.2.1 Magic Square of SAXS

As early as 1930's, X-ray scattering at the small angle applied in the structure investigation of metallic alloy was developed by Guinier and Fournet.[187] The methodology of processing the SAXS data is moved forward greatly during the past several decades. Several monographs in this discipline are written by Guinier and Fournet[187, 188], Hosemann[189], Balta and Vonk[190], Krattkey and Glatter[191], Feigin and Svergun[192], Stribeck[193], and so on. They uncover the methods to explore the nanostructure of materials.

A well-known magic square of scattering is abstracted and extracted from the methods proposed by those pioneers in the SAXS which is shown in the Figure 2.2.1. The Fourier transform \mathcal{F} connecting the reciprocal space and real space is based on the Fraunhofer approximation¹ of kinematic scattering theory. The Fourier transform is only valid when the imaging plane is far from the scattering object, namely far-field imaging. In the experiment, what we only can collect is scattering intensity pattern $I(\mathbf{s})$. Patterson's correlation function $P(\mathbf{r})$ is resulted from scattering intensity $I(\mathbf{s})$ subjected to Fourier transform \mathcal{F}_3 . The physical significance of $P(\mathbf{r})$ is the autocorrelation function (superposition) of electron density distribution function $\rho(\mathbf{r})$. Chord distribution function $z(\mathbf{r})$ is deduced from correlation function $P(\mathbf{r})$ subjected to second derivative. $z(\mathbf{r})$ is the autocorrelation function of the gradient function of electron density distribution function $\rho(\mathbf{r})$. $S(\mathbf{s})F(\mathbf{s})$ employed to fit the scattering intensity $I(\mathbf{s})$ is the scattering function of ideal particle stacking model. $S(\mathbf{s})$ and $F(\mathbf{s})$ is the structure factor and form factor respectively.

¹Fraunhofer scattering is used to model the diffraction pattern viewed at a long distance from the diffraction object.

2.2.2 Methods of Data Evaluation

The magic square shows us three routes to evaluate the scattering intensity $I(\mathbf{s})$, two of them, $P(\mathbf{r})$ and $S(\mathbf{s})P(\mathbf{s})$, are reversible, the third one $A(\mathbf{s})$ is irreversible. The routes of SAXS data evaluation can be divided into two orientations, fitting using ideal model and modeling from model-free function. Fitting the scattering pattern or curve using the analytic equation with the user-supplied parameters is used extensively in the study of simple particle stacking system. Constructing the nanoparticle stacking model from the transformed function of the scattering pattern or curve provides another route to study the material nanostructure.

2.2.2.1 Model-free

Model-free method extracts the nanostructure from the scattering intensity without any model assumption at hand. The simplest method to evaluate the intensity based on the model-free assumptions is correlation function which is the resulted function of Fourier transform of scattering intensity. The interface distribution function (IDF) initiated by Ruland[184, 185, 186] is one-dimensional correlation function of the gradient of the electron density function. Chord distribution function (CDF) applied to investigate the fibrous nanostructure initiated by Striebeck[5] is the multi-dimensional interface distribution function. Pair distribution function, also named as radial distribution function, describes how density varies as a function of distance from the reference particle. In the SAXS theory, these evaluation methods are abstract for understanding. In this thesis, we try to clarify the physical significance of these functions briefly.

Figure 2.2.2 shows the electron density function and gradient function of electron density function along a straight line (chord) in the deliberate direction. If we can perform a statistic of density variation along all the chords spatially, we can get the average values of nanostructure. The SAXS could carry out statistics for the density variation in reciprocal space. The correlation function or distribution functions mentioned above extract the nanostructure from reciprocal space and present it in real space. These functions facilitate to extract the average size of nanoentities from the practical morphology of material. For the particular morphologies, e.g. random distribution or highly oriented distribution of particle, the nanostructure can be described by 1D analytic function.

One-dimensional Correlation Function. Correlation function (including the autocorrelation function and cross-correlation function) is used to establish the similarity between a function and another function. The autocorrelation function in the material research can detect the repeating domains, namely the presence of the periodic or regular domain stacking. The mathematical form of the autocorrelation function is shown in the equation 2.2.1.

$$h^{*2}(r) = h(r) * h(-r) = \int_{-\infty}^{\infty} h(y) h(r+y) dy \quad (2.2.1)$$

In the spatial domain, the autocorrelation can be interpreted as the overlapping integral of the function and its shifting ghost. Figure 2.2.3 shows the schematic of the autocor-

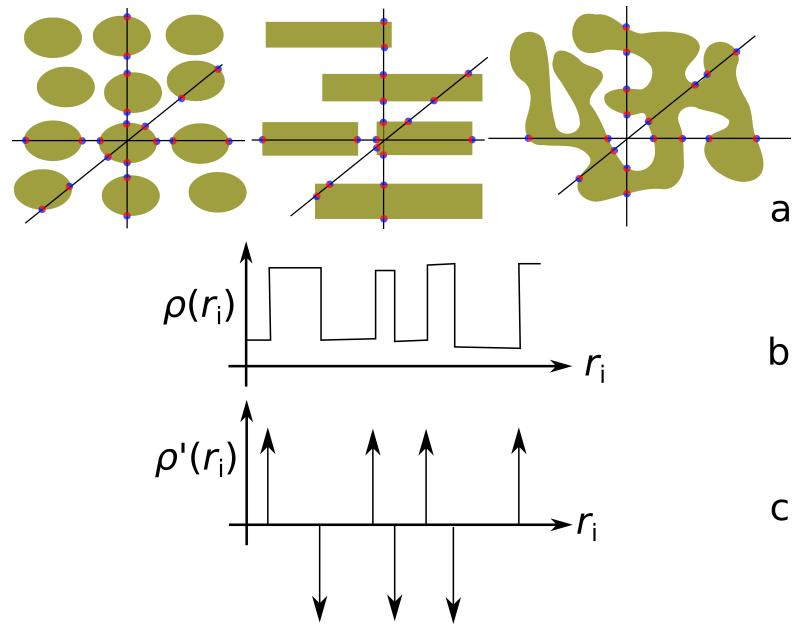


Figure 2.2.2: (a) Schematics of the straight lines (chords) penetrating through two-phase structure of polyurethane. The small circles indicate the phase boundary. Subfigure (b) shows the density variation along the chord, subfigure (c) exhibiting the gradient of density function shown in subfigure (b) is a series of δ -function which mark the positions of domain boundary.

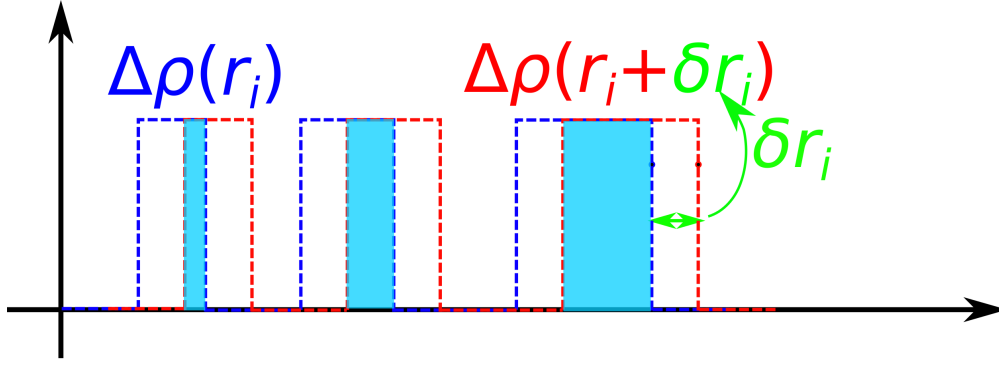


Figure 2.2.3: Schematic diagram of 1D autocorrelation function $\gamma_1(r_i)$. $\Delta\rho(r_i)$ is the electron density difference of two-phase along certain direction. Each value of $\gamma_1(r_i)$ is proportional to the overlap integral (the shaded area) of the density difference $\Delta\rho(r_i)$ and its displaced ghost $\Delta\rho(r_i + \delta r_i)$ with displacement δr_i .

relation function of density function $\Delta\rho(r_i)$ which is mentioned in Figure 2.2.2b. The density difference $\Delta\rho(r_i)$ is simplified by $\Delta\rho(r_i) = \rho(r_i) - \langle\rho\rangle_V$ with $\langle\rho\rangle_V$ being the average density. The variable δr_i indicates the displacement. The total shaded area $\gamma_1(r_i)$ as a function of displacement δr_i results in the 1D correlation function.

$$\gamma_1(r_i) \propto \int_0^{\infty} \Delta\rho(r_i) \Delta\rho(r_i + \delta r_i) d\delta r_i \quad (2.2.2)$$

The classical applicable model-free structure visualization can be retrospectively to Vonk[176, 177] who described the structure by 1D correlation function $\gamma(r_i)$ in physical space.

The 1D correlation function computed from the 1D scattering intensity, $\{I\}_1(s)$ or $I_1(s)$, is executed by the 1D Fourier transform (normally executed by cosine transform).

$$[\gamma_1](r_i) = \frac{2}{k} \int_0^{\infty} \{I\}_1(s) \cos(2\pi r_i s) ds \quad (2.2.3)$$

$$\gamma_1(r_i) = \frac{2}{k} \int_0^{\infty} I_1(s) \cos(2\pi r_i s) ds \quad (2.2.4)$$

$$\gamma_1(r_i) = \frac{4\pi}{k} \int_0^{\infty} s^2 I(s) \cos(2\pi r_i s) ds \quad (2.2.5)$$

Here, k is the total scattering intensity $\int I(\mathbf{s}) d^3s$. Equation 2.2.5 is valid for the isotropic scattering of lamellar multi-phase system as the 1D scattering intensity needs

2 Background Knowledge

to be subjected to the Lorentz correction. For the numeric computation of 1D correlation function, either a Porod-law analysis needs to be carried out, or the interference function could be got from the spatial frequency filtering. These two methods are used to determine the scattering intensity of the electron density fluctuation inside one phase or the ambiguous boundary of two-phase. Any deliberate direction can be chosen to evaluate the domain arrangement. When the material is strained, the elongation direction is chosen frequently and it indicates the fiber-like domain stacking.

The correlation function defined in physical space is frequently limited to determine the crystallinity and the long period in the lamellar stack which can be extracted by application of a simple graphical evaluation method.[176, 179, 194] However, the nanostructure not only contains the composition of lamellar component, but also contains the disordered domains pointed out by Hermans and Hosemann.[195, 196] The domain clusters are frequently observed in short-range correlation. The plain correlation function can't reveal the statistics of domain size distributions in a simple way.

The polydispersity is an avoidless issue in the polymer science, its improper reflection in the correlation function is the principal disadvantage of correlation function.[180, 197] It means that extracting domain thickness distribution is not easy from correlation function in the layer stacks or microfibrils system. If we want to perform the statistics for the domain thickness, devising a new method to evaluate the polydispersity of the domain is obligatory.

Interface Distribution Function. In Figure 2.2.2c, the edge effect of domain is magnified by the gradient (first derivative) of density function. The gradient function is a series of δ -function. From the physical significance of autocorrelation function, we know that the autocorrelation function is proportional to the overlapping area between this function and its shifting function. The peak positions of the autocorrelation function are related to the displacement which is a measurement of the domain size and domain periodicity. This method in 1D case is the interface distribution function.[184, 185, 186]

The interface distribution function is defined as

$$g_1(r_i) = - \left(\frac{d\rho_1(r_i)}{dr_i} \right)^{*2} = -k\gamma_1''(r_i) \quad (2.2.6)$$

which is proportional to the second derivative of the related 1D correlation function, $\gamma_1(r_i)$. $g_1(r_i)$ is computed from 1D interference function $G_1(s_i)$ subjected to 1D Fourier transform.

$$g_1(r_i) = -\mathcal{F}_1 \left(4\pi s_i^2 I_1(s_i) - \lim_{s_i \rightarrow \infty} 4\pi s_i^2 I_1(s_i) \right) = -\mathcal{F}_1(G_1(s_i)) \quad (2.2.7)$$

$I_1(s_i)$ indicates a 1D projected curve.

The IDF $g_1(r_i)$ is similar to the chord length distribution $g(r)$ which is constructed from the statistics of all the segments that penetrate a domain in any direction. Obviously, $g_1(r_i)$ is more selective as it can be used to perform the statistics of domain size and its distribution $h_1(r_i)$ in the specific direction. In the practical application, the microfibril axis direction and lateral direction are chosen frequently.

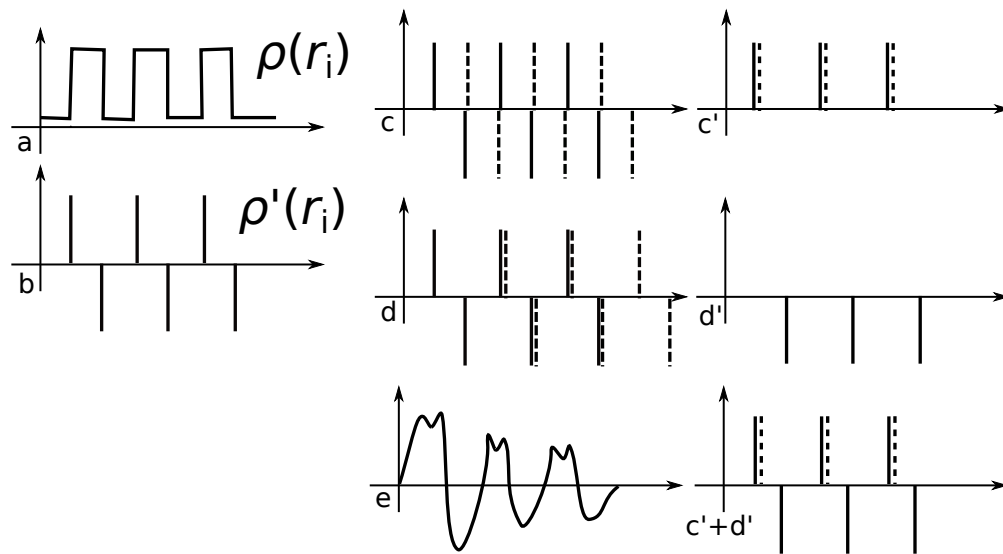


Figure 2.2.4: Schematic diagram of generation of interfacial distribution function. Subfigure (a) and (b) is the density function and the gradient of density function, respectively. Subfigure (c and d) shows the different displacements. Subfigure (c') and (d') is the correlation function with different shifting distance. Subfigure (c'+d') is the “sum” of functions in subfigure (c') and (d'). Subfigure (e) is broadened by polydispersity of domains from subfigure (c'+d').

2 Background Knowledge

Figure 2.2.4 sketches the generation of 1D interface distribution function. The schematic diagram is based on the autocorrelation of gradient of electron density function. Subfigure (a) and (b) indicate the electron density function and gradient of electron density function mentioned in Figure 2.2.2. Subfigure (c) and (c') shows the superposition of the gradient function and its ghost function when the shifting distance is equal to the size of soft domain or hard domain. Subfigure (d) and (d') indicates the superposition of the gradient function and its ghost function when the shifting distance is equal to the long-period. Subfigure (c'+d') shows the addition of subfigure (c') and (d'). Subfigure (e) shows the general IDF what we see frequently when the polydispersity of domain size and blurring boundary are introduced into the ideal stacking model. The advantages of IDF is quite obvious, the domain size and long-period can be extracted from the peak position. Because of the introduction of gradient of electron density function, the domain edge is a series of δ -function, the edge effect is enhanced. The precision of statistics of domain size and its distribution is also enhanced correspondingly.

In consideration of the physical significance of IDF indicated by Ruland[184, 185], the peaks of IDF are combination of a series of distance distribution function. These distance distribution functions describe the distribution of domains stacking along certain direction. If we want to visualize the 2D correlation of one domain in the meridional and equatorial direction simultaneously, the chord distribution function[5] can be employed.

Chord Distribution Function. If the material exhibits the fibril-like nanostructure with lateral correlation, the 1D interface distribution function can't visualize the correlation of one domain with other domains in the lateral and vertical direction simultaneously. Therefore, a 2D plot of the IDF is required. Apparently, we could synthesize the 2D plot from a complete set of IDFs which are computed by projecting the scattering intensity to the different azimuthal angles[184], however, a feasible algorithm is not found yet.

For the application in anisotropic scattering pattern (layer stacks or microfibrils), Stribeck[5] has devised a new algorithm to extend the edge enhancement principal to multiple dimensionality. The fiber-symmetric chord distribution function (CDF)

$$z(r_{12}, r_3) = (\nabla \rho(r_{12}, r_3))^*{}^2 = k \Delta \gamma(r_{12}, r_3) \quad (2.2.8)$$

is closely related to Vonk's multidimensional correlation function $\gamma(r_{12}, r_3)$ [198]. Compared with equation 2.2.6, the $d\rho_1(r_i)/dr_i$ is replace by the gradient ∇ , the second derivative d^2/dx^2 is presented by the Laplacian Δ .

In analogy to the physical significance of correlation function and interface distribution function, Figure 2.2.5 sketches the generation of CDF from the 2D particle and its ghost. In the multiphase material, the gradient $\nabla \rho(\mathbf{r})$ is zero almost everywhere except the domain surfaces. The CDF can be achieved by shifting of the gradient vectors in ergodic directions. The superposition of the particle shape its shifting ghost outlines the shape of particle and correlation between particles in real space. CDF as a function of the trace of shifting ghost describes the occurrence of nonzero superposition around the domain surface. The trace going through the surface of hard and soft domain exhibits nonzero superposition peak.

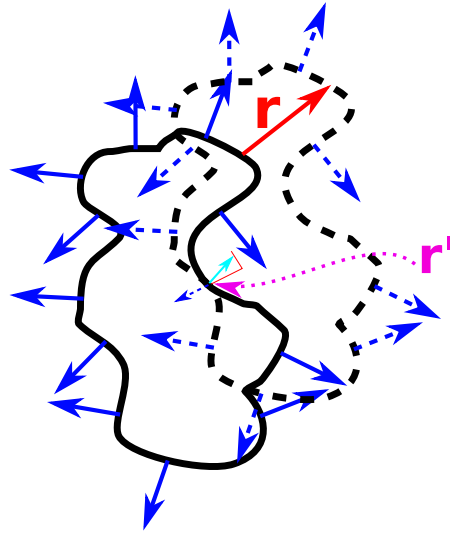


Figure 2.2.5: Schematic diagram of generation of chord distribution function by particle-ghost autocorrelation of gradient vectors. The solid vectors and dashed vectors emanate from the surfaces of particle and its ghost that is displaced by the vector \mathbf{r} . At position \mathbf{r}' , the contribution of CDF which originates from the scalar product of two gradient vectors is generated.

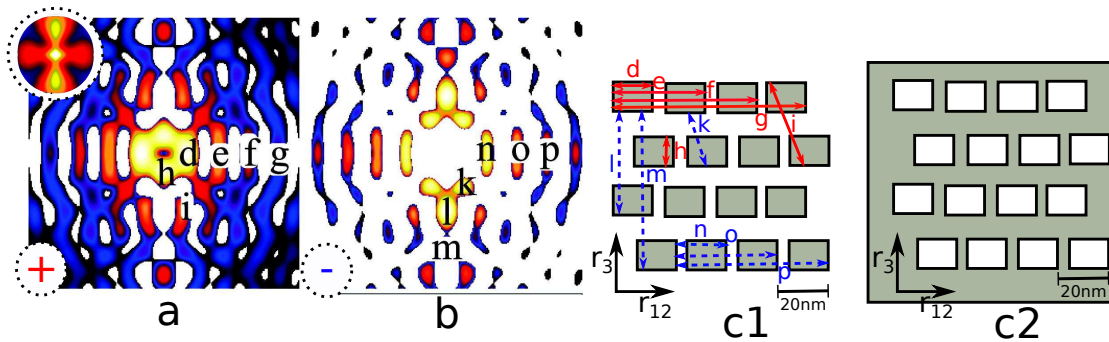


Figure 2.2.6: An example to interpret how to extract the nanostructure of material from CDF peaks.[199] Subfigure (a) and (b) exhibiting positive peaks (domain peaks) and negative peaks (long periods) of CDF are computed from a SAXS cross-pattern of polypropylene that is displayed in up-left corner of subfigure (a). Subfigure (c1) exhibits the block-structure model with indication of CDF peaks. Subfigure (c2) exhibits the cross-hatched model achieved by phase inversion of block-structure model.

2 Background Knowledge

An example shown in Figure 2.2.6 is helpful for us to understand the CDF.[199] This figure indicates how to extract the domain arrangement from the CDF peaks. The SAXS pattern shown in the upper-left corner of subfigure (a) is scattered from the oriented quiescent crystallization of polypropylene. Subfigure (a) and (b) show the positive face and negative face of CDF respectively. Generation of domain peaks on subfigure (a) and long-spacing peaks on subfigure (b) are indicated by the correlation between different domains shown in the subfigure (c1). Subfigure (c2) indicates the cross-hatched model achieved by phase inversion of block-structure model because of the Babinet theory.

If we link the CDF peaks with the gradient of density function shown in Figure 2.2.5, $z(\mathbf{r})$ as a function of ghost displacement $\mathbf{r} = (r_{12}, r_3)$ shows peaks $h_i(r_{12}, r_3)$ wherever there is domain surface contact between domain in $\rho'(\mathbf{r}')$ and its displaced ghost $\rho'(\mathbf{r}' - \mathbf{r})$. Such peaks $h_i(r_{12}, r_3)$ is called distance distribution function. In order to extract the distribution of domain size or distance, fitting the IDF or CDF with Mellin convolution can be carried out.[200, 197]

Relationship between a CDF and IDFs. Every IDF is a 1D radial slice through the center of the CDF by definition whose slicing direction could be presented by a polar angle Ψ and azimuthal angle φ .

$$[z]_1(r_{\Psi, \varphi}) = g_1(r_{\Psi, \varphi}) \quad (2.2.9)$$

What attracts us in the study of fibrous nanostructure is the slice of CDF along the fiber axis r_3 and transversal direction r_{12} .

$$[z]_1(r_3) = z(0, r_3) = g_1(r_3) \quad (2.2.10)$$

$$[z]_2(r_{12}) = z(0, r_{12}) = g_2(r_{12}) \quad (2.2.11)$$

2.2.2.2 Fitting with Ideal Model

For some materials with particular nanoparticles, such as core-shell colloid, lamella, micelle, vesicle, the parameters of the nanostructure can be fitted using the modified equations.[187, 191, 201]

For the semi-crystalline or phase-separated polymer system, fitting of scattering curve, fitting of 1D correlation function, or fitting of interface distribution function (IDF) with standard stacking models are done by Striebeck[180, 202, 200, 203, 197, 204] and Crist [205, 206, 207]. In their methods, the distribution of domain size is described in symmetrical Gaussian distribution function or asymmetrical Reinhold distribution function[208]. The ordinary convolution[196] and Mellin convolution[197] are employed to determine the polydispersity of nanodomains.

The IDF fitting employed in this thesis is introduced briefly herein.

IDF Fitting. IDF $g_1(r)$ of a lamellar two-phase system can be expanded into a series of distance distribution function, $h_i(r)$.[186]

$$g_1(r) = A_p \sum_{i=1}^m c_i h_i(r) \quad (2.2.12)$$

with $c_i = 1$ for $i \bmod 3 \neq 0$, and $c_i = -2$ for $i \bmod 3 = 0$. This equation is valid for the infinite stack. If one wants to fit the IDF with a model, the distribution function $h(r_i)$ must be determined first. Some experiments have indicated the asymmetric distribution of crystalline thickness and long periods.[208, 194, 209, 210, 211] If these asymmetric distribution functions, e.g. Reinhold distribution[208], are utilized as the base functions, $h_i(r)$, of IDF, there would be a cut-off in the IDFs. The cutoff was not found in the IDFs. If the asymmetric Hanna-Windle distribution function is employed, an analytic expression for its center of gravity is not possible in mathematics. This also constrains its application in SAXS data and IDFs. Moreover, if one intends to fit the IDFs with symmetric distribution functions, Gaussian normal distribution is possible,

$$N(x, d_i, \sigma_i) := \frac{1}{\sqrt{2\pi}\sigma_i} \exp \left\{ -\frac{1}{2} \left(\frac{x - d_i}{\sigma_i} \right)^2 \right\}. \quad (2.2.13)$$

If this equation is plugged into the equation 2.2.12 with large m (e.g. $m=25$), this model will have the disadvantage of a large parameter set. However, its advantage is also very obvious, we don't need to introduce any pre-determinations on the statistics of layer stacking. Several papers have been published based on this model.[180, 212, 213, 214] In order to simplify the fitting of two-phase paracrystalline system, a different model assumes "inhomogeneous system with exact lattice"[173] by Porod, where they assumed that each stack is perfect and the lattice constant is varying from stack to stack. Ruland named this as a "homogeneous long period distribution" ("hL-distribution").[186] In this model, the σ_i is constrained by the relation $\sigma_i/d_i = \text{const}$, only one width parameter dominates all the others.

Based on the ideal "hL-distribution", the fitting of IDF exhibits considerable deviation from the truth of nanostructure.[200] The deviation from truth suggests that at least two independent width variables should be incorporated into the model. A new principle of the hL-model should be devised.

The ideal hL-model is a superposition of perfect 1D-lattices in sample volume in which a lattice constant can be defined. If we make the lattice constant variable, in the different regions, "the lattice constant is subjected to such a variation that every local lattice can be generated from an 'average local reference structure' by an affine compression or expansion." [200] This principle may be used to describe the general distorted nanostructure.

Set $g_{1r}(r)$ as the IDF of the reference stack which describes the average local ensembles of lamellar stacks. Set $h_H(y)$ be a frequency distribution of compression or expansion factors y which is applied to the reference stack to generate the whole ensembles of scattering stacks. $h_H(y)$ describes the heterogeneity of the sample. Thus, the observed IDF $g_1(r)$ is overlapped by the $h_H(y)$ and $g_{1r}(r)$,

$$g_1(r) = \int_0^{\infty} h_H(y) \frac{1}{y} g_{1r} \left(\frac{r}{y} \right) dy. \quad (2.2.14)$$

After multi-stage mathematical processing and simplification using the properties of Mellin convolution and Fourier transform, one finally obtains the 1D-Fourier-transform

2 Background Knowledge

$F(s)$ of the companded function $f(r)$,

$$F(s) = \sqrt{A(s)} \exp\{-A(s)B(s)\} [\cos\{2\pi isA(s)\} + i \sin\{2\pi isA(s)\}] \quad (2.2.15)$$

with

$$A(s) = \frac{1}{1 + (2\pi\sigma_g\sigma_h s)^2} \quad (2.2.16)$$

$$B(s) = 2\pi^2 (\sigma_g^2 + \sigma_h^2) s^2. \quad (2.2.17)$$

The heterogeneity of ensembles σ_h is got in the reciprocal space, and $\sigma_h \equiv \sigma_H$ can be identified easily. The $\sigma_g \equiv \sigma_i/d_i$ indicates relative deviation of i -th distance distribution. The negative Fourier transform of companded function, $-F(s)$, is proportional to the interference function $G_1(s)$. In the SAXS data analysis, the imaginary part of $F(s)$ is omitted, but the weight of $F(s)$ is doubled. The relative deviation σ_g and d_i can be calculated by fitting $g_1(r)$ which is Fourier transform of the $-F(s)$.

2.3 Comprehending the Magic Square

2.3.1 Fourier Transform

The Fourier transform based on the Fraunhofer approximation is a fundamental transform in the SAXS theory. Fourier transform of 3-dimensional electron density function $\rho_3(\mathbf{r})$ is defined as

$$A(\mathbf{s}) = \mathcal{F}_3(\rho_3)(\mathbf{s}) := \int \rho_3(\mathbf{r}) \exp(2\pi i \mathbf{r} \cdot \mathbf{s}) d^3 r \quad (2.3.1)$$

with i the imaginary unit. The kernel of Fourier transform called harmonic function

$$\exp(2\pi i \mathbf{r} \cdot \mathbf{s}) = \cos(2\pi \mathbf{r} \cdot \mathbf{s}) + i \sin(2\pi \mathbf{r} \cdot \mathbf{s}) \quad (2.3.2)$$

performs an harmonic analysis for the $\rho_3(\mathbf{r})$. There is an orthogonal property for the harmonic analysis.

$$\int_{-\pi}^{\pi} \cos(mx) \cos(nx) dx = \pi \delta_{mn}, \quad m, n \geq 1, \quad (2.3.3)$$

$$\int_{-\pi}^{\pi} \sin(mx) \sin(nx) dx = \pi \delta_{mn}, \quad m, n \geq 1, \quad (2.3.4)$$

$$\int_{-\pi}^{\pi} \cos(mx) \sin(nx) dx = 0 \quad (2.3.5)$$

On the basis of the orthogonal property of harmonic analysis, we can conclude that the Fourier transform extracts the periodic signal, the aperiodic signal is eliminated or reduced by the harmonic analysis. This is meaningful for the periodic stacking of

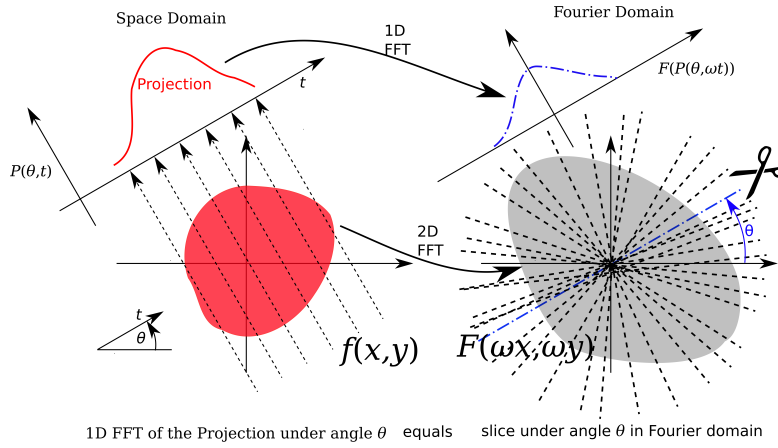


Figure 2.3.1: Schematic diagram of Fourier slice theorem of a 2D function $f(x, y)$. $F(\omega_x, \omega_y)$ is the 2D Fourier transform. The 1D FFT $F(P(\theta, \omega t))$ of projection function $P(\theta, t)$ from the 2D function $f(x, y)$ is equal to the 1D slice of 2D FFT $F(\omega_x, \omega_y)$ of $f(x, y)$.

domains in the semi-crystalline or phase-separated polymer material. The information of repeating units is involved to SAXS curve by Fourier transform. The 1D correlation function and distribution function of chord length computed from the SAXS curve by the inverse Fourier transform reveal the information of repeating units.

2.3.1.1 Projection-slice Theorem

2D scattering pattern collected by a CCD detector is the projected scattering of 3D structure. If we want to investigate the nanostructure in the specific direction, we must take the corresponding data from the 2D SAXS pattern. What we must bear in mind first is that the $I(\mathbf{s}_i)$ can not reflect the $\rho(\mathbf{r}_i)$ directly and plainly. How to take the curve in the specific direction from the SAXS pattern is indicated by Fourier slice theorem. “In n -dimensional (n D) space, Fourier transform F_m of the projection P_m of an n D function $f_n(\mathbf{r})$ onto an m D linear submanifold is equal to an m D slice S_m of the n D Fourier transform F_n of that function $f_n(\mathbf{r})$. F_n consists of an m D linear submanifold that is passing through the origin of the Fourier space and parallel to the projection submanifold P_m .” [215] Projection-slice theorem can be displayed in operator terms,

$$F_m P_m = S_m F_n. \quad (2.3.6)$$

Figure 2.3.1 sketches the Fourier slice theorem applied on a 2D function $f(x, y)$. The projection function $P(\theta, t)$ on the angle θ subjected to the 1D FFT results in the $F(P(\theta, t))$ which is also a slice from the 2D FFT $F(\omega_x, \omega_y)$ of $f(x, y)$. The dot-dashed curve indicates the slice from the 2D FFT $F(\omega_x, \omega_y)$ of $f(x, y)$.

In order to clarify the projection-slice theorem applied in the 2D SAXS pattern, a mathematical proof of 2D Fourier slice theorem is presented by projection in the specific

2 Background Knowledge

directions x -axis or y -axis which indicates the longitudinal axis and transversal axis in the nanofibril structure. Let's assume $f(x, y)$ a 2D function, the projection of $f(x, y)$ onto the x -axis is $P(x)$.

$$P(x) = \int_{-\infty}^{+\infty} f(x, y) dy \quad (2.3.7)$$

The Fourier transform of $f(x, y)$ is

$$\mathcal{F}(k_x, k_y) = \int_{-\infty}^{+\infty} \int_{-\infty}^{+\infty} f(x, y) e^{-2\pi i(xk_x + yk_y)} dx dy. \quad (2.3.8)$$

The slice $s(k_x)$ is

$$s(k_x) = \mathcal{F}(k_x, 0) = \int_{-\infty}^{+\infty} \int_{-\infty}^{+\infty} f(x, y) e^{-2\pi i x k_x} dx dy \quad (2.3.9)$$

$$= \int_{-\infty}^{+\infty} \left[\int_{-\infty}^{+\infty} f(x, y) dy \right] e^{-2\pi i x k_x} dx \quad (2.3.10)$$

$$= \int_{-\infty}^{+\infty} P(x) e^{-2\pi i x k_x} dx. \quad (2.3.11)$$

which is the Fourier transform of $P(x)$. If the projection is onto y -axis, the proof process is same.

When the Fourier slice theorem is applied on the nanostructure determination from the 2D SAXS fiber pattern, Extracting the nanostructure from projection of SAXS pattern is performed by Bonart firstly.[216] One example to extract nanostructure from SAXS fiber pattern is shown in Figure 2.3.2. The projections onto different directions perform the statistics of different chords penetrating the two-phase structure. Vertical (Longitudinal) projection

$$\{I\}_1(s_3) = 2\pi \int_0^{\infty} s_{12} I(s_{12}, s_3) ds_{12} \quad (2.3.12)$$

perform the statistics of those chords passing the two-phase system in the direction parallel to the fiber axis. Walking along such a chord, we will go through the hard domain and soft domain alternately. The domain size and its distribution can be extracted from the statistics of chord length and its distribution which are computed from the interface distribution function. Vertical projection in Figure 2.3.2 exhibiting a discrete scattering peak indicates the strong vertical correlation among domains. The horizontal projection of a fiber pattern

$$\{I\}_2(s_{12}) = 2 \int_0^{\infty} I(s_{12}, s_3) ds_3 \quad (2.3.13)$$

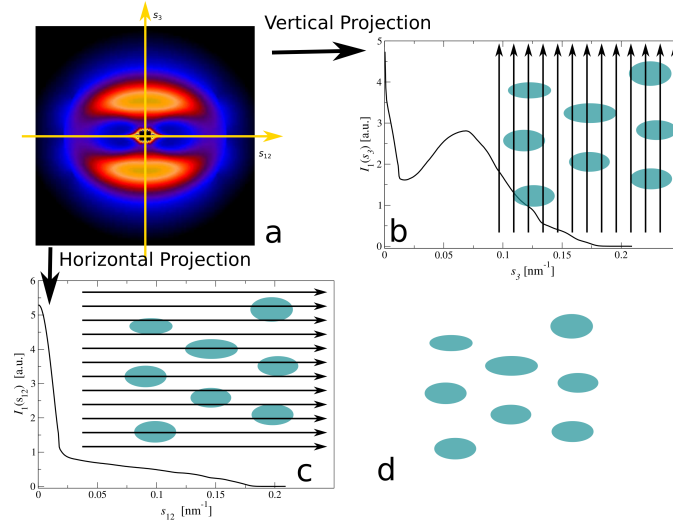


Figure 2.3.2: Vertical and lateral correlation of domains (d) analyzed by projecting the 2D SAXS (a). Vertical projection and horizontal projection indicate the domain correlation in the straining direction and lateral direction. $I_1(s_3)$ (b) exhibiting the discrete peak indicates the vertical periodic stacking of domains, $I_1(s_{12})$ (c) exhibiting a monotonous decay indicates the little lateral correlation among domains. The straining direction is vertical.

indicates the statistics of lateral correlation of fiber-like domains. The monotonous decay of horizontal projection indicates little lateral correlation among nanofibrils.

2.3.1.2 Spatial Frequency Filter

The inhomogeneities of different phases in PUE scatter the X-ray at small angle, the inhomogeneities inside certain phase or ambiguous boundary between two phases scatter the X-ray at large angle whose scattering effects is always accompanying with the scattering at small angle. The polydispersity effect is reflected at moderate angle. The scattering effects generated by the essential imperfection of material is called background of scattering pattern or parasitic scattering. When we investigate the polymer with high disorder, the scattering peak is a broad halo with strong background scattering. With the basic understandings of scattering theory, extracting the topology of polymer can be considered as a plain problem of signal processing. The measured SAXS intensity taken as the power spectrum has three distinct spatial bands. Background scattering is in the low spatial frequency, the noise is in the high spatial frequency because of lacking long-range order. The moderate spatial frequency covers the information of disordered topology. It's hard to deduce the analytic formula for the background scattering. Fortunately, the background scattering can be eliminated by a self-adapting spatial frequency filtering.[217, 193] This filter facilitates to determine the interference function $G_f(\mathbf{s}) \approx mG(\mathbf{s})$, with $m < 1$ being an unknown that presents the loss in the filter, and

2 Background Knowledge

with $G(\mathbf{s})$ being the true interference function. In practice, a constant fluctuation function is subtracted from the raw data scattering intensity $I(s) - c_{Fl}$, then it is transformed by specific power of scattering vector $s^n (I(s) - c_{Fl})$. A low-pass filter is employed to obtain the background. The interference function is received after subtraction of background and multiplication by the Hanning filter.

The Butterworth low-pass filter designed by a British engineer Stephen Butterworth in 1930[218] is applied to filter the high frequency noise. Equation 2.3.14 shows the 1st-order low-pass Butterworth filter applied on the interference function $I_L(\mathbf{s})$

$$f_{\ell, r_c} [I_L(\mathbf{s})] = \mathcal{F}^{-1} \left\{ \mathcal{F} [I_L(\mathbf{s})] (\mathbf{r}) / (1 + r/r_c)^2 \right\} \quad (2.3.14)$$

where r_c is the cutoff spatial frequency and \mathcal{F} is the multidimensional Fourier transform.

If the phase boundary is strongly rough, the iteration of this low-pass filter can be applied to remove the scattering effect of domain surfaces. Inevitably it also eliminates the scattering of tiny domains. Thus, we must bear in mind what we do when we apply the iteration of this filter.[219]

2.3.2 Gradient

The gradient denoted as $\nabla f \equiv \text{grad } f$ is expanded by

$$\nabla f(\mathbf{r}) = \sum_{i=1}^3 \frac{\partial f}{\partial r_i} \mathbf{r}_i \quad (2.3.15)$$

in the Cartesian coordinate. The gradient which is similar to the usual derivative represents the slope of the tangent of the graph of the function f . In the morphology of PUE, the gradient of electron density function enhances the edge effects of certain phase. In the ideal phase, the gradient of density inside this phase should be zero, only at the phase boundary, the gradient is not zero, but an infinite number. For the real morphology of PUE, the gradient values are finite numbers as the heterogeneities are quite universal.

2.3.3 Comparison of Convolution and Correlation Function

In the scattering theory, one-dimensional particle size distribution modeled by convolution is established by Hosemann.[196] The concept convolution is very common in the polymer science whose inherent characteristic is polydispersity. The convolution of two function f and g is designated as asterisk $*$

$$(f * g)(t) := \int_{-\infty}^{\infty} f(\tau) g(t - \tau) d\tau. \quad (2.3.16)$$

If f and g are same, the definition of convolution can be displayed as

$$(f * f)(t) = \int_{-\infty}^{\infty} f(\tau) f(t - \tau) d\tau. \quad (2.3.17)$$

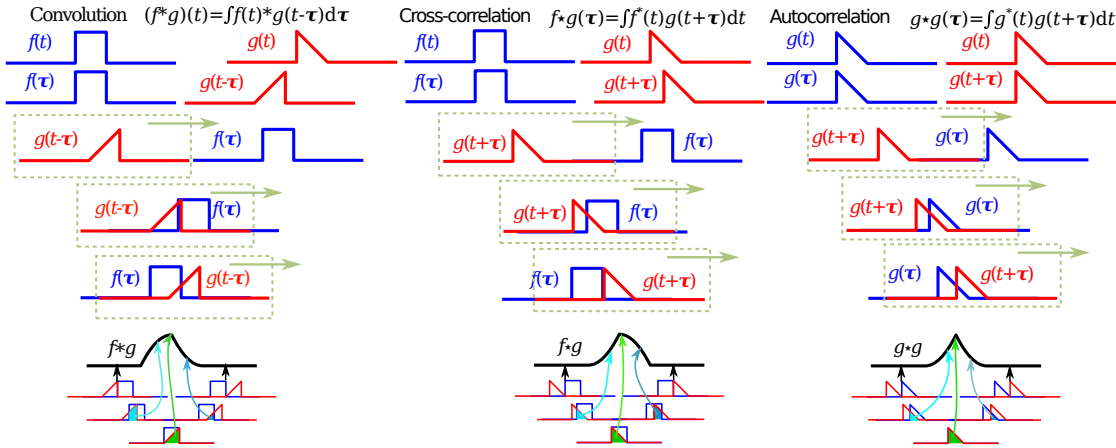


Figure 2.3.3: The comparison between convolution, cross-correlation and autocorrelation. The most obvious difference of f and g between convolution and cross-correlation is the flip operation performed in convolution. This figure is replotted referring to an online figure.[220]

This function is similar to the autocorrelation function 2.2.1 but with a flip operation.

In order to clarify the differences between them, Figure 2.3.3 shows the comparisons of convolution, cross-correlation, and autocorrelation. The correlation function or convolution of two functions is proportional to the integral (shaded area) of f and the shifting function g . In the convolution, we must perform a horizontal flip on g function first, the superposition of f and flipped g is the convolution. The cross-correlation is computed from the superposition of f and shifting g . The autocorrelation function is a cross-correlation function of one function and its shifting ghost function.

2.3.4 Lorentz Correction

In the misorientation or isotropic scattering, the Lorentz correction[221, 193] applied on the scattering intensity is mandatory in order to measure the real distance between two lamellae which is normal to the lamella plane. Figure 2.3.4 shows the schematic diagram of Lorentz correction applied on the scattering intensity of misorientation material. We assume a lamella whose thickness and extension radius of lamella is T and R ($R \gg T$) respectively. Its ideal scattering pattern should be a narrow cylinder with diameter $1/2R$ and length $1/T$. For the lamella with parallel and infinitely extended layers, its scattering pattern shrinks onto a line whose scattering intensity can be defined as $I_1(s_3)$ in s and $-s$ direction. The long-period of layers can be determined by reciprocity law from the scattering peaks without any doubt. However, for the isotropic distribution of lamellae orientation (shown in subfigure (a)), $I_1(s_3)$ must be isotropized by solid-angle accumulation from the half spherical shell with radius s that results from the observed intensity, $I(s)$. Accumulation from the half shell not the full shell is due to summing

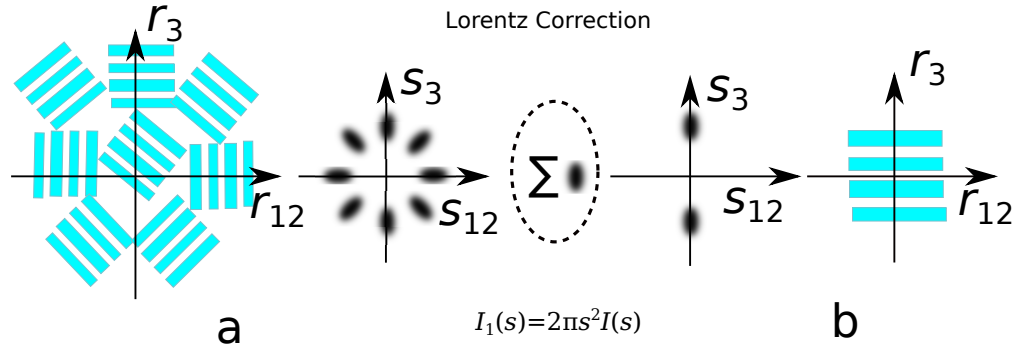


Figure 2.3.4: Schematic diagram of Lorentz correction for the misorientation or isotropic material. (a) The misorientation of lamellar packing of domains generates the isotropic scattering. Two spots on the meridian (b) are accumulated (dashed ellipse) from intensity on the spherical shell of s . The summed scattering spots indicates the distance between lamellae that is normal to the lamella surface.

intensity for s and $-s$ dividually. The 1D $I_1(s)$ intensity

$$I_1(s) = 2\pi s^2 I(s) \quad (2.3.18)$$

can be obtained by Lorentz correction from the observed intensity $I(s)$. This simple equation connects the isotropic material and perfectly oriented structural entities. What we must bear in mind is that the Lorentz correction is only valid for the scattering of isotropic material with lamellar structure (dilute solution) and the range of s must be kept in the range $s > 1/R$.

Comparison between Lorentz Correction and Vertical Projection. The Lorentz correction applied on the isotropic material with a lamellar domain structure ($I_1(s_3) = 2\pi s_3^2 I(s_3); s_3 \equiv s$) and the analysis of Bonart's longitudinal projection are related to each other closely.[222] Both of them indicate the 1D structure in the physical space. If we view the Lorentz correction in the mathematical point, it only can be applied in the isotropic material with lamellar structure. The vertical projection can be applied in the general structure. From the physical point, the long-spacing computed from the curve subjected to Lorentz correction is the distance normal to the lamellae plane. The vertical projection extracts the average long-spacing of well-oriented system. Both of their intensities fall off in Porod's law with s_3^{-2} as both of them measure the nanostructure of same entities.

3 Experimental

3.1 Materials

3.1.1 Materials Investigated in Section 4.1

We study thermoplastic polyurethanes (TPU) made from different components. The hard segments of all materials are made from 4,4'-methylene diphenyl diisocyanate (MDI). The chain extenders are 1,4-butanediol (BD) or hydroquinone bis(2-hydroxyethyl) ether (HQEE), respectively. The soft segments are either made from polytetrahydrofuran (PTHF[®] PTHF is a trade mark of BASF SE) or from polycaprolactone (PCL) or from an adipic ester. The molar masses of all the soft segments are close to $M_n \approx 1000$ Da. $M_w/M_n \approx 1$ for PCL. $M_w/M_n \approx 2$ for PTHF[®] and the adipic ester.

The raw materials have been produced by BASF and all TPUs have been synthesized by BASF Polyurethanes Ltd in Lemförde, Germany by hand-casting in a one-shot process. The materials have been milled and injection molded to sheets of 2 mm thickness. Afterwards they have been matured [1, 223, 155, 113, 224, 225, 226] by annealing at 100 °C for 20 h.

Table 3.1 presents characterizations of the materials. σ_{max} and ε_b have been determined in tensile tests run at a strain rate of $\dot{\varepsilon} \approx 0.67 \text{ min}^{-1}$. The hard segment content is calculated according to

$$\text{HSC} = \frac{n_{chain\ extender} (M_{chain\ extender} + M_{diisocyanate})}{m_{total}}$$

whilst neglecting the second terminal diisocyanate.

3.1.2 Materials Investigated in Section 4.2

The PUE material is supplied by BASF Polyurethane Ltd in Lemförde, Germany. It's synthesized from 4,4-methylene diphenyl diisocyanate (MDI), polytetrahydrofuran (PTHF) with molecular weight $1000 \text{ g}\cdot\text{mol}^{-1}$ and 1,4-butanediol (BD) as chain extender. The hard phase is buildup of MDI and BD, while MDI and PTHF form the soft phase. The content of hard segment (MDI+BD) is about 43%wt.

The virgin sample is annealed at 100 °C for 20 hours. Antioxidant and anti-uv stabilizers (1 ppm) are added into the raw material to protect its chemical stability. The stabilizers don't influence the mechanical property significantly. The ageing experiments are carried out in the circulating air chamber at 150 °C. They were taken out after different ageing days.

In our study, the thermal-ageing temperature is higher than 100 °C that is the evaporation temperature of liquid water, therefore ignoring ageing effect of moisture is rational.

3 Experimental

Table 3.1: Samples and their characterization. ρ : mass density, σ_{max} : tensile strength, ε_b : elongation at break, $M_{w,TPU}$: weight-average molecular mass of the polymer, $X_{iso,TPU}$: isocyanate content of the polymer. All materials share the same hard-segment content HSC=51%.

labeling	mbt	mqt	mbl	mql	mba	mqa
hard segment	MDI	MDI	MDI	MDI	MDI	MDI
chain extender	BD	HQEE	BD	HQEE	BD	HQEE
soft segment	PTHF	PTHF	PCL	PCL	adipic ester	adipic ester
ρ [g/cm]	1.172	1.185	1.215	1.23	1.239	1.255
Shore D	65	64	71	75	71	74
σ_{max} [MPa]	54	40	42	33	42	34
ε_b	5.0	4.6	4.9	3.9	5.6	4.7
$M_{w,TPU}$ [kDa]	88	55	103	54	80	66
$X_{iso,TPU}$ [%]	0.06	0.10	0.04	0.04	0.04	0.08

Table 3.2: Materials and parameters that characterize their chemistry. In the sample designation the letter following the dash mimics the topology of the polyol. HSC is the hard segment content. With respect to the polyols, f is their functionality, v_{OH} is the hydroxyl value. M_{th} is the theoretical molecular weight as computed from v_{OH} , and $M_e = M_{th}/f$ is the equivalent molar mass

material	HSC [wt%]	f	v_{OH} [mgKOH/g]	M_{th} [g/mol]	M_e [g/mol]
PU-I	31	2	55.0	2000	1020
PU-Y	30	3	42.0	4000	1340
PU-X	30	4	41.0	5500	1370
PU-Hl	30	4	51.5	4400	1140
PU-Hs	32	4	96.5	2300	580

We have measured wide-angle X-ray scattering (WAXS) of all the samples. All samples show a broad amorphous halo with a maximum at $2\theta \approx 20.5^\circ$. No crystallites are formed during the long-term ageing.

3.1.3 Materials Investigated in Section 4.3

Polypropylene polyols have been synthesized via anionic polymerization using cesium hydroxide as a catalyst. Figure 3.1.1 shows the architecture of the polyols in schematic representations. The distance between the dotted lines represents a molecular weight of 2000 Daltons. The lengths of the solid lines that indicate the molecular structures are proportional to the molecular weights of the polyol segments. In Table 3.2 the composition of the materials and their polyols are characterized. The polyols are described by their functionality f , OH-value, and theoretical molecular weight M_{th} . Also the equiva-

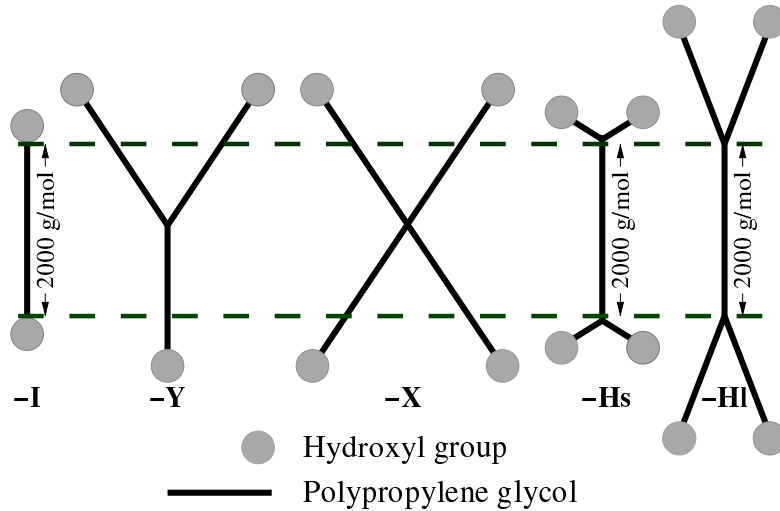


Figure 3.1.1: Architecture of the polyols. The lengths of the solid lines are proportional to the molar masses of the polypropylene glycol. From the left: Linear ($f=2$); trifunctional ($f=3$); tetrafunctional, X-shaped ($f=4$); tetrafunctional, H-shaped with short arms; and tetrafunctional, H-shaped with long arms

lent molecular weight $M_e = M_{th}/f$ is given.

The PUEs are produced from polyether polyols made from propyleneoxide, 1,4 butane diol and 4,4'-methylene diphenyl diisocyanate (MDI). The MDI is a common prepolymer used in the commercial production of PUE. It contains some short chain diols and uretdione groups. The latter introduce some crosslinking via the isocyanate, but its contribution to the overall level of crosslinking is considered to be small. M_e of isocyanate is 160 Daltons. 1,4-butanediol has the $M_e=45$ Daltons. PUE recipes have been calculated such that the hard segment content (HSC) is amounting to approximately 31 wt.-%. HSC has been calculated from: $HSC = (\text{weight MDI} + \text{weight chain extender}) / (\text{weight polyol} + \text{weight MDI} + \text{weight chain extender})$. The molar ratio of isocyanate to hydroxyl groups amounts to 1.00. Because the polyols employed are branched (with the exception of polyol I) and the isocyanate is slightly branched, a polymer network is obtained with an infinite molecular weight. As the molar ratio of isocyanate and polyol is 1:1, there is no tendency to form side products like allophanate. All raw materials have been obtained from BASF SE. The isocyanate has been used as received. Prior to the preparation of the cast elastomer, both the polyol and chain extender, have been dried under vacuum at room temperature for 2 h. The polyol, an anti-foaming agent, a mercury catalyst, and chain extender have been mixed and homogenized in a speed mixer at 2000 rpm for 2 min. Subsequently the isocyanate has been added and the components have been mixed for another 2 min at 2000 rpm. The reactive mixture has been poured into an aluminum mold (150 mm \times 200 mm \times 2 mm) at 70 °C. The casting has been remolded after approx. 5 min. Finally the casts have been post-cured in an air-circulated oven for 4 h at 80 °C. The PU castings have been kept at least one week

3 Experimental

at room temperature prior to measurement.

3.2 Wide Angle X-ray Scattering

All the wide angle X-ray scattering (WAXS) scans are carried out in a powder diffractometer X'Pert Pro MPD manufactured by PANalytical in Bragg-Brentano geometry with a wavelength $\lambda = 0.1542$ nm (Cu- k_α). The scanning range of 2Θ is from 2° to 42° with step 0.001° .

3.3 Transmission Electron Microscopy

For transmission electron microscopy (TEM) an ultra-thin frozen section has been prepared. The contrast of sample has been enhanced by RuO_4 staining of the soft phase. Then an image has been taken using Zeiss Libra 120 electron microscope.

3.4 Fourier Transform Infrared Spectroscopy (FTIR)

Infrared tests were performed in Attenuated Total Reflectance (ATR) mode using a Nicolet iS10 spectrometer (Thermo Scientific). The spectra were collected in extinction mode within a wavenumber range from 650 to 4000 cm^{-1} at a resolution of 5 cm^{-1} for 16 scans.

3.5 Tensile Testing

The samples were extended by the stretching machine but in different synchrotron facilities. The results described in Section 4.1 is carried out at DESY. The results described in Section 4.2 and Section 4.3 were carried out at BESSY II.

3.5.1 Tensile Testing at DESY

Tests are run on a self-made machine at room temperature.[227] Dogbone-shaped test bars S3 according to DIN53504 are punched from the sheet. The clamping distance is 22.5 mm. A 1000 N load cell is used. A TV-camera is employed to monitor the motion of the fiducial marks. Video frames are grabbed every 12 s. Stretching speed is 1 $\text{mm}\cdot\text{min}^{-1}$. Figure 3.5.1 sketches the front-end of X-ray and in-situ tensile setup. Figure 3.5.1(a) sketches the front end where X-ray is generated, guided and wavelength-adjusted from synchrotron facility. Figure 3.5.1(b) sketches the tensile devices. The dogbone-shaped sample is mounted between two clamps with load cell.

Using the fiducial marks close to the beam irradiation spot, the local macroscopic strain $\varepsilon = (\ell - \ell_0) / \ell_0$ is computed from the initial distance, ℓ_0 , of the fiducial marks and the respective actual distance, ℓ . The true stress σ is computed by $\sigma = F/A$, F designates the real-time force and A computed by $A = A_0 / (\varepsilon + 1)$ is the estimated dynamic sample cross-section. A_0 is the initial cross-section of the central part of the test bar. Figure

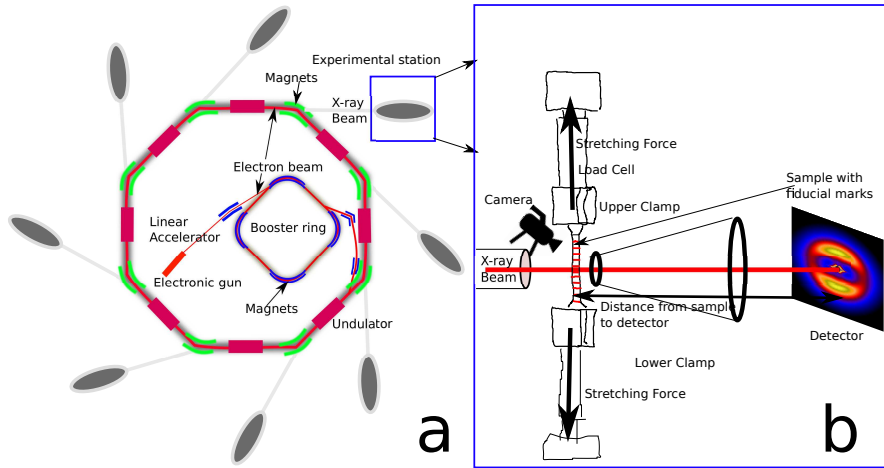


Figure 3.5.1: Experimental devices for the tensile experiments. (a) The front-end of experimental station where X-ray is generated, guided and wavelength-adjusted. (b) The in-situ tensile machine and detector.

3.5.2 shows the algorithm to determine the stress-strain in the current thesis. During the straining, the pigment on the mark could be discretized and some area of the mark can't be covered by pigment, therefore, the reference point of strain set by the gravity center of mark guarantees the reference point in the center of the mark. The distance between two marks set as the relative reference distance to calculate the strain. The stress is calculated with respect to the in-situ cross-section area of sample by assuming the constant volume during straining. All the procedures can be downloaded from the website.[228]

3.5.2 Tensile Testing at BESSY II

Tests are run in a self-made[227] machine. A grid of fiducial marks is printed[229] on test bars S3 (DIN 50125). The sample thickness is $\delta_0 = 2.0$ mm. The clamping distance is 21 mm. Signals from the transducer are recorded during the experiment. The sample is monitored by a TV-camera. Video frames are grabbed every 60 s and are stored together with the experimental data. The machine is operated at cross-head speeds of 1 mm/min. Using the fiducial marks, the local macroscopic strain $\varepsilon = (\ell - \ell_0)/\ell_0$ at the position of X-radiation is computed from the initial distance, ℓ_0 , of two fiducial marks and the respective actual distance, ℓ . Processing all the video frames yields the curve $\varepsilon(t)$ as a function of the elapsed time. It is very well approximated by a quadratic polynomial. The local strain rate is kept low $\dot{\varepsilon} \approx 1.3 \times 10^{-3} \text{ s}^{-1}$ in order to be able to monitor the straining process using the old-fashioned detector. The stress data was not recorded associated with the strain as the load cell didn't work at the beamtime. The strain data as a function of elapsed time is also computed according to the theory shown in Figure 3.5.2.

3 Experimental

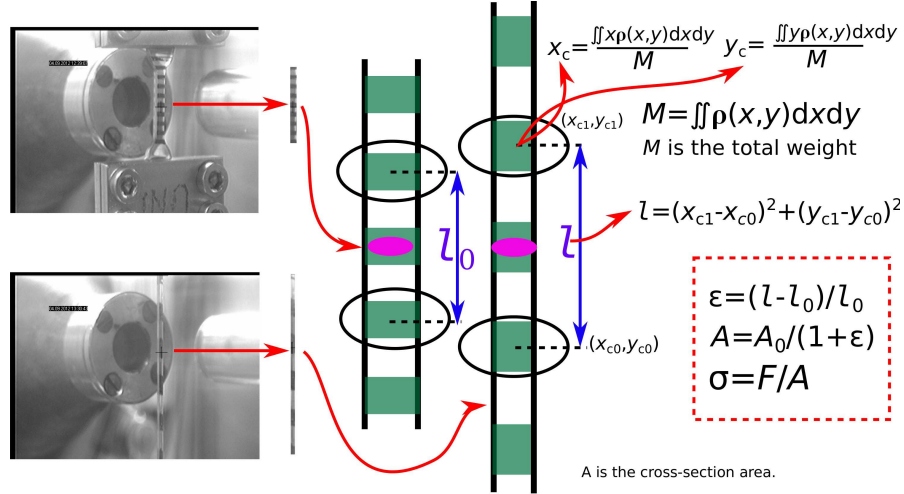


Figure 3.5.2: Stress-strain determination from the fiducial marks. The gravity center of mark is taken as the reference point. The constant volume during straining is assumed.

3.6 SAXS Setup

The experiments for different samples were carried out in different synchrotron facilities. The results described in Section 4.1 is carried out at DESY. The results described in Section 4.2 and Section 4.3 were carried out at BESSY II.

3.6.1 Experiments Carried out at DESY

Small-angle X-ray scattering (SAXS) experiments are carried out in the synchrotron beamline A2 at HASYLAB, Hamburg, Germany. The sample-detector distance is 3022 mm. Wavelength is $\lambda = 0.15$ nm. Scattering patterns are collected by a 2D marccd 165 detector (mar research, Norderstedt, Germany) using binned 1024×1024 pixel mode (pixel size: $158 \mu\text{m} \times 158 \mu\text{m}$). Scattering patterns of undrawn and relaxed sample are recorded with 120 s exposure. Scattering patterns of plain stretching have been recorded every 132 s with one exposure of 120 s. In the cyclic loading experiments scattering patterns have been recorded every 60 s with one exposure of 48 s. The patterns $I(\mathbf{s}) = I(s_{12}, s_3)$ cover the region $-0.175 \text{ nm}^{-1} \leq s_{12}, s_3 \leq 0.175 \text{ nm}^{-1}$. $\mathbf{s} = (s_{12}, s_3)$ is the scattering vector with its modulus defined by $|\mathbf{s}| = s = (2/\lambda) \sin \theta$ with 2θ being the scattering angle.

3.6.2 Experiments Carried out at BESSY II

Small-angle X-ray scattering (SAXS) is carried out in the synchrotron beamline 7T-MPW-SAXS at BESSY II, Berlin operated in top-up mode with a ring current of 300 mA. Then the 7-Tesla multipole-wiggler delivers a photon flux of $6 \times 10^{12} \text{ s}^{-1}$. The downstream

optics is optimized for setups with a sample-detector distance in the typical SAXS range of 3 m. The chosen primary-beam cross-section is 1 mm \times 0.4 mm (width \times height), the sample-detector distance is 2854 mm as determined by calibration with Ag-Behenate (long period $d_{001} = 5.8380$ nm) and the photon energy of 8310 keV, equivalent to the wavelength $\lambda = 0.1492$ nm. A filter package in the primary beam is engaged in order to limit the count rate in the detector. The intensity ratios of different filter settings are measured for later compensation. The detector is a 2D gas detector (multi-wire proportional counter) built by JJ X-ray, Kgs. Lyngby, Denmark. It has 1024×1024 pixels of $207 \mu\text{m} \times 207 \mu\text{m}$. Scattering patterns are recorded every 240 s with an exposure of 140 s. The patterns $I(\mathbf{s}) = I(s_{12}, s_3)$ cover the region $-0.24 \text{ nm}^{-1} \leq s_{12}, s_3 \leq 0.24 \text{ nm}^{-1}$. $\mathbf{s} = (s_{12}, s_3)$ is the scattering vector with its modulus defined by $|\mathbf{s}| = s = (2/\lambda) \sin \theta$. 2θ is the scattering angle. The smallest s -values recorded close to the central beam stop is $s_{min} = 0.0125 \text{ nm}^{-1}$. The remnant small blind area in the center is filled by extrapolation. Before any processing the patterns are corrected for the uneven detector sensitivity which has been measured using a radioactive Ni-target.

3.7 Data Evaluation

Data Pre-processing. The scattering patterns $I(s_{12}, s_3)$ are normalized, background corrected, aligned as described in Stribeck's textbook.[193] These procedures contain intensity normalization for constant primary beam flux, zero absorption, and constant irradiated volume V_0 . The correction has been carried out assuming $V(t)/V_0 = (1/(1 + \varepsilon(t)))^{0.5}$. This equation is based on the constant volume during straining. The strain $\varepsilon(t)$ that is associated to each scattering pattern is related to the time $t + t_e/2$ with t being the elapsed time at the start of the exposure, and t_e the total exposure of the pattern. After these steps the resulting scattering patterns are still not in absolute units, but their intensities can be compared relatively to each other.

Extrapolation is carried out by the radial-basis function algorithm[230] that is implemented in PV-WAVE Fig. 3.7.1 shows a pattern before and after preprocessing.

The patterns $I(\mathbf{s}) = I(s_{12}, s_3)$ are transformed into a representation of the nanostructure in real space. The only assumption is presence of a multiphase topology. The result is a multidimensional chord distribution function (CDF), $z(\mathbf{r})$ [5]. The method is exemplified in a textbook[193] and in the original paper[5] where figures show the change of the pattern from step to step. Here we only summarize the steps and introduce the important quantities. The CDF with fiber symmetry in real space, $z(r_{12}, r_3)$, is computed from the fiber-symmetrical SAXS pattern, $I(s_{12}, s_3)$, of a multi-phase material. In order to compute $z(r_{12}, r_3)$, $I(s_{12}, s_3)$ is projected on the representative fiber plane. Multiplication by s^2 applies the real-space Laplacian. The density fluctuation background is determined by low-pass filtering. It is eliminated by subtraction. The resulting interference function, $G(s_{12}, s_3)$, describes the ideal multiphase system. Its 2D Fourier transform is the sought CDF. In the historical context the CDF is an extension of Ruland's interface distribution function (IDF)[184] to the multidimensional case or, in a different view, the Laplacian of Vonk's multidimensional correlation function[198].

3 Experimental

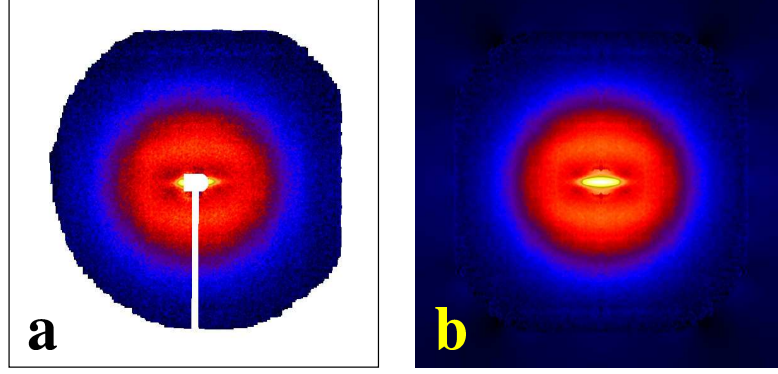


Figure 3.7.1: Effect of pattern preprocessing. (a) raw valid data. The sensitive region is limited by the detector edge and the vacuum tube. The central beamstop and its holder define an inner blind region. (b) The same pattern after preprocessing. Noise reduction by four-quadrant averaging is visible. Both patterns are on a logarithmic pseudo-color intensity scale

The CDF is an “edge-enhanced autocorrelation function”[141, 173, 231, 190] – the autocorrelation of the gradient field, $\nabla\rho(\mathbf{r})$. $\rho(\mathbf{r})$ is the electron density inside the sample that is constant within a domain (crystalline, amorphous). Thus as a function of ghost displacement \mathbf{r} , the multidimensional CDF $z(\mathbf{r})$ shows peaks wherever there are domain *surface contacts* between domains in $\rho(\mathbf{r}')$ and in its displaced ghost $\rho(\mathbf{r}' - \mathbf{r})$. Such peaks $h_i(r_{12}, r_3)$ are called distance distributions.[184] Distance $\mathbf{r} = (r_{12}, r_3)$ is the ghost displacement. In this paper we are mainly studying the evolution of the strong meridional long-spacing peaks $h_L(r_{12}, r_3)$ in the CDF.

Bonart’s Longitudinal Projection. The best-known projection in the field of scattering maps the intensity $I(\mathbf{s})/V$ that is normalized to the irradiated volume, V , onto the zero-dimensional subspace. The resulting number Q is known as “invariant” or “scattering power”

$$\{I\}_0/V = Q = \int I(\mathbf{s})/V d^3s. \quad (3.7.1)$$

Bonart’s longitudinal structure is obtained by not integrating over the whole reciprocal space, but only over planes normal to the fiber axis yielding the curve

$$\{I\}_1(s_3)/V = 2\pi \int_0^\infty s_{12} I(s_{12}, s_3)/V ds_{12}, \quad (3.7.2)$$

which is a function of the straining direction s_3 only. This is a projection onto a 1D subspace as indicated by subscripting to the pair of braces. Projections are computed from normalized data according to Fig. 3.7.1a after 4-quadrant averaging and filling of the central hole.

From such projections interface distribution functions (IDF)[193, 184, 222] $g_1(r_3)$ are

computed for further analysis. In this way it becomes possible to quantify several morphological parameters.

Technically, the first step involves subtraction of a guessed constant density fluctuation background[232, 231, 233], I_{Fl} , from the measured curve and multiplication by $4\pi^2 s_3^2$ to apply the second derivative in reciprocal space. The result is an intermediate interference function

$$G_{1,i}(s_3) = (\{I\}_1(s_3)/V - I_{Fl}) 4\pi^2 s_3^2.$$

The final background is constructed by application of a narrow low-pass frequency filter to $G_{1,i}(s_3)$, as is described elsewhere[217, 193]. Thus the interference function $G_1(s_3)$ is obtained. Its one-dimensional Fourier transform is the longitudinal IDF $g_1(r_3)$.

IDF Fitting in Section 4.1. The IDF is fitted[222] by a one-dimensional model that describes the arrangement of alternating hard-domain heights and soft-domain heights along the straining direction. Visual inspection of the computed IDFs shows that the height distributions of hard domains can be modeled by Gaussian functions and that the range of correlation among the domains is short. Thus a short-range stacking model[222] with few parameters is chosen, which is a variant of the ideal stacking model[195]. The parameters of the model are a weight W that is related to the volume fraction of contributing chords (cf. Figure ??), average heights \bar{H}_h and \bar{H}_s of hard and soft domains, respectively, and the relative standard deviations σ_h/\bar{H}_h and σ_s/\bar{H}_s of the domain height distributions. An additional parameter that skews[200, 202] the Gaussians is present but not discussed here.

IDF Fitting in Section 4.2. The IDF is fitted[222, 200, 217] by a one-dimensional model that describes the arrangement of alternating hard-domain heights and soft-domain heights along the straining direction. An adapted model is constructed under consideration of information which is collected by visual inspection of the CDFs and the IDFs themselves. Anticipating the information content of the CDFs (Figure 4.2.3) it is clear that the mid-range correlations among hard domains are governed by arrangements that do not continuously lengthen in the straining experiment. The arranged domains appear[234] to form quasiperiodic sequences. Such arrangements cannot be described by the common models of short-range correlated entities which are based on the convolution polynomial (paracrystal, stacking model, ...)[195].

Fortunately the scattering effect of the higher quasi-periodic sequences is low. Thus we neglect it to the first approximation by modeling only next-neighbor correlations. An appropriate model describes an entity which comprises only two hard-domains with a single soft-domain in between (“duos”[193, 235]). The hard domains are described by a hard-domain height-distributions, and the soft domain in between by a soft-domain height-distribution.

Moreover, the scattering effect of uncorrelated hard domains (“solos”[193, 235, 89, 61]) must be considered. It is pure, diffuse particle scattering which originates from those hard domains which are randomly placed in the material (“solos”[193, 235]). In earlier work[61, 236] we have called the corresponding regions in the material (“poorly arranged

3 Experimental

regions” (PAR)). Correspondingly, the duos are identified by the former “well arranged entities” (WAE)[61, 236].

Thus our ultimate model comprises two components, namely solos and duos. This is similar as in earlier work[235], but here the two components are not coupled by their corresponding volume fraction. Instead, here we couple solos and duos by assuming that the height-distributions of isolated and correlated hard domains are the same. This assumption appears to be reasonable, because in polyurethane materials the correlation among the hard domains is extremely low, and thus a disproportions of the hard-domain height-distributions appears improbable.

It appears worth to be mentioned that we have fitted other two-component models as well and have even varied the parameter coupling between them. The ultimate model presented here exhibits the best separation of the morphological parameters (narrow error bars, low noise of the obtained curves as a function of strain).

Let us present the model parameters. The parameters of the duo component are a weight W_{duo} , average heights \overline{H}_h and \overline{H}_s of hard and soft domains, respectively, and the relative standard deviations σ_h/\overline{H}_h and σ_s/\overline{H}_s . A further standard deviation σ_H permits skewed height distributions[200, 202]. Addition of the solo component adds only one further parameter, W_{solo} . It borrows \overline{H}_h , σ_h/\overline{H}_h and σ_H from the duos. In the fitting procedure intervals of confidence are reported, and the corresponding numbers show that for the aged materials the widths of the domain-height distributions (σ_h/\overline{H}_h , σ_s/\overline{H}_s , σ_H) are too uncertain to be discussed. This is a consequence of the highly distorted morphology.

Let us discuss the morphological meaning of the parameters which return significant results. $W_{solo}\overline{H}_h$ and $W_{duo}\overline{H}_h$ are proportional to the volume fraction of uncorrelated and correlated hard domains, respectively. Summed up

$$(W_{solo} + W_{duo})\overline{H}_h = cv_h \quad (3.7.3)$$

we compute a quantity which is proportional to the volume fraction of hard domains, v_h . Unfortunately, the morphology of our TPUs is a diluted one, i.e. the parameter $W_{duo}\overline{H}_s$ does not catch all soft chords[181]. Only in a concentrated system $W_{duo}\overline{H}_s = cv_s$ would be valid. Then it would be possible to eliminate c . Nevertheless, we can report cv_h . Fortunately, proper normalization guarantees that c is the same for all the recorded SAXS patterns. The meaning of \overline{H}_h and \overline{H}_s is obvious.

Figure 3.7.2 shows a decomposition of $g_1(r_3)$ into the two model components. The fit appears to be good. Due to the finite character of both components, curve oscillations cannot be fitted which occur outside the second upturn of $g_1(r_3)$ (in Figure 3.7.2 for $r_3 > 20$ nm).

Fitted Parameters and Hard Domain Volume. By fitting the IDF, we determine the height distributions $H_h(r_3)$ and $H_s(r_3)$ of hard and soft domain chords, respectively. The weight parameter of the IDF is defined

$$W = \int H_h(r_3) dr = \int H(r_3) dr. \quad (3.7.4)$$

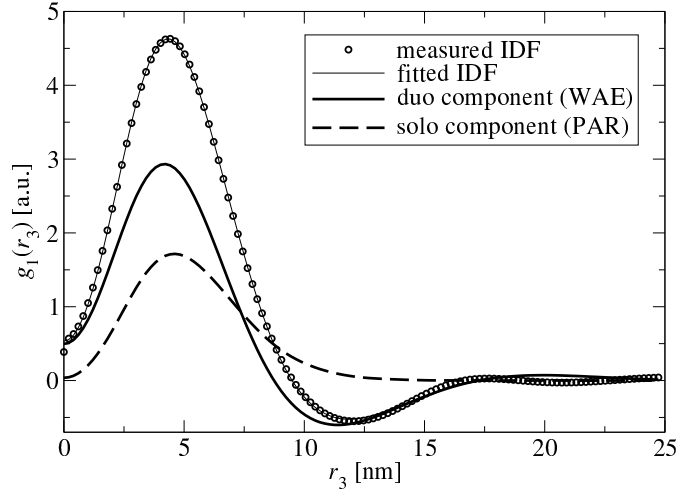


Figure 3.7.2: Decomposition of a measured interface distribution function (IDF) $g_1(r_3)$ into the two main morphological model components (solo, duo) for an aged TPU

Let us assume that the hard domains are the diluted phase, i.e. that the small-angle scattering counts all the chords which cross all the hard domains (in the matrix phase there may be chords which are so long that they will not be counted). Without loss of generality we consider a single hard domain. Figure ?? shows a sketch of this hard domain intersected by its chords. Obviously, the volume V_h of the hard domains is

$$V_h = d\sigma \iint l(r_1, r_2) dr_1 dr_2 = d\sigma \int r_3 H_h(r_3) dr_3, \quad (3.7.5)$$

and the change of the integration variables from the first to the second integral is possible, because $H_h(r_3)$ is just the function which gives the number of chords length r_3 . Moreover, the average hard-domain height is defined as usual

$$\bar{H}_h = \frac{\int r_3 H_h(r_3) dr_3}{\int H_h(r_3) dr_3} = \frac{V_h/d\sigma}{W}, \quad (3.7.6)$$

and it follows

$$\bar{H}_h W \propto V_h. \quad (3.7.7)$$

Both \bar{H}_h and W are fit parameters. Thus a quantity which is proportional to the total volume of hard domains can be determined from the fit. In the special case of rigid hard domains the proportionality even simplifies to $W \propto V_h$.

3.8 Code

SAXS patterns in Section 4.1 and Section 4.3 are processed by a package[228] which is written in the high-level programming language PV-WAVE. This package can be downloaded for free from website.[228] The license of commercial PV-WAVE is not a small

3 Experimental

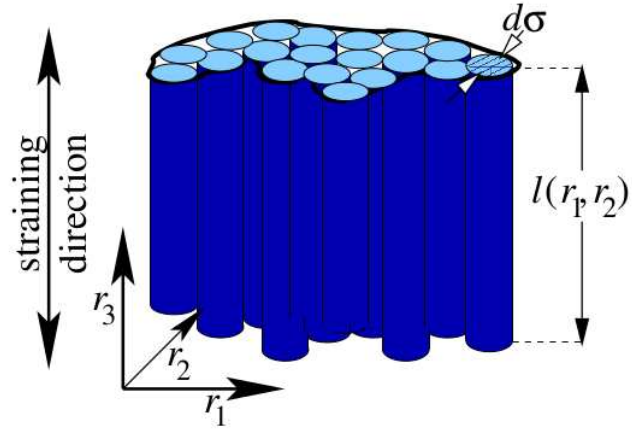


Figure 3.7.3: The (only) hard domain of a primitive morphology intersected by chords of varying length l , the lengths defined by the surface of the hard domain. Every chord occupies an infinitesimal cross section $d\sigma$. Only chords which run in straining direction are considered, because the longitudinal scattering $\{I\}_1(r_3)$ is analyzed.

expense if we share the codes in the scientific community. The developing of open-source codes is driven by the scientific community. Rewriting the package in open-source programming language Python, a completely free high-level programming language, is done by the author.[237] This python package (ipyChord) will be published and downloadable after a short time.

4 Results and Discussion

4.1 Morphology Variation of TPUs Monitored by SAXS Related to Strain-at-break

In this section¹, morphology evolution of 6 polyurethanes of different components under strain are monitored by in-situ SAXS. The relative volume fraction of hard domains are fit from the interface distribution function. An empirical equation of volume fraction of hard domains and macroscopic strain is established.

4.1.1 Properties of the TPU Materials

TPUs based on MDI, poly(alkylene adipate), and PTHF polyols and 1,4-BD are most common. Polyethers like PTHF are less compatible with MDI based hard chain segments than polyesters and TPUs derived from them show a higher degree of phase separation. The hard domains also tend to be larger and more complex than those found in TPUs based on polyesters. With regards to the short-chain diol, HQEE yields higher melting hard domains than those produced from 1,4-BD. In this paper, we investigate the MDI-based TPUs from PTHF, poly(alkylene adipate) and PCL polyols and 1,4-BD and HQEE chain extenders. With the present series of polyurethanes the TPU technology field is largely covered. The hard-segment content (HSC) has been kept constant for all TPUs and amount to 51 wt.-%. In regard to their mechanical properties (see Table 3.1), the TPUs based on PTHF (mqt and mbt) are significantly softer (5-10 shore-D units) than the polyester based TPUs, which may originate from a higher degree of phase separation. In this respect the use of HQEE or BD has only a minor effect on the polymer hardness (1-4 shore-D units). Although being soft, the highest tensile strength at break is measured for mbt. Another observation made is that the HQEE based TPUs show significantly lower values of both weight-average molecular mass M_w and tensile strength at break than those produced from BD. The HQEE based hard chain segments have a higher tendency to phase-separate than those from BD, causing the phase separation to start already at a lower conversion. This earlier phase separation is believed to be origin of the reduced M_w build-up, and consequentially poorer ultimate tensile properties. Early phase separation may affect the polymer morphology and the nature of the hard domains. The combined effects of differences in chain topology and polymer morphology may be reflected in the morphologies and their evolution under strain, notably for the polymer mqt.

¹This section is based on the paper published in *Macromolecular Chemistry and Physics* 2015, in print.

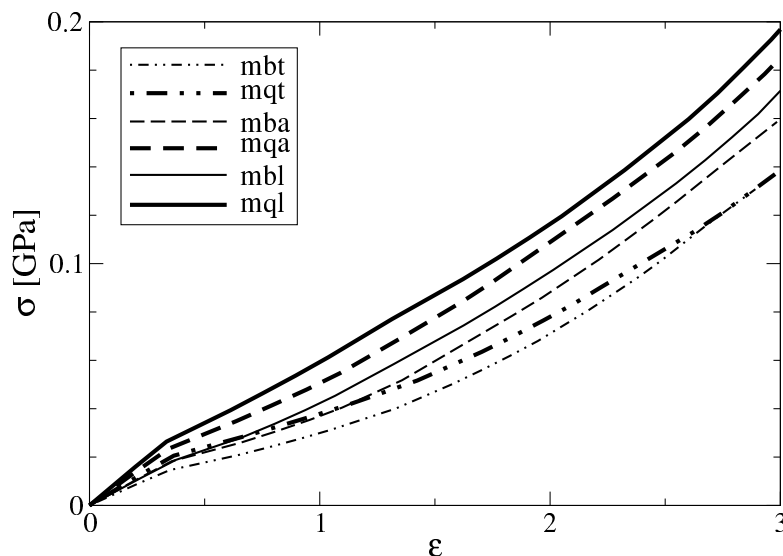


Figure 4.1.1: Hand-cast thermoplastic polyurethane materials. True stress σ vs. local strain ε at the position of X-irradiation as measured in-situ during the tensile tests

4.1.2 Tensile Tests

Figure 4.1.1 shows the stress-strain curves (true stress vs. local strain) measured in the experiments at the synchrotron. Bear in mind that the tensile strength σ_{max} from Table 3.1 is expressed in engineering stress, $\sigma_{eng} \approx \sigma / (1 + \varepsilon)$. The local strain ε is computed from the movement of two fiducial marks close to the point of X-irradiation. This is not the engineering strain which is computed from the movement of the machine crossheads. Materials become stronger, when the chain extender BD (thin lines) is replaced by HQEE (bold lines). Strengthening correlates with the detectability of crystallites.

Related to the soft-segment component the weakest material (dashed-dotted) contains PTHF, the medium one (dashed) is based on adipic ester, and the strongest one (solid line) has soft segments from PCL. This shows that the tensile strength could originate from differences in phase separation and intramolecular interactions between the polyol segments. A comparison with the WAXS curves further indicates a correlation with crystallinity of the hard domains: in the hardest material the crystallites are big enough to clearly detected.

4.1.3 TEM

Figure 4.1.2 presents the morphology of the sample mbt. The morphologies contain the uncorrelated and correlated hard domains. Black region stained by RuO_4 is soft matrix and white region is hard domain. Most of hard domains are randomly placed in the soft matrix, meanwhile, some hard domains are correlated with their nearest neighboring

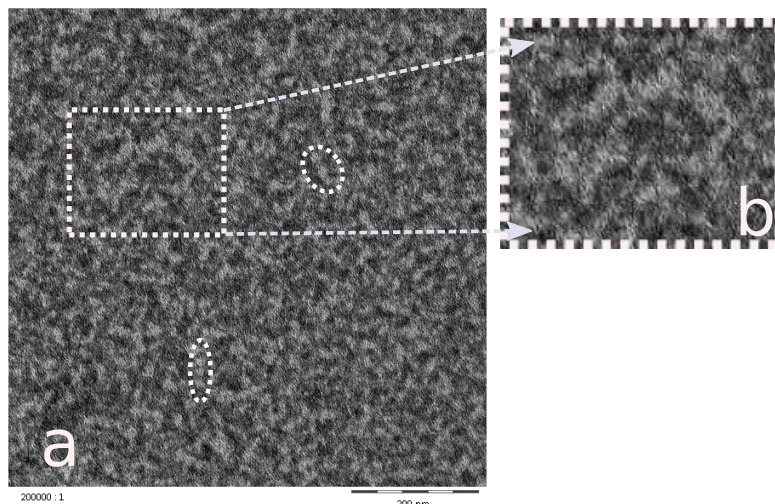


Figure 4.1.2: TEM image (a) exhibiting correlated and uncorrelated hard domains in undrawn PUE. Subfigure (b) magnified from the dashed rectangle of image (a) exhibits the uncorrelated and correlated hard domains clearly. Dashed ellipse circles exhibit the stacking of hard domains.

hard domains and even the correlation reaches into the third neighboring hard domains. All the other materials have the similar morphology.

4.1.4 Wide-angle X-ray Scattering Scans

Figure 4.1.3 presents the WAXS scans of the studied materials. For mbt and mba only an amorphous halo is observed. All materials with the chain extender HQEE exhibit broad crystalline reflections, and mbl is in between. This shows that the HQEE-based hard domains are more perfectly ordered than those from BD.

WAXS results monitor correlations on the scale of several angstrom. The strongest scattering effect is related to the contrast between chains and vacuum. Thus some information on the orientation distribution of the normal-direction to the chains may be obtained as a function of strain. Beyond that, even short-range correlations between different chemical groups along the chain may be detectable. On the other hand, the SAXS monitors the two-phase morphology on the scale of nanometers, e.g. the sizes of hard and soft domains and their arrangements in space. For distorted materials of low crystallinity like polyurethanes the morphological relations between both views appear weak, as a previous study has shown and a WAXS study may be reported separately from a SAXS study.

In a tensile test it is expected that the WAXS amorphous halo becomes oriented. It demonstrates the orientation of the normal to the chain direction. For the semicrystalline materials crystalline reflections may orient, grow, or decrease during straining.

From the shape of oriented peaks some information of the orientation distribution of

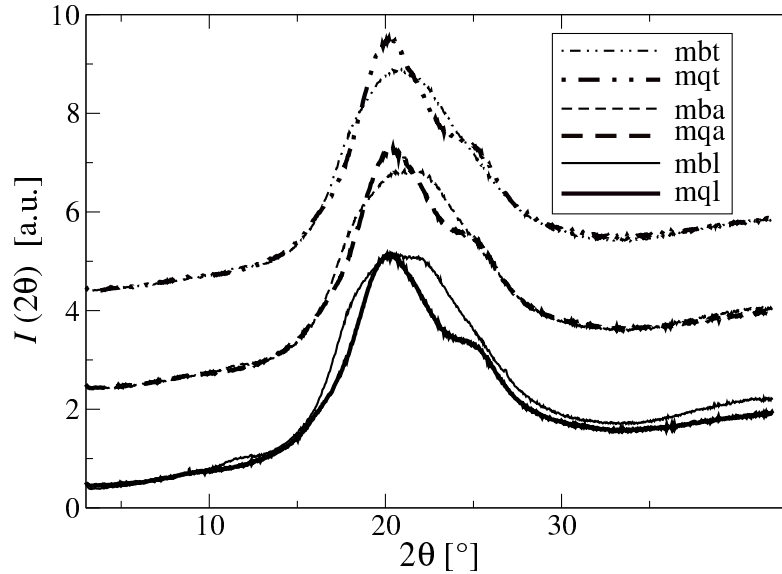


Figure 4.1.3: Thermoplastic polyurethane materials hand-cast from different raw components. WAXS scans $I(2\theta)$ (wavelength $\lambda = 0.1542$ nm) of the virgin isotropic materials. Some curves are shifted in vertical direction for clarity

the crystals may be obtained. Similar to the analysis of the orientation of the amorphous halo one does not obtain absolute values, because there is no easy way to determine the background that must be considered. Nevertheless, limits and trends for an uniaxial orientation parameter can be determined. Similarly, the variation of the integral intensity of separated crystalline reflections as a function of strain yields indications of strain-induced crystallization or melting. Of course, the integration has to be carried out in 3D reciprocal space and not only in the detector plane.

4.1.5 SAXS Data Accumulated during the Tests

Figure 4.1.4 presents recorded scattering patterns $I(s_{12}, s_3)$ and CDFs $z(r_{12}, r_3)$ computed from them. In fact, only central cutouts are displayed and only the long-period face $-z(r_{12}, r_3) > 0$ of the CDFs is shown. CDFs visualize the local structure in the neighborhood of a domain: Each peak shows, in which direction and distance neighbor domains are found. It appears worth to mention that scattering cannot detect the presence of a co-continuous morphology. This is a consequence of the mathematical relation (notably: an autocorrelation) between structure and scattering pattern. Thus in the SAXS data, domains that bend away from the normal plane to the straining direction appears as if they were cut-off in the direction transverse to the straining (cf. the discussion of the breadth of the long-period peaks below).

For each tensile test a row of images is presented. The leftmost row shows the weakest material, the strongest one is found on the right. In each row the strain ε increases from top to bottom. Compared to respective machine-cast materials[58] the SAXS patterns

4.1 Morphology Variation of TPUs Monitored by SAXS Related to Strain-at-break

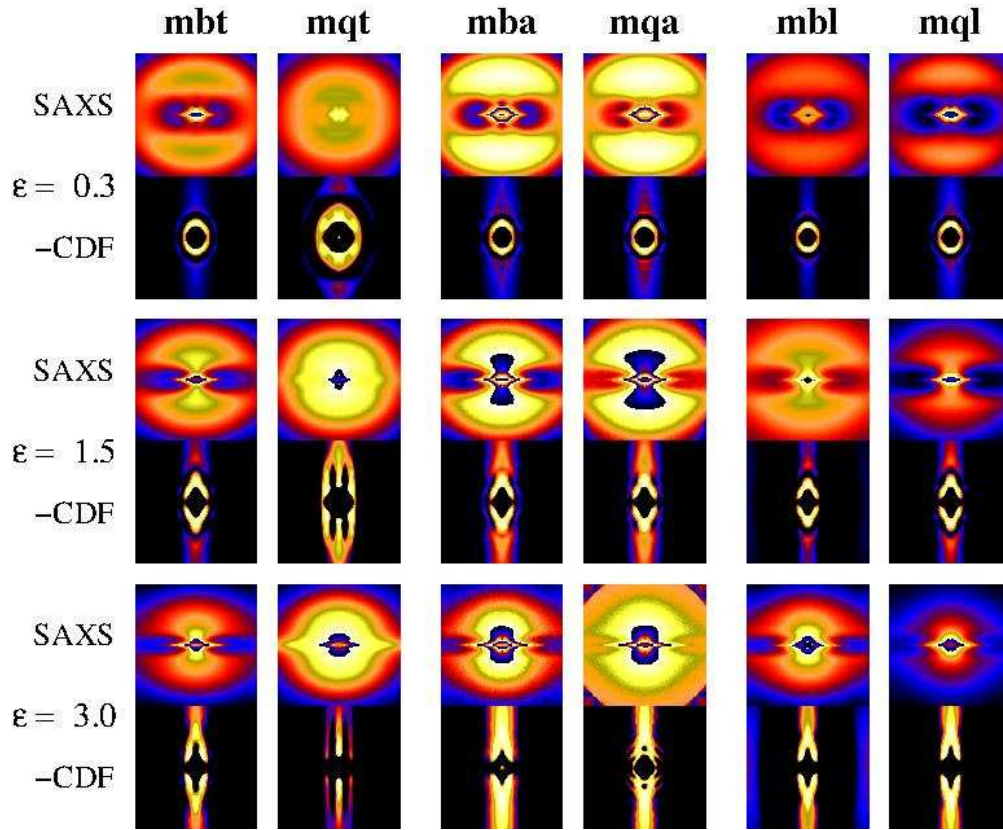


Figure 4.1.4: Selected SAXS data from continuous straining experiments of 6 hand-cast TPU materials. ε is the strain. Straining direction is vertical (s_3, r_3 resp.). The top pattern in each line is the scattering intensity (“SAXS”), shown as $\log(\log(I(s_{12}, s_3)))$, $-0.15 \text{ nm}^{-1} \leq s_{12}, s_3 \leq 0.15 \text{ nm}^{-1}$. The bottom pattern in each line presents the long-period peaks in the chord distribution function (“-CDF”), $-z(r_{12}, r_3)$, $-50 \text{ nm} \leq r_{12}, r_3 \leq 50 \text{ nm}$ on a logarithmic pseudo-color intensity scale

look similar, but the CDFs are fundamentally different. With the hand-cast materials the long-period peaks are broad (in vertical direction). They are neither narrow nor found in static discrete bands like with the machine-prepared TPUs. Instead, the CDFs look very similar to those from a previous study of some of us[61]. Also those samples were prepared by the hand-casting process.

4.1.6 Nanostructure from CDF Analysis

The 6 materials exhibit morphological differences. Compared to the given overview they are more clearly presented in meridional cuts of the CDFs (Figure 4.1.5). In one of the subfigures straight lines are drawn as guides to the eye. They connect the first-order peaks (solid) and the second-order peaks (dashed). In each strip the brightest yellow spot on the central line indicates the most-frequent long period. mqt shows a peculiarity that has previously been found with machine-cast materials[58]. The most-frequent long period relaxes after an initial increase. The yellow spot moves down and a long tail points upward. The peculiar tail formation is observed with all materials. It has earlier been observed with other hand-cast polyurethanes[61]. Both long-period relaxation and the formation of a long tail have been explained by a “sacrifice-and-relief” mechanism[61] that requires the destruction of a considerable amount of hard domains.

The CDFs of mqt resemble an intermediate state between the morphology of machine-cast TPUs and those of the other hand-cast materials. Perhaps here the homogeneity of the raw component mixture has been higher by chance.

To capture the nanostructure change quantitatively by means of the long period peak, we track its position and shape during the tensile tests. In previous work on polyurethanes we have done that as well[61, 58, 238]. Figure 4.1.6 presents the evolution of the nanoscopic strain $\varepsilon_n(\varepsilon)$ computed from the most-frequent long period. Only the material mqt exhibits the relaxation behavior known from machine-cast materials[58] that has already been discussed qualitatively. With the other hand-cast materials the known[58] slow increase of the nanoscopic strain $\varepsilon_n(\varepsilon) \approx 0.6\varepsilon$ continues up to the end of the experiment. We explain the low ε_n by the rigidity of the hard domain (average height: \bar{H}_h) that is part of the long period $\bar{L} = \bar{H}_h + \bar{H}_s$.

The breadth of the long-period peak yields a measure of some average hard-domain extension transverse to the straining direction. Sufficient anisotropy of the CDF is required for its determination. Figure 4.1.7 displays the results. The hard domain extensions decrease with increasing strain. This indicates disruption. Most of the materials show a very similar behavior with an almost constant value reached for $\varepsilon > 1.5$. Again, an exception is the material mqt that has the relaxing long periods. A possible explanation is, that narrow hard domains have less tie molecules and the related narrow sandwich structure (two hard domains with a soft gap in between) is relaxing more frequently than wider ones.

4.1 Morphology Variation of TPUs Monitored by SAXS Related to Strain-at-break

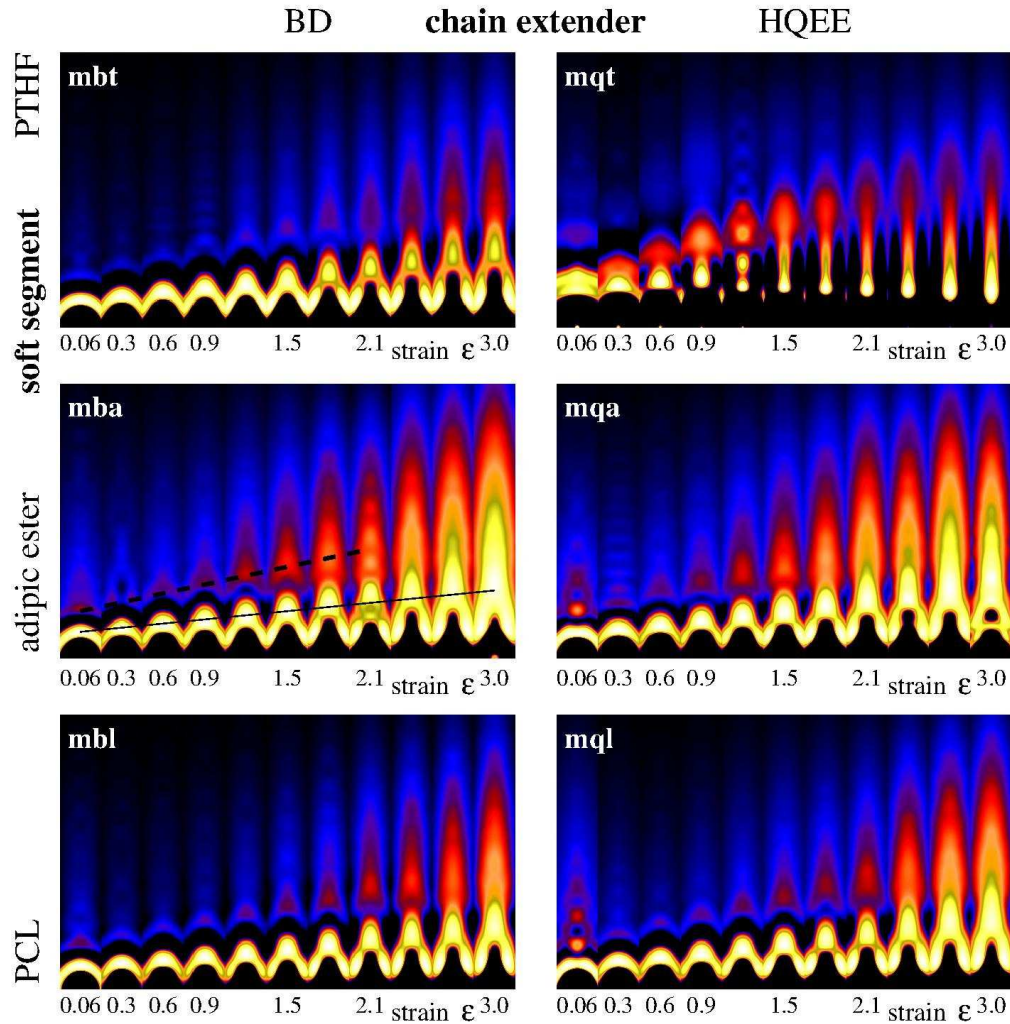


Figure 4.1.5: Meridional long-period regions cut from the CDFs. $-z(r_{12}, r_3)$ $0 \leq r_3 \leq 50$ nm, $|r_{12}| \leq 8$ nm is presented on a varying $\log(\log(-z))$ intensity scale. In subfigure mba: Lines indicate first-order (solid) and second-order (broken) long period peaks.

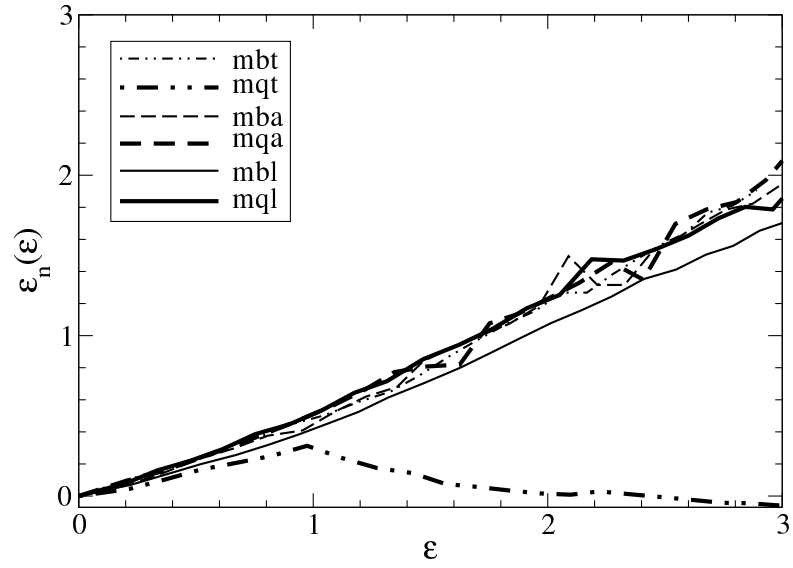


Figure 4.1.6: Nanoscopic strain $\varepsilon_n(\varepsilon) = r_{3,Lmax}(\varepsilon)/\varepsilon$ computed from the position $r_{3,Lmax}(\varepsilon)$ of the first-order long period maximum in the the CDF as a function of the macroscopic local strain ε

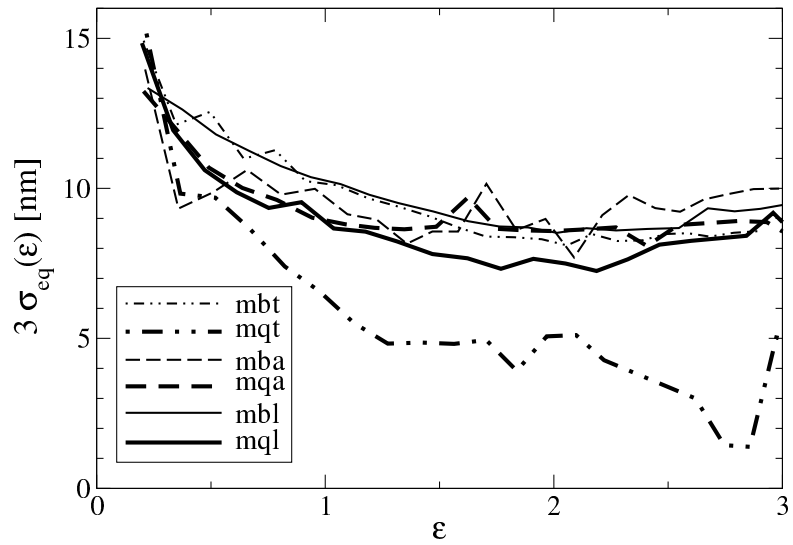


Figure 4.1.7: $\sigma_{eq}(\varepsilon)$ computed for the evolution of the first-order long period peak is a measure of the lateral size of the hard domains

4.1.7 Bonart's Longitudinal Scattering

Direct Analysis. The longitudinal scattering $\{I\}_1(s_3)$ exhibits morphological differences, as well. Figure 4.1.8 displays the results. In the upper subfigures the soft segment is PTHF. Here substitution of the chain extender BD by HQEE has several effects. The intensity is doubled, the peak position is affected, and its response to strain is changed. With mqt containing HQEE the long-period peak is much less pronounced than with the material mbt.

Such strong effects are not found with the middle and the bottom subfigures, but minor differences with respect to both the varying long-period and changing intensity can still be read from the curves. In Figure 4.1.8 the area under the curves is the scattering power Q . Its differences for the different materials and the responses to the applied strain are reported in Figure 4.1.9. Obviously, the chain extender BD yields lower Q than HQEE. The relative variations of Q as a function of ε are similar for all materials. If the initial volume fraction of hard domains $v_h(\varepsilon = 0) < 0.5$, a decrease of Q is approximately proportional to a reduction of v_h . For all materials an initial increase is followed by a decrease. Because of the blurred morphology of the hand-cast materials a quantitative determination of the changing v_h is possible by an analysis of the corresponding interface distribution functions.

IDF Analysis. From Bonart's longitudinal scattering $\{I\}_1(s_3)$ the IDF $g_1(r_3)$ can always be computed. It describes the statistics and arrangement of domain heights in straining direction r_3 . Nevertheless, an analysis that may yield deeper insight is only possible, if a suitable model can be fitted to the IDF. In the case of machine-processed materials[58] a peculiar band structure has been found that requests for an involved morphological model based on quasi-periodicity. Here the inspection of Figure 4.1.4 indicates that an IDF analysis appears much more promising.

In a first step the IDFs are computed and visually inspected. Their features and the trend as a function of ε is similar for all materials show in Figure 4.1.10. Figure 4.1.11 shows IDFs of the material mql at different strains. The decrease of the integral indicates a loss of hard-domains in the tensile test. The long-period peak $L(r_3)$ moves to higher r_3 with increasing strain. The shape of the curves indicates that they can be fitted by Gaussian distributions. The blurred morphology of the hand-cast material is reflected in broad peaks that have already died out for $r_3 > 25$ nm. A short-range model appears to be applicable. The strong positive domain peak dominates the IDF. Even if second-order features are not correctly considered by a simple model, it should be able to separate the hard-domain peak $H_h(r_3)$ from the soft-domain peak $H_s(r_3)$. A failure of the separation can be assessed by discussing the plausibility of the extracted morphological parameters as a function of ε .

Thin lines in Figure 4.1.11 show the best fits with the one-dimensional stacking model[222, 195]. The strong peak appears to be fitted well, but the long-period peak $L(r_3)$ is poorly fitted for low and medium strain. This shortcoming may be related to remnant features of quasi-periodic sequences of hard and soft segments that have been found with machine-cast TPUs[58]. The following figures present the values of the parameters of

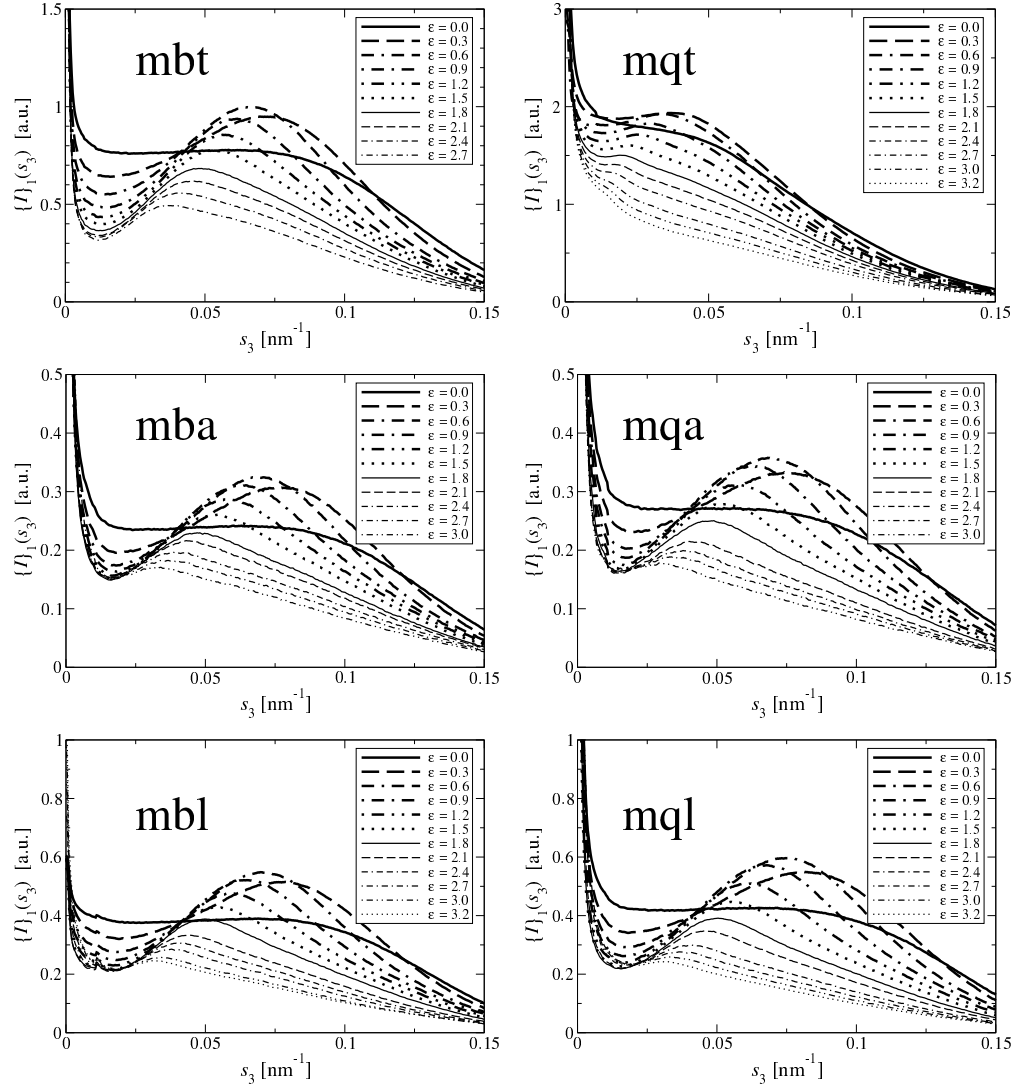


Figure 4.1.8: Evolution of Bonart's longitudinal scattering as a function of strain. Intensities are normalized for constant X-ray flux and constant irradiated volume

4.1 Morphology Variation of TPUs Monitored by SAXS Related to Strain-at-break

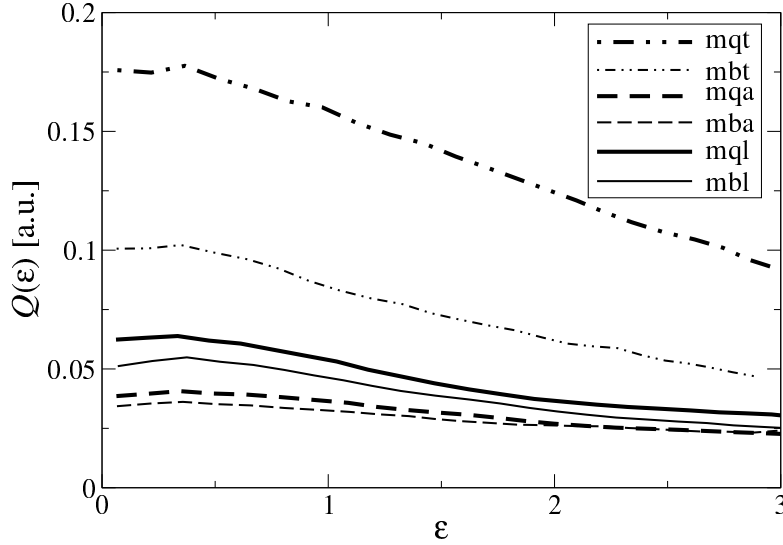


Figure 4.1.9: Variation of the scattering power Q in the tensile tests

$H_h(r_3)$ and $H_s(r_3)$ determined by nonlinear regression[217] of $g_1(r_3)$.

Figure 4.1.12 displays the variation of the average hard-domain height $\bar{H}_h(\varepsilon)$ for all materials. $\bar{H}_h(\varepsilon)$ varies only slightly with ε and has a value of about 8 nm. 8 nm is also the height of hard domains that has been extracted from the data of machine-cast materials[58, 234] that are, as well, based on MDI hard segments. It has been identified from a peculiar quasi-periodic signature of their CDF peaks and related to the sequence of 2 MDI segments along the chain of the copolymer. This is in excellent agreement with crystallographic data[50, 239, 83] from model urethanes made from alternating MDI and BD. The papers find unit cell heights of 3.8 nm. Thus a hard block that contains 2 MDI segments should have a height of $2 \times 3.8 \text{ nm} = 7.6 \text{ nm}$.

Also the relative breadths σ_h/\bar{H}_h of $H_h(\varepsilon)$ vary only slightly between 0.4 and 0.6. Thus, the hard domain ensemble has an almost constant average height and distribution width. Inelastic behavior is what one expects.

Nevertheless, there are slight changes related to growth and destruction of hard domains. Thickness growth at low strain is only observed for mbt. The other materials exhibit constant thickness followed by increasing average thickness for $0.5 < \varepsilon < 1.5$. We will show that this is already the region in which hard domains are destroyed. So the finding shows that for most of the materials thin hard domains fail more easily than thick ones.

Figure 4.1.13 presents $\bar{H}_s(\varepsilon)$, the variation of the average soft-domain height between two hard-domains. To keep the effort manageable only some of the measured data have been processed. The strong and monotonous increase of $\bar{H}_s(\varepsilon)$ describes the expected contribution of the soft phase to the nanoscopic elongation of the materials. Only for the material mqt $\bar{H}_s(\varepsilon)$ iterates towards zero, because there the distributions $H_s(r_3)$ are extremely wide. It is worth to mention that the regression does not return the most

4 Results and Discussion

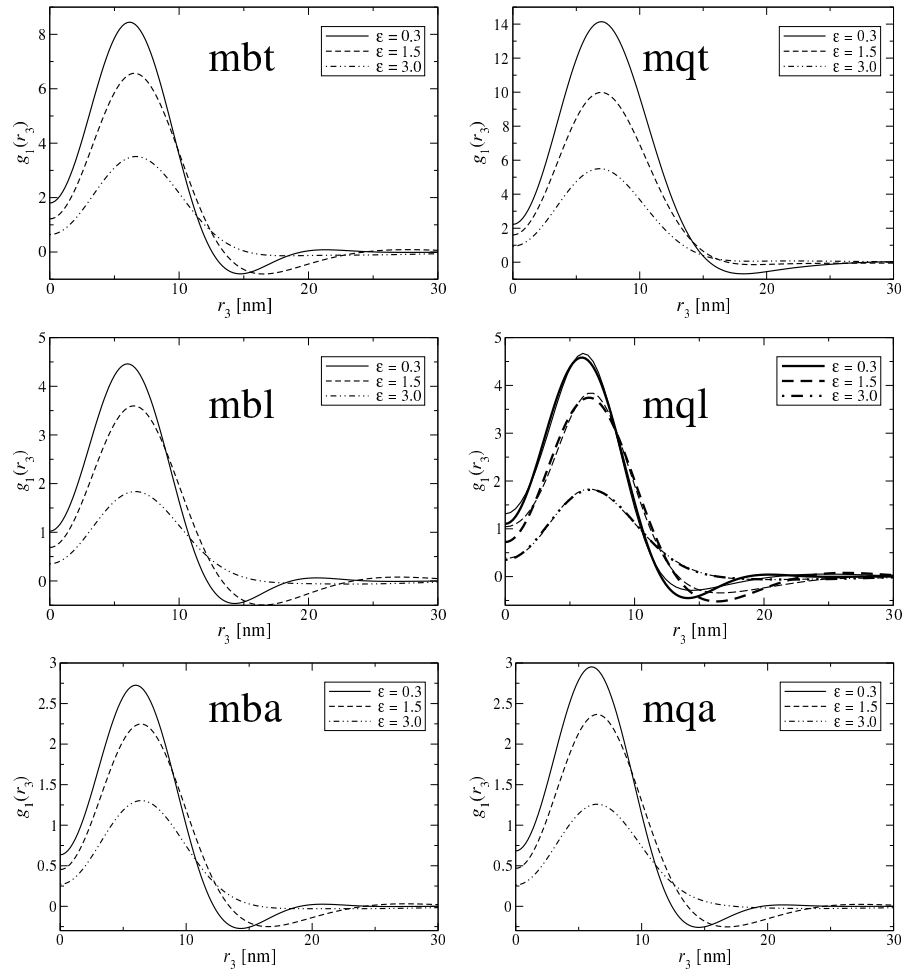


Figure 4.1.10: Interface distribution functions (IDFs) computed from the longitudinal projection of 2D SAXS pattern.

4.1 Morphology Variation of TPUs Monitored by SAXS Related to Strain-at-break

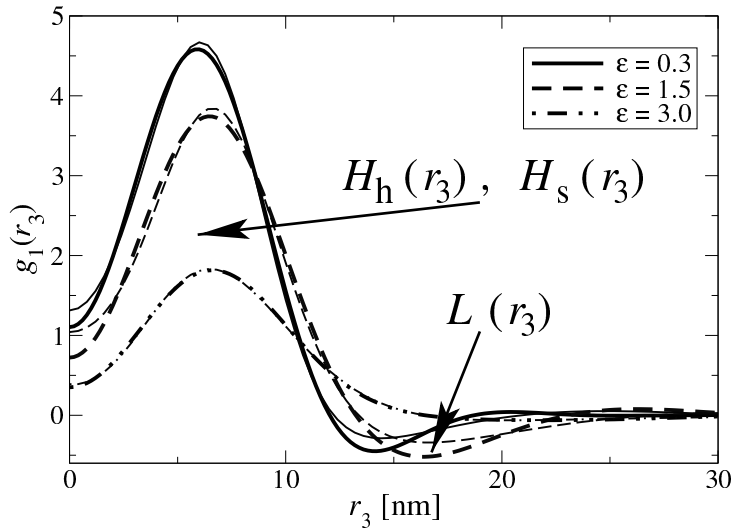


Figure 4.1.11: Material mql. Interface distribution functions (IDF) $g_1(r_3)$ computed from $\{I\}_1(s_3)$ for selected ϵ . The data of the other materials look similar. Bold lines: measured data. Thin lines: fits by the stacking model. The main peak is made from $H_h(r_3)$ and $H_s(r_3)$, the height distributions of hard and soft domains in straining direction r_3 . Long period distributions $L(r_3)$ are peaking in negative direction

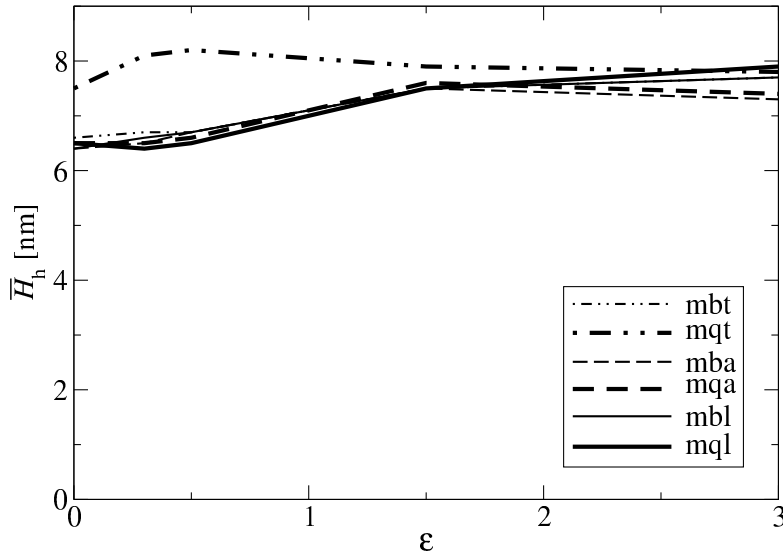


Figure 4.1.12: Variation of the average hard domain height, $\bar{H}_h(\epsilon)$ as determined from fits of $g_1(r_3)$

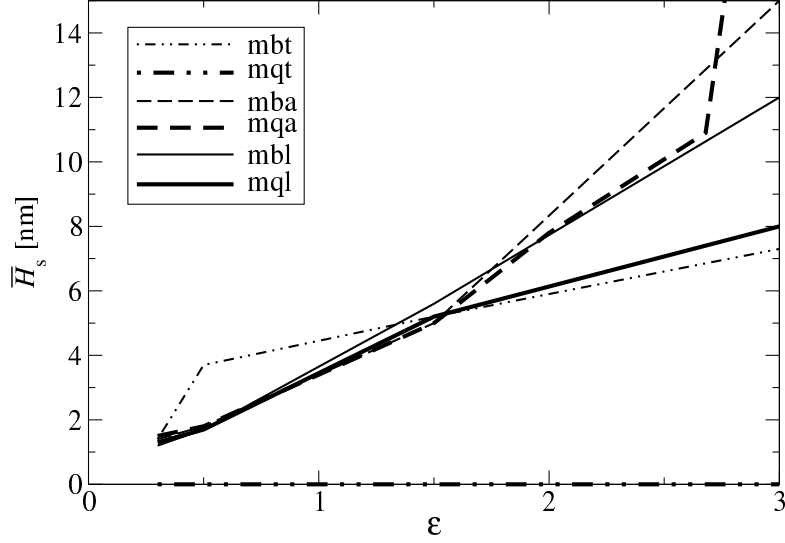


Figure 4.1.13: Average soft domain height, $\bar{H}_s(\epsilon)$ of the studied materials as determined from fits of $g_1(r_3)$

probable soft-domain height, but the number average of the respective chords.

Figure 4.1.14 presents the changes in relative widths of the soft-domain height distributions $H_s(r_3)$. Again, mqt drops out. The infinite values have been arbitrarily set at the upper edge of the drawing. With the other materials, the relative width strongly decreases with increasing strain. σ_s/\bar{H}_s would stay constant, if the structure would be stretched affinely without a destruction of hard domains. The observed decrease means that entities with narrow soft gap either vanish or catch up, and the latter appears unreasonable. Simultaneously, entities that contain a wide soft gap may be strained less than those with a gap of average height. Remarkably, the initial homogenization of the distribution is stronger for mbt than for the other materials. Initial domain thickness growth appears to homogenize the thicknesses. For $\epsilon > 1.5$ all materials behave similar – except for the unfitable mqt.

Figure 4.1.11 shows that the integral of the IDF is decreasing with increasing strain. Assuming a constant contrast between soft and hard phase, the quantity

$$\frac{W(\epsilon)}{W(0)} = \frac{n_{chords}(r_3, \epsilon)}{V(\epsilon)} \frac{V(0)}{n_{chords}(r_3, 0)} \approx \frac{v_h(\epsilon)}{v_h(0)} = v_{r,h}(\epsilon) \quad (4.1.1)$$

describes the relative variation of the number of chords $n_{chords}(r_3, \epsilon)$ in straining direction r_3 normalized to the volume of the material. Moreover, if the volume of the material does not change during straining ($V(\epsilon) \approx V(0)$), the approximation is valid and Eq. (4.1.1) describes the ratio of the volume fraction $v_h(\epsilon)$ of hard domains with respect to the initial volume fraction $v_h(\epsilon = 0)$. Thus, an increasing $W(\epsilon)$ indicates formation of hard phase (strain induced phase separation) and a decreasing $W(\epsilon)$ indicates destruction of hard domains. Figure 4.1.15 shows the result of the weight analysis. For all materials

4.1 Morphology Variation of TPUs Monitored by SAXS Related to Strain-at-break

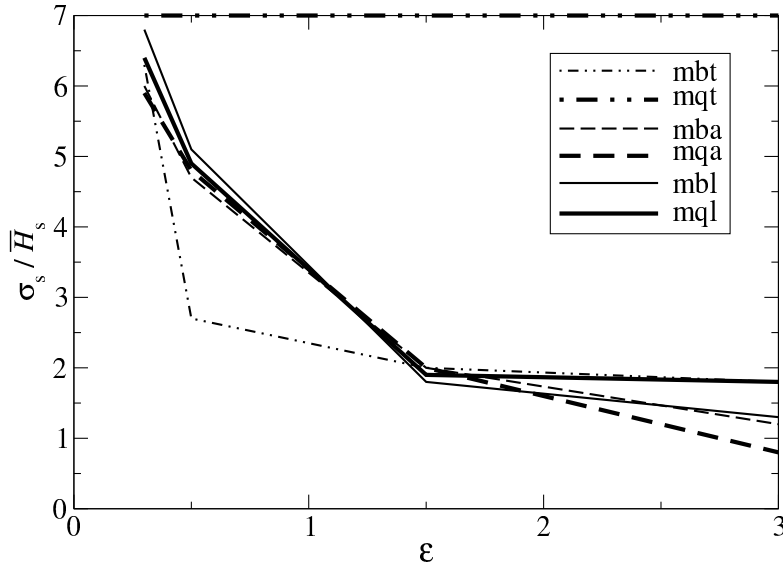


Figure 4.1.14: Relative width $\sigma_s(\epsilon) / \bar{H}_s(\epsilon)$ of the soft domain distribution as determined from fits of $g_1(r_3)$

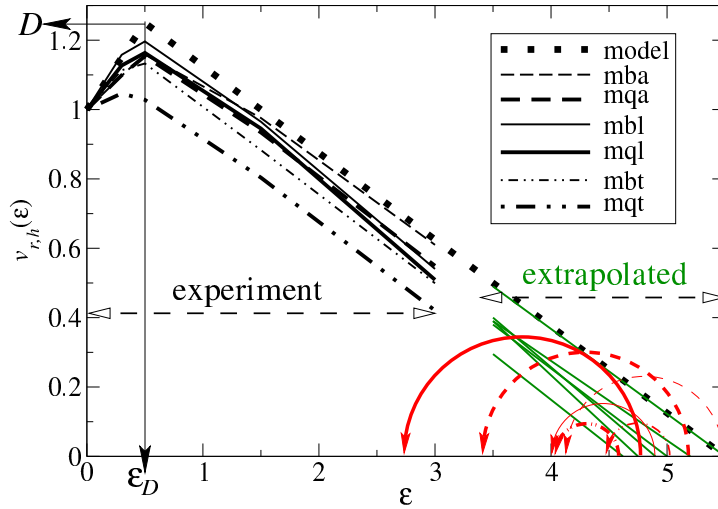


Figure 4.1.15: Variation of the relative volume fraction of hard domains, $v_{r,h}(\epsilon)$ for $0 \leq \epsilon \leq 3$ as determined from the weights $W(\epsilon)$ in fits of $g_1(r_3)$. Characteristic parameters D and ϵ_D are indicated with the model curve (dotted). Linear extrapolations hit the ϵ -axis at a theoretical strain at break $\epsilon_{b,th}$. Circular arrows point at ϵ_b values from Table 3.1. Discrepancies are high for materials with HQEE that do not contain PTHF

4 Results and Discussion

a strain-induced formation of hard domains is observed up to $\varepsilon \approx 0.5$. The gain is different for different materials. It is lowest for mqt and highest for mbl. For $\varepsilon > 0.5$ all materials show a linear decrease of the hard-phase volume over the whole range of the tensile test. In several previous studies we have found by different analysis methods that hard domains must be sacrificed. Now, for the studied materials, we are able to present a quantitative relation.

As sketched in Figure 4.1.15 we define two material constants. D is a tensile domain growth factor (in analogy to the definition of the tensile strength in a stress-strain curve), and ε_D is the corresponding growth-limit strain, i.e. $D = v_{r,h}(\varepsilon_D)$. The slope of the subsequent destruction decay, $c_{r,\varepsilon} = dv_{r,h}/d\varepsilon = 0.25$ is identical for all the different materials. It defines a tensile hard-domain consumption. A reason for the identical value may be that all materials share the same HSC. Considering the variety of chemical compositions the result shows that the demand for domain destruction per strain-step appears to be a principle that governs the straining of TPU. This should be different for chemically crosslinked materials.

In summary, for the studied materials a first-approximation model for the relative volume change of hard domains is described by

$$v_{r,h}(\varepsilon) \approx \begin{cases} 1 + (D - 1)\varepsilon/\varepsilon_D & \text{for } \varepsilon \leq \varepsilon_D \\ D - c_{r,\varepsilon}(\varepsilon - \varepsilon_D) & \text{for } \varepsilon > \varepsilon_D \end{cases}. \quad (4.1.2)$$

Does the material break, if almost all hard domains are consumed? This would mean $v_{r,h}(\varepsilon_b) = 0$, and if the linear relation of Eq. (4.1.2) holds up to the materials failure, then the approximation

$$\varepsilon_b \approx D/c_{r,\varepsilon} + \varepsilon_D \quad (4.1.3)$$

should be valid. Comparison with Table 3.1 and the extrapolations sketched in Figure 4.1.15 indicates that Eq. (4.1.3) is not too bad. The found discrepancies may be related to ripening of the materials between preparation and the synchrotron study. This is indicated by the fact that for some materials ε_b measured after production is smaller than the ε_{max} that has been reached at the synchrotron without failure.

Destruction Verified by Infrared (IR). If the hard domain of PU is destructed during material deformation, absorbance of chemical groups in the hydrogen bonding may decrease. The hydrogen bonding is composed of chemical group N-H and C=O.[240] But not all the N-H and C=O groups are in the hydrogen bonding. Figure 4.1.16 shows the IR absorbance decrease of hydrogen bonded N-H and C=O groups with increasing the strain. The absorbance decrease of hydrogen bonded indicates the decrease of hydrogen bonding density. The decrease of hydrogen bonding density indicates the destruction of hard domains, some hard segments are pulled out from the hard domains into soft matrix.[107] As the precision of our equipment is limited, only a qualitative analysis is possible.

4.1 Morphology Variation of TPUs Monitored by SAXS Related to Strain-at-break

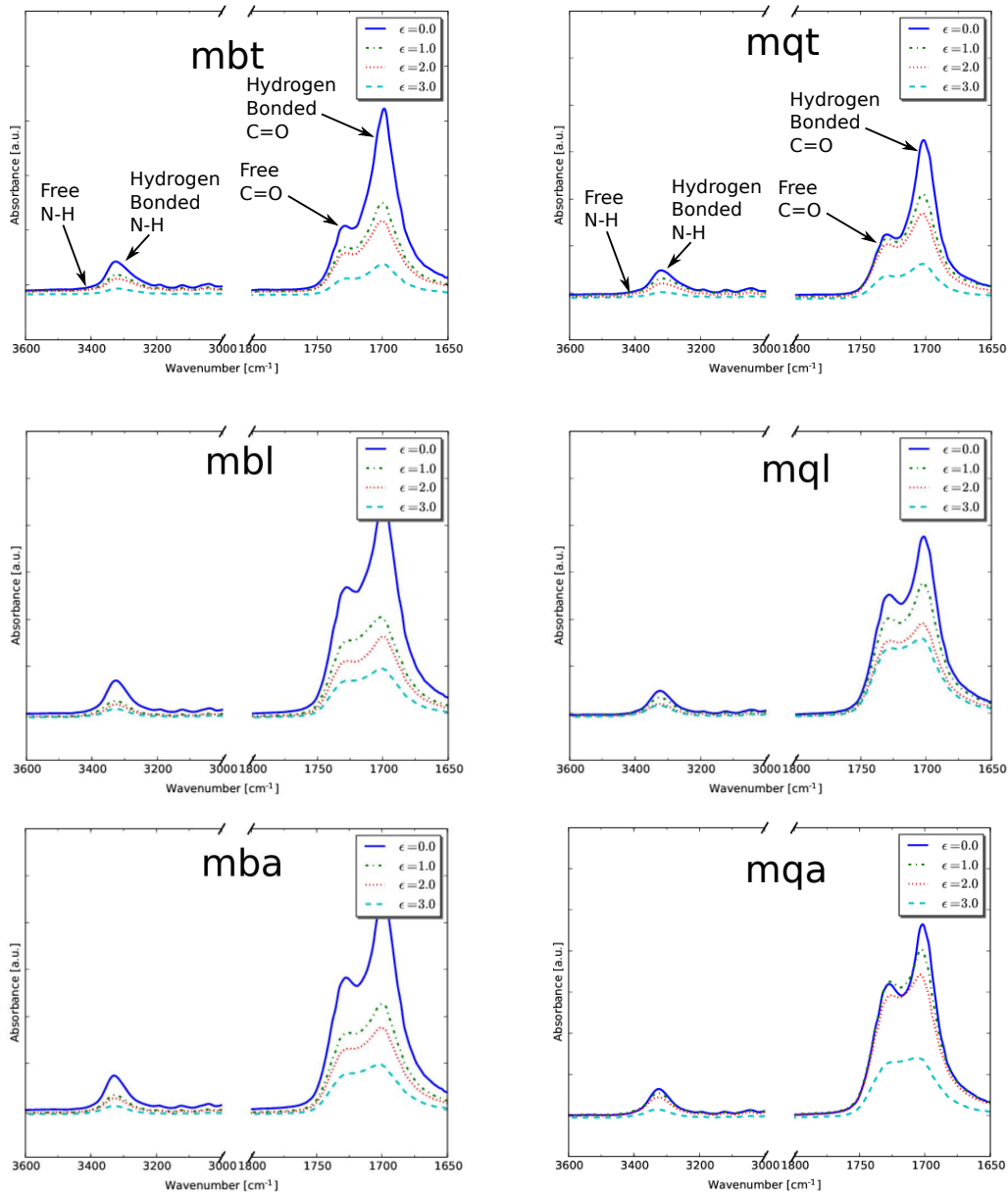


Figure 4.1.16: Infrared absorbance spectroscopy of chemical groups N-H and C=O as a function of strain ϵ .

4.1.8 Conclusion

The hand-cast TPU materials exhibit hard domains with particularly wide distributions of their sizes and the distances between them. Therefore, one can describe the topology of their domains with a simple two-phase model quantitatively and monitor their evolution in the test strain. Apparently, the investigated materials even meet some special requirements. These allow us to track the change of the hard-phase volume in the tensile test. The relationship of the found result with the elongation at break indicates how fundamental the destruction of physical crosslinks (the hard domains) appears to be in the non-crosslinked polyurethane with respect to both the extensibility and to the ultimate elongation of the material.

As an explanation for the wide distributions of hand-molded materials, we have adopted a double-sequence variability of the hard and soft blocks along the chains. The second variability is thus generated by incomplete mixing in the bucket. Let us think one step ahead. Then it appears possible to us that even the phase separation proceeds in two steps when the material is cooled from the melt. Differences with respect to machine-processed material would become apparent in a calorimetric study. Based on this notion it is even imaginable that hand-cast samples show lower hardness than machine-processed materials. By comparing to the hardness of a reference product one could eventually conclude on the quality of mixing.

In consumer products made from TPU's a double-variability will probably play a minor role because during the processing of bulk material it usually passes through several temperature cycles (drying, annealing, extruding, annealing, injection molding, annealing). In some of these steps chain scissoring occurs, which is healed by a downstream annealing step[1, 147, 155, 113, 225, 226, 224]. The associated rearrangement of chain pieces is likely to homogenize the ensemble of chains, and finally each chain carries the same statistical fingerprints of polyaddition and mixing inhomogeneity.

We have studied materials with a hard segment content $\text{HSC}=0.51$ only. Therefore we do not know, if the tensile domain consumption $c_{r,\varepsilon}$ is a function of HSC. A systematic variation of HSC is required. It should give information about whether one should normalize the initial value of the curves in Figure 4.1.15 instead of on 1 on HSC. The latter would be reasonable, if an absolute hard-domain consumption, $c_h = \text{HSC } c_{r,h}$, would turn out to be a characteristic parameter of the material. Finally, we hope that Eq. (4.1.2) and Eq. (4.1.3) may become useful in the modeling of material properties of thermoplastic polyurethanes.

For future investigation, it appears reasonable drive such experiments to the vicinity of the elongation at break. This requires some technical improvements concerning the synchrotron beamline (X-ray beam of higher intensity but still large diameter, very advanced detector) and the tensile tester (use of self-tightening grips).

4.2 Ageing Effect on Morphological Evolution of PUE under Strain

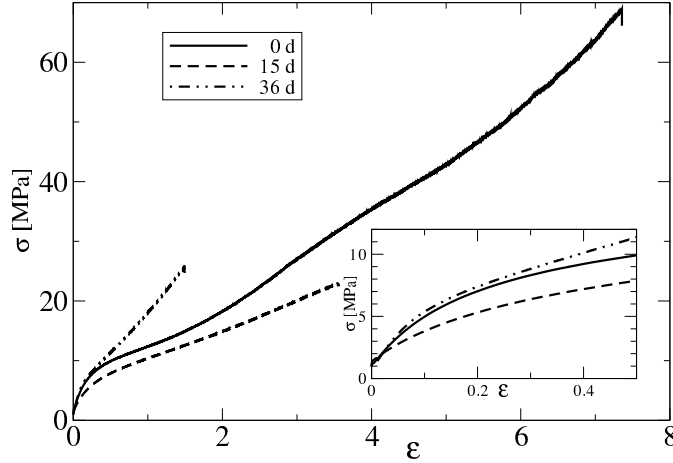


Figure 4.2.1: Mechanical performance of unaged and aged TPU materials. σ is the engineering stress, and ϵ the engineering strain. The inset is an enlarged image of the beginning of the curves

4.2 Ageing Effect on Morphological Evolution of PUE under Strain

In the current section, the samples aged after different time at 150°C are subjected to stretching monitored by in-situ SAXS. Ageing effect on the nanoscale of morphology during ageing and ageing effect on the nanostructure evolution under strain are discussed.

4.2.1 Mechanical Performance

Figure 4.2.1 presents the mechanical performance of the unaged and the aged TPU materials. For the unaged material (0 d) the strain at break is $\epsilon_b = 7.4$. After 15 days of aging (15 d) the material has become softer than the unaged material. It fails at $\epsilon_b = 3.6$. This is already outside the range of the SAXS monitoring. The softening of the material can be explained if we can allot 15 d to the mentioned first stage of degradation[145, 146], in which only the hard domains are weakened (cf. result in Figure 4.2.7) from aging.

Sample 36 d, on the other hand, shows the highest modulus of the 3 specimens. It breaks at $\epsilon_b = 1.5$. This very early break indicates that 36 d is probably from the second[146, 145] stage of degradation, and the high modulus and increased rigidity[129] may indicate that after 36 d in the soft phase the cross-linking mechanism is still more frequent than chain scission[134, 241].

4.2.2 Screening the SAXS Data from the Straining Experiments

Characteristics of the Unstrained Samples. Figure 4.2.2 presents recorded scattering patterns $I(s_{12}, s_3)$ and CDFs $z(r_{12}, r_3)$ computed thereof. In fact, only the long-period face $-z(r_{12}, r_3) > 0$ of the CDFs is shown. CDFs visualize the local structure in the

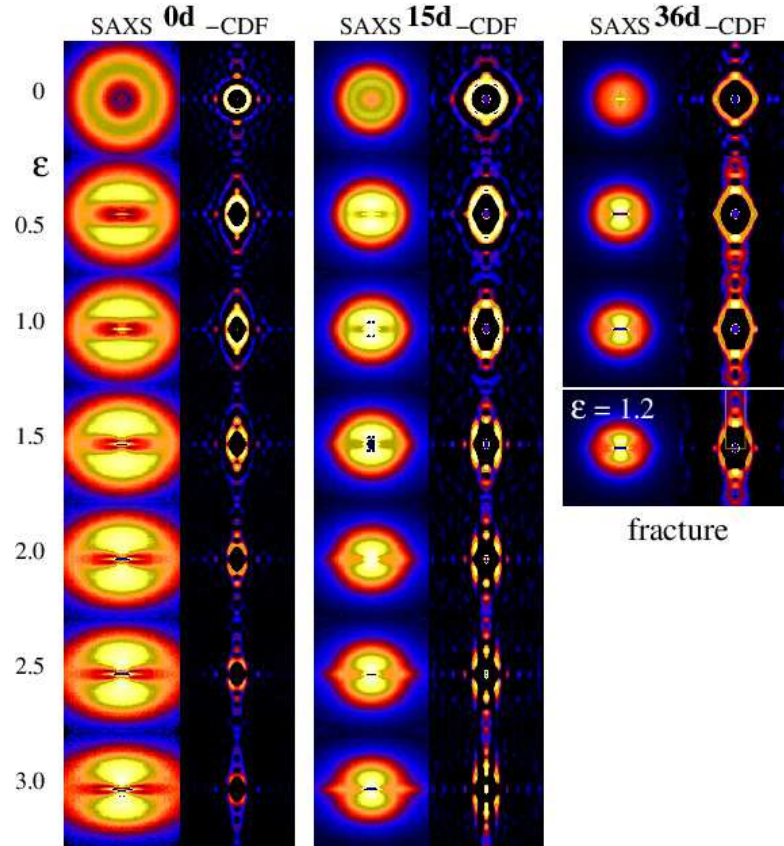


Figure 4.2.2: Selected SAXS data of the materials collected during continuous straining experiments. The strain ε is labeled in the text column. In each block on the left the scattering intensity (“SAXS”) is presented. This is $I(s_{12}, s_3)$, $-0.2 \text{ nm}^{-1} \leq s_{12}, s_3 \leq 0.2 \text{ nm}^{-1}$. The right pattern in each block presents the long-period peaks in the chord distribution function (“-CDF”), $-z(r_{12}, r_3)$, $-50 \text{ nm} \leq r_{12}, r_3 \leq 50 \text{ nm}$. The pseudo-color intensity scales are identical within each material. The straining direction (s_3 , r_3 resp.) is vertical. A rectangle in a pattern (above the label “fracture”) indicates the regions which are presented in Figure 4.2.3

Table 4.1: Morphological parameters of the unstrained materials. The numbers and asymptotic intervals of confidence are computed by nonlinear regression on the IDF using the “duo-solo” model. Missing intervals indicate that numbers are exact up to the last shown digit. W_i are the weights of the two components. \overline{H}_h and \overline{H}_s are the average domain heights of hard and soft domains and $c = \overline{H}_h + \overline{H}_s$ is the long period

sample	W_{duo} [a.u.]	W_{solo} [a.u.]	\overline{H}_h [nm]	\overline{H}_s [nm]	\overline{L} [nm]
0 d	0.61	2.50	5.2	3.0	8.2
15 d	0.36±0.08	1.05±0.14	7.5	5.6±1.5	13.1±1.5
36 d	0.04±0.02	0.49±0.02	7.3	8.8±2.5	16.1±2.5

neighborhood of a domain: Each peak shows, in which direction and distance neighbor domains are found.

For each experiment a block of images is presented. The upper patterns in a block show the data of the unstrained isotropic materials. They are followed below by selected patterns from the tensile test. A text column indicates the strain ε . Sample 36 d breaks at $\varepsilon = 1.5$.

All the unstrained ($\varepsilon = 0$) samples in the top row show isotropic SAXS with a ring-shaped long-period reflection, but with the aged samples the reflection is found at smaller s . The long period has grown. Quantitative morphological data are presented in Table 4.1. $\overline{H}_h W_{total} = \overline{H}_h (W_{duo} + W_{solo})$ (cf. Eq. (3.7.3)) is proportional to the volume fraction of hard domains. Thus the very strong decrease of the weights after aging reflects a considerable decrease of v_h ($v_{h,0d}/v_{h,15d} = 2.2$, $v_{h,0d}/v_{h,36d} = 4.5$). Aging increases the average thickness \overline{H}_h of the hard domains, and the average distance \overline{H}_s between them increases even more. This increase of \overline{H}_s supports the finding of a decrease of v_h .

Our findings are in agreement with the results of other studies on high-temperature aging of TPU. The increase of \overline{H}_h has frequently been reported in the literature[142, 143, 144]. In principle, it may be due to an annealing effect (mechanisms: growing hard domains[35] or agglomeration of hard domains[137, 242]), or it may be related to selective disappearance[35] of small hard domains. Even our finding of a considerable increase of \overline{H}_s is not new[140, 144].

Taking into account the observed increase of \overline{H}_s , hard-domain growth appears to be impossible and agglomeration improbable. The most probable mechanism appears to be a selective degradation of the smaller hard domains. This assessment is supported by reported results that thermal degradation affects first the hard domains[134, 145, 146].

Qualitative Description of the Morphology Evolution During Straining. Figure 4.2.2 shows as a function of increasing ε the typical conversion of the isotropic SAXS patterns of samples 0 d, 15 d, and 36 d into a layer line pattern. In the CDF and with increasing strain the strong peaks concentrate in a narrow strip along the vertical line (meridian). This shows that the morphology of the correlated domains becomes microfibrillar[243],

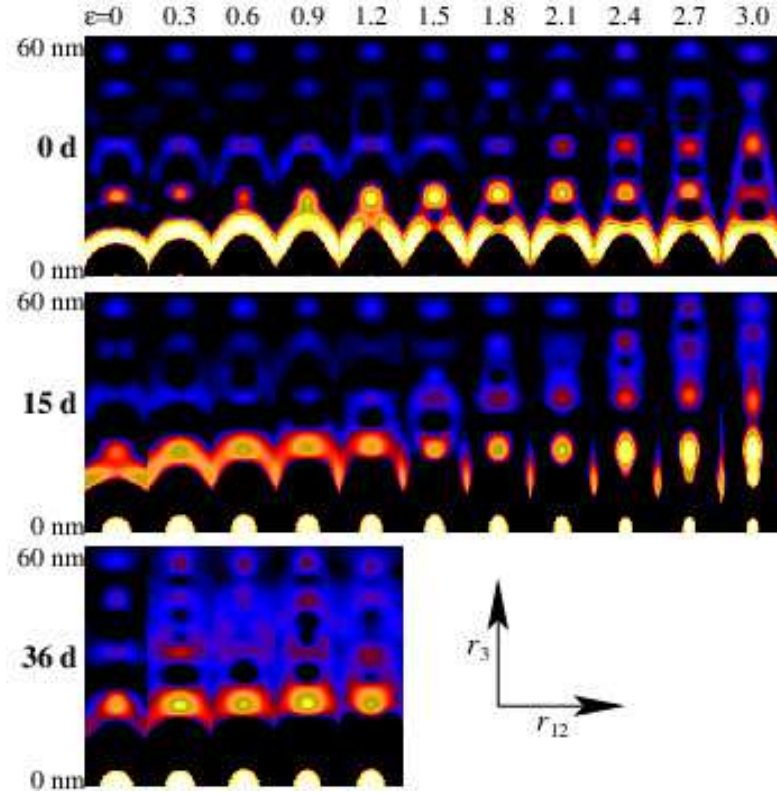


Figure 4.2.3: Nanostructure evolution of a differently aged TPU (top to bottom) presented in regions cut from the CDFs $-z(r_{12}, r_3)$ around the meridian as a function of ε (left to right). $-z(r_{12}, r_3)$ $0 \leq r_3 \leq 60$ nm, $|r_{12}| \leq 8$ nm is presented on a varying $\log(\log(-z))$ intensity scale. The peaks are the long-period peaks of differently arranged hard domains. Peaks are not continuously growing with strain, but are bound to “ L -bands”. For the cutting region cf. Figure 4.2.2

in principle. In this study we are not discussing the indications of three-dimensional arrangement of hard domains. Thus, putting meridional strips of the CDFs on a wall-paper the features of the longitudinal nanostructure evolution are readily demonstrated. This screening method has been introduced in previous work[58, 234, 238]. Figure 4.2.3 presents the results. The peaks in the figure are long-period reflections. They originate from arrangements of hard domains which form ensembles. In all materials we observe a peculiar behavior that recently has been found and described by us: With increasing ε the peaks do not move continuously long distances. Instead, they keep bound to “ L -bands” and only within these bands a limited mobility of the peaks is observed. This indicates that the arranged ensembles of hard domains possess only a limited extensibility. Such a morphology cannot be fitted by an infinite “paracrystalline model” or a “stacking model”, respectively. As we have already mentioned in the data evaluation section, we choose a

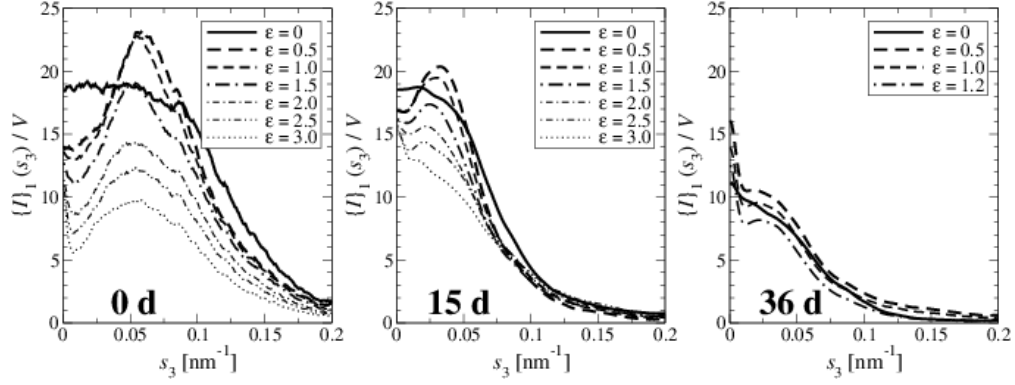


Figure 4.2.4: Variation of the longitudinal projected scattering $\{I\}_1(s_3)$ in the tensile tests of a TPU material as a function of both the aging duration and the strain ε . Intensities are normalized for the beam flux and the irradiated volume

finite model in which only the peak in the lowest L -band is fitted. The significance of this assumption must be explained, because in Figure 4.2.3 the higher peaks look as if they were comparably strong. Nevertheless, this is nothing but an intended effect of the special presentation which has been designed in order to visualize the set of correlations in the material (in the figure the intensity $-z(r_{12}, r_3)$ is presented as $\log(\log(-z(r_{12}, r_3)))$).

4.2.3 Quantitative Analysis of the SAXS Data

Bonart’s “Longitudinal Scattering”. Even if the morphology of the materials is as complex as revealed in the CDFs with uniaxial symmetry (cf. Figure 4.2.2 and Figure 4.2.3), it is still possible to quantitatively study the arrangement and the extension of the hard domains in the straining direction. For this purpose Bonart[216] has proposed to study the projection $\{I\}_1(s_3)/V$ (cf. Eq. (3.7.1)), which is well-founded in the scattering theory. At a first glance, the curves $\{I\}_1(s_3)/V$ (Figure 4.2.4) give an impression on the variation of the long-period peak and of the scattering power Q , which is the integral under the curves. We observe that Q decreases considerably with increasing duration of the aging. This is another indication for selective degradation[35, 145, 146] of small hard domains, as is the left-shift of the peak (increase of the long period).

Results of the IDF Analysis. $\{I\}_1(s_3)/V$ is a one-dimensional intensity which is transformed into the IDF $g_1(r_3)$. It collects information on the sequences of the finite chords which run in the straining direction r_3 . The fitting of the IDF has been explained in a separate section. The quantities which will be discussed from now on are computed by fitting the IDFs (cf. Figure 3.7.2) to the already presented duo-solo model.

Figure 4.2.5 displays the quantity cv_h (cf. Eq. (3.7.3) which is proportional to the volume fraction v_h of hard domains. The reduction after aging has already been addressed in the discussion of Table 4.1. The curve of the unaged material shows an initial increase

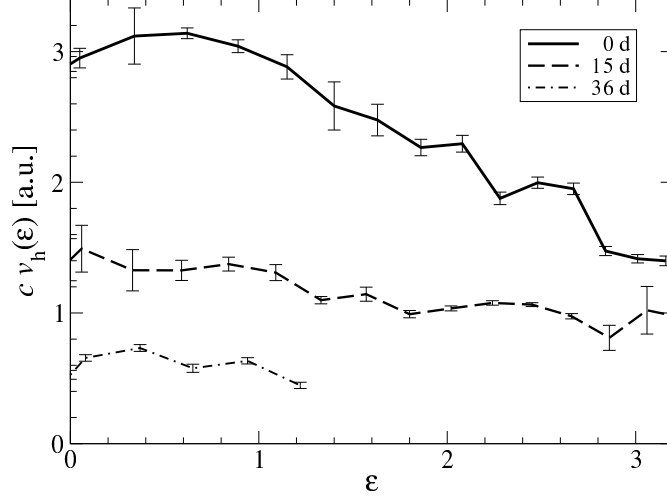


Figure 4.2.5: Variation of the total volume fraction of hard-domains, $v_h(\varepsilon)$ in the straining experiments of a TPU aged for different time at 150 °C. Error bars indicate intervals of confidence[212] as determined by the regression program. The actual errors may be wider

for $\varepsilon < 0.6$ and after that a continuous, almost linear decrease. The same curve shape has been found in earlier work[244] for other TPU materials. By scaling the 3 curves to a master curve it is readily demonstrated that, to a first approximation, the relative loss of hard-domains with increasing strain is the same for all samples. We imagine that the continuous destruction of hard domains releases more and more chains into the soft phase, which that way accomplishes the macroscopic strain.

From Eq. (3.7.3) it is obvious that the hard domain volume can be split into two fractions. The hard domains collected by W_{solo} are randomly placed without any correlation to other domains, whereas the domains collected by W_{duo} are arranged. Only they contribute to the discrete scattering, and only they carry information on topological arrangement. Figure 4.2.6 displays the results. Assuming that the actual error bars are about 3times the estimated ones, smoothed curves are drawn through the data. Thin curves are related to the randomly placed domains, bold ones to arranged domains. For all samples and all strains there are more domains placed at random than arranged. In the unaged material $\approx 75\%$ of the hard domains are placed at random, and this relation hardly changes with increasing strain.

This is different for the aged materials. Here for $\varepsilon < 0.6$ hard domains are transferred from random placement into arrangement. With respect to the measured SAXS pattern this means that the strength of the long-period peak grows, although not a single domain is formed. For $\varepsilon > 0.6$ the transfer is inverted. Now hard domains migrate back from the arranged phase into the random one. The strong decrease of the discrete scattering is not related to a correspondingly strong destruction of domains. For 15 d and $\varepsilon > 2$ we do not discuss the indicated “back-migration” because of poor statistics.

4.2 Ageing Effect on Morphological Evolution of PUE under Strain

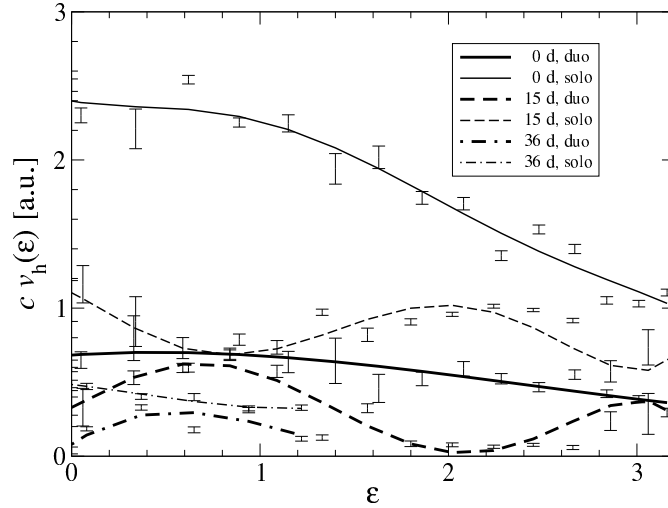


Figure 4.2.6: Separation of the volume fractions of hard-domains $v_h(\varepsilon)$ into those hard domains which are placed at random (“solo”), and arranged ones (“duo”). The curves show the variation in straining experiments of a TPU aged for different time at 150 °C. Error bars indicate intervals of confidence as determined by the regression program. The actual errors are assumed to be wider

Figure 4.2.7 shows the variation of the average hard-domain height, $\overline{H}_h(\varepsilon)$ with increasing strain for the three samples. For sample 0 d \overline{H}_h does not change. This has also been found in previous work[244] on various similar TPU materials. The unaged material has rigid hard domains.

For both aged materials $\overline{H}_h(\varepsilon)$ starts with an increase from $\overline{H}_h(0) = 7$ nm to $\overline{H}_h(1) = 10$ nm. Considering, in addition (Figure 4.2.5), that there is little change of v_h in the interval $0 < \varepsilon < 1$ we conclude that the thermal aging is softening many of the hard domains. Thus our morphology evolution data are in good agreement with other work[134, 145, 146] stating that high-temperature thermal aging affects first the hard domains. Moreover, we quantify the softening effect and find that it is the same for both aged materials. From the stress-strain curves (Figure 4.2.1) we see that for sample 15 d the hard-domain softening leads to global softening, but not for sample 36 d. Sample 36 d breaks at $\varepsilon \approx 1.5$, while sample 15 d passes the tensile test. This difference is readily explained by literature results stating that the soft phase is only affected in a second, later stage[145, 146] which goes along with cross-linking, chain scission and decrease of the mechanical performance. For sample 15 d the course of the curve for $\varepsilon > 1$ shows an asymptotic decrease of $\overline{H}_h(\varepsilon)$ towards the height of the unaged material. This result can be explained by assuming that the softened hard domains fail earlier than the remaining rigid ones.

Figure 4.2.8 presents the variation of the average soft-domain height $\overline{H}_s(\varepsilon)$ between two arranged hard-domains as a function of strain. The unaged material shows a linear increase for $0 < \varepsilon < 0.6$ (elastic response) which is followed by a peculiar relaxation.

4 Results and Discussion

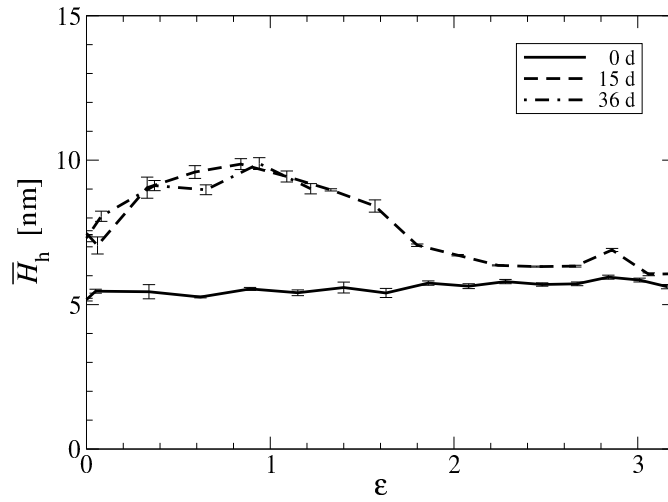


Figure 4.2.7: Differently aged TPU. Average hard-domain height \bar{H}_h measured in straining direction r_3 as a function of strain ϵ

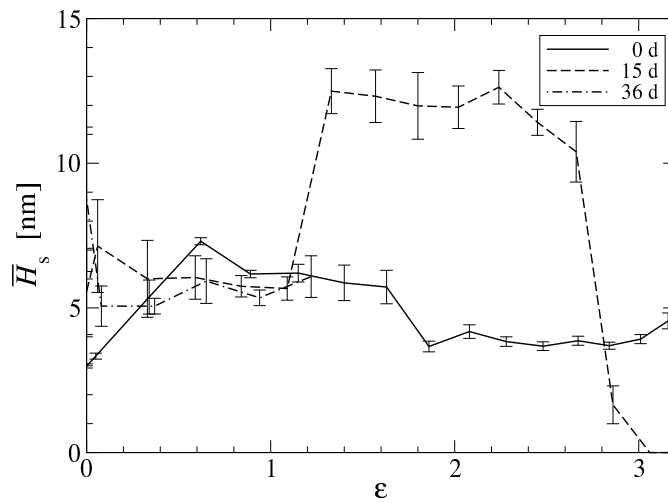


Figure 4.2.8: Differently aged TPU. Average soft-domain height \bar{H}_s between correlated hard domains as a function of strain ϵ . \bar{H}_s is measured in straining direction r_3

4.3 Failure Mechanisms of Crosslinked PUE with Poorly Developed Domain Structure

This peculiar “relief” process has been reported previously not only by us[238], but also by several other authors[167, 168, 169, 96, 112, 102, 170]. For the aged samples at $\varepsilon < 1$ $\overline{H}_s(\varepsilon) \approx 5$ nm is indicated. This indicates that for $\varepsilon < 1$ the lengthening is taking place in the softened hard-domains and in the poorly arranged regions (PAR) where the hard domains are placed randomly. For the soft-domain heights in the arranged entities no significant trend is indicated. At $\varepsilon = 1.5$ sample 36 d breaks, whereas sample 15 d resists. At $\varepsilon \approx 1.2$ it exhibits a length jump to $\overline{H}_s(\varepsilon) \approx 12$ nm. Considering a sequence of arranged hard domains, such length jump would be observed if approximately every second hard domain from the arranged regions would suddenly be disrupted. For $\varepsilon > 2.6$ a steep decrease is observed which may be explained by predominant failure of hard domains from stretched, correlated entities while domains from slack entities are not destroyed.

We do not report the fitted widths of the domain-height distributions because of low significance with the aged samples. For half of the analyzed curves the estimated interval of confidence is wider than the value that gives the best fit of the SAXS data.

4.2.4 Conclusion

In the present study, we have coupled thermal aging tests on TPU with an in-situ study of the morphology evolution in tensile tests. Our morphological findings on the unstretched specimens confirm relations between high-temperature aging and the two-phase morphology which are known from the literature. New are our results concerning the structural change upon stretching. The thermal aging not only reduces the number of hard domains, it even softens many of them. The softened hard domains deform under mechanical load and fail earlier than the remaining rigid domains. Only for $\varepsilon > 0.6$ begins the usual “division of labor” between the hard phase (rigid physical network points) and soft phase (deformation).

Beyond that, the interplay between randomly placed hard domains and a rudimentary arrangement in the aged samples appears to be of academic interest, at least. In the beginning of the tensile test the hard domains and the matrix both are deformable. In this morphology, further order is formed upon stretching. Once the remaining hard domains take over their role as rigid fillers again, the intermediate order declines again.

4.3 Failure Mechanisms of Crosslinked PUE with Poorly Developed Domain Structure

In this section², we present an investigation of poorly ordered materials under mechanical load monitored by small-angle X-ray scattering (SAXS). The isotropic virgin samples are strained, oriented, and two-dimensional (2D) SAXS patterns are recorded. Most of our materials fail at relatively low strain, but two materials are more extensible.

²This section based on the paper published in the Macromolecular Materials and Engineering 2015, 300(7), 699-711.

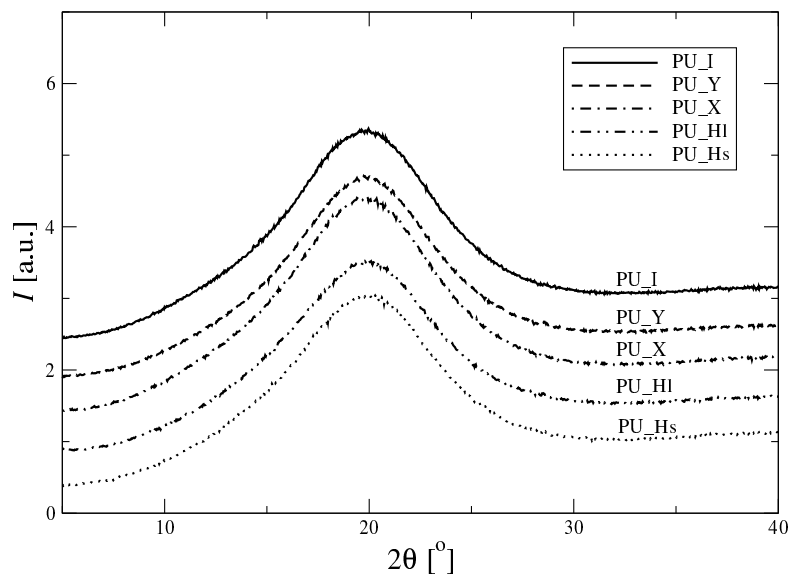


Figure 4.3.1: WAXS scans of the isotropic samples.

We have prepared a series of chemically crosslinked PUE, in which the polymer network topology has been varied widely, with the objective to study the polymer morphology and how this morphology changes upon submission to high strains. The polyols are telechelic in nature that means that they carry hydroxyl groups at the chain ends. The number of the hydroxyl groups per chain is referred to as the functionality of the polyol and is varied from 2 to 4. The molecular weight and the topology of the polyol chains have been varied. In the PU technology it is common to use linear polyols (with a functionality of 2) and three-functional polyols of which the three branches are equal in length. In this study we wish to find out how the high strain properties are affected by the chain topology of the polyol. Hence our interests in molecular failure mechanisms on the nanometer scale.

4.3.1 Amorphous Materials

We have carried out wide-angle X-ray scattering (WAXS) scans of the isotropic materials which is shown in Figure 4.3.1. All samples show only a broad amorphous halo with a maximum at $2\theta \approx 20^\circ$. Crystallites cannot be detected.

4.3.2 Stress-strain Curve

Stress-strain curves of the materials are shown in Figure 4.3.2. The materials break at the end of the curves.

4.3.3 Features of the SAXS Patterns Related to Strain and Material

Figure 4.3.3 shows the recorded scattering patterns and the CDFs computed thereof.

4.3 Failure Mechanisms of Crosslinked PUE with Poorly Developed Domain Structure

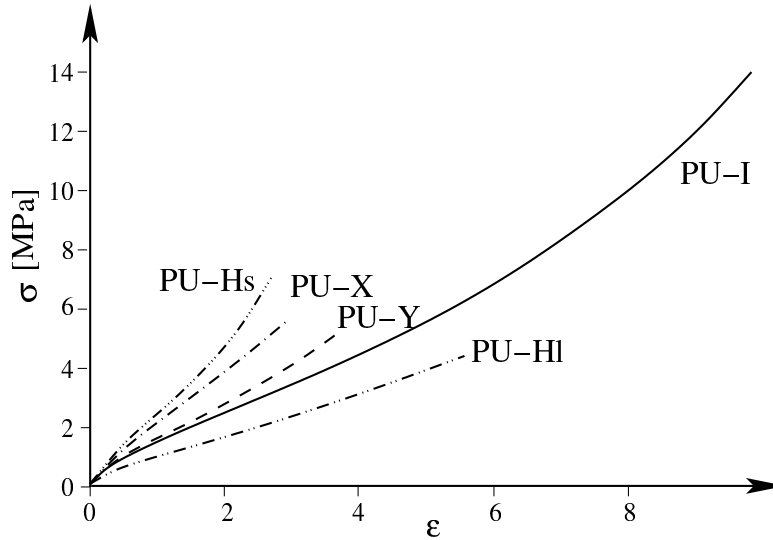


Figure 4.3.2: Stress σ as a function of the strain ϵ of the polyurethane materials.

Since some of the studied samples scatter very weakly, artifacts of the Fourier-transform may interfere with weak peaks of the CDF. Therefore, the CDFs of some materials are not suitable for a full quantitative evaluation. For each experiment a block of images is presented. The upper patterns in each block display the data of the unstrained isotropic materials. Below are shown selected patterns from the tensile test. Along the left edge rounded percentages of the strain ϵ are put down. They are related to the test of PU-I. For the other materials this sequence is valid, too, except for the bottom row which displays the status just before failure.

CDFs visualize the local structure in the neighborhood of a domain: Each peak shows, in which direction and distance neighbor domains are found that generate a long period. The integral of a peak is a measure of the population density. The influence of artifacts to the strongest peaks appears to be low, therefore they are discussed for all materials. The best-correlated nanostructure is shown by PU-I and PU-Y. As soon as the materials have been oriented, there are strong peaks both on the meridian (central vertical line) and on lines parallel to the meridian. The peaks on the meridian describe correlations among hard domains that are arranged along a thread[165] in the straining direction. The corresponding scattering entity is called a microfibril[243]. Beyond that, strong peaks to the right and to the left of the meridian exhibit 3D connectivity[112]. Accordingly, a hard domain finds neighbors not only in its own microfibril, but also in the neighboring ones. This is readily explained by assuming that there are tie molecules connecting neighboring hard domains[112]. Under strain the shortest connection, i.e. the tie molecule, defines the inter-domain distance.

With material PU-X this is different. Here, only 1D[165] correlation is formed in the straining direction. There are no significant correlations with hard domains from surrounding microfibrils. The reason is probably a lower level of phase separation in

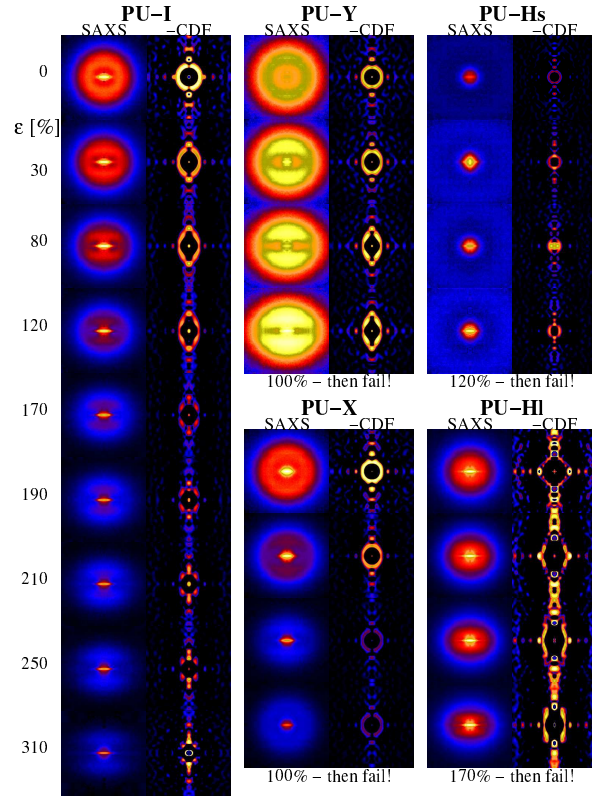


Figure 4.3.3: Selected SAXS data of the materials collected during continuous straining experiments. Percentages of the strain ε are labeled on the left side. In each block on the left the central part of the scattering intensity (“SAXS”) is presented. This is $I(s_{12}, s_3)$, $-0.2 \text{ nm}^{-1} \leq s_{12}, s_3 \leq 0.2 \text{ nm}^{-1}$. The right pattern in each block presents the long-period peaks in the chord distribution function (“-CDF”), $-z(r_{12}, r_3)$, $-50 \text{ nm} \leq r_{12}, r_3 \leq 50 \text{ nm}$. The logarithmic intensity scales are identical with each material. The bottom row in the short blocks (failing materials) presents the last record before failure

PU-X.

The material PU-HI exhibits only strong diffuse scattering that falls off from the center. This is typical for the scattering of uncorrelated domains (“particle scattering”). When the material is strained, the envelope shape changes from a circle to an ellipse. This is explained by either orientation of anisotropic hard domains, or by domain deformation under load. Accordingly, in PU-HI the hard domains appear randomly distributed in the volume. Even under strain no correlation is generated among them. Because the displayed CDFs do not show strong correlation peaks, the features visible after scaling the image are predominantly artifacts. The sample PU-Hs exhibits hardly any discrete scattering. A discussion of CDFs is inappropriate.

Failure Related to Morphology. Only sample PU-I survives the strain test. PU-Y, PU-X and PU-Hs fail at $\varepsilon \approx 1.2$, PU-Hl at $\varepsilon \approx 1.8$. For some of the materials, morphological and network-topological characteristics can readily be related to failure. PU-Hs has not developed hard domains (physical crosslinks) and has the highest crosslink density of all the 5 samples. In PU-Hl there is no connectivity among the hard domains. It appears noteworthy that a placement of hard domains without connectivity results in better mechanical properties than a 1D concatenation. Anticipating a further result the domains of PU-Hl survive. This may be explained by the missing of tie molecules that otherwise would limit the range of the elastic response of the soft matrix. PU-X appears to fail early, because here the few physical crosslinks are only interconnected linearly. Moreover, the extensibility of the polymer network is reduced because of the high functionality ($f = 4$) of the employed polyol.

Finally it remains to be clarified, why PU-Y fails in the tensile test, although the CDFs of PU-I and PU-Y exhibit the same 3D connectivity. The big difference is the course of the scattering intensities. With PU-I the intensity decreases during the test, indicating that considerable amounts of hard domains are continuously sacrificed. Thus we observe the decomposition that has been discussed by Enderle et al.[112], and the predominance of this mechanism may be explained by the chain topology of PU-I. Because of the linear chain structure the hard-domain integrity should be rather low with PU-I, and chains can easily be pulled out from hard domains without chain rupture. The reason for low hard-domain integrity with PU-I is the fact that soft segments of linear PUEs are easily incorporated into hard domains[169, 245]. On the other hand, with PU-Y the intensity in the long-period peak increases clearly during straining. Admittedly, this could be an orientation effect only, if the existing isotropic intensity were simply focused at two points in the reciprocal space while the invariant Q would stay constant. For a two-phase system $Q = v_h (1 - v_h) (\rho_h - \rho_s)^2$ is valid with v_h being the volume fraction of hard domains, and ρ_h and ρ_s being the electron densities of the hard phase and the soft phase, respectively. In the following analysis we will demonstrate, that Q is increasing in the test of PU-Y. Considering a decreasing $v_h < 0.3$, the only explanation is increase of the contrast $|\rho_h - \rho_s|$ between the hard domains and the soft phase. Such increase could be caused from hard domains that become more and more perfect (increasing phase separation). Nevertheless, it appears more probable that the density ρ_s of the soft phase between the well-arranged hard domain entities decreases with increasing strain (for a sketch cf. Figure 4.3.7c). A similar deformation process is known from hard elastic polyolefins[246] where the density decrease even leads to interdomain voids.

Voids. Generation of nanoscale voids in the material would be indicated by an increase of the intensity in the equatorial streak that is extending in horizontal direction in the center of the scattering patterns. Even a moderate increase of voids would lead to a strong increase of the equator scattering. With PU-I and PU-Y no change is observed. The slight increase with the other materials appears to be irrelevant. Other PUE materials that have been studied during the same experimental period grow white and exhibit a strong increase of the equatorial scattering.

Table 4.2: Long periods L of the unstrained isotropic materials

sample	L [nm]
PU-I	10.4
PU-Y	8.9
PU-X	8.9
PU-Hs	—
PU-Hl	10.9

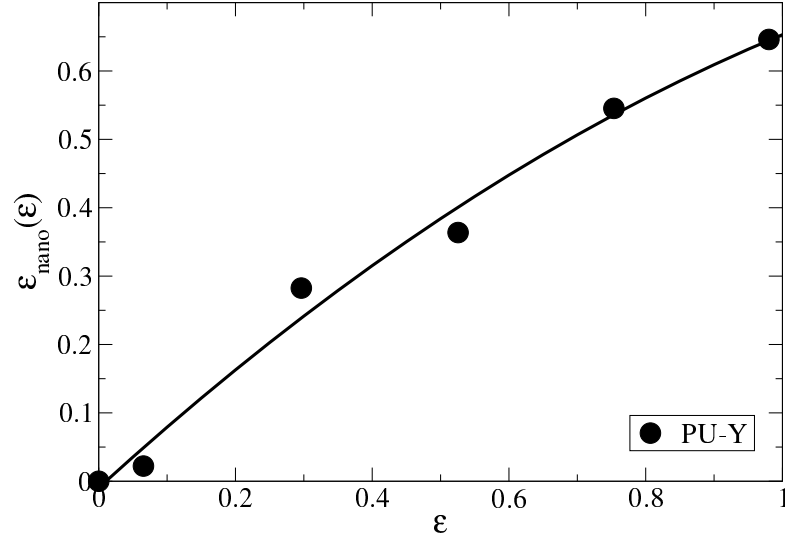


Figure 4.3.4: PU-Y: Nanoscopic strain $\varepsilon_{nano} = L(\varepsilon)/L(0) - 1$ computed from the change of the long period L as a function of the macroscopic local strain ε at the irradiation point

4.3.4 Long Periods

For the virgin samples the common method of long-period determination has been employed, i.e. the values reported in Table 4.2 are determined from the position of the peak maximum in the curve $s^2 I(s)$. The peaks are extremely wide. Thus the reported values may be far from the number-average long period. Material PU-Hs exhibits diffuse scattering only. A long period cannot be determined.

Only with PU-Y the long period reflection is strong enough for an analysis of its movement $L(\varepsilon)$. From $L(\varepsilon)$ the apparent nanoscopic strain $\varepsilon_{nano}(\varepsilon)$ is computed. The result is presented in Figure 4.3.4. In the ideal case $\varepsilon_{nano}(\varepsilon) = \varepsilon$ would be valid, but the plot shows a deviation. At a macroscopic strain of 100%, the well-arranged entities[61] that make the reflection are only strained to $\varepsilon_{nano} = 0.65$. This effect has been reported by others[96, 87] and explained by breaking the hard domains into pieces accompanied by a reduction of the average distance among the fragments. The proposed mechanism is homogeneous in the sense that the evolution of morphology is acting on all the hard

4.3 Failure Mechanisms of Crosslinked PUE with Poorly Developed Domain Structure

domains of the material in the same way. In contrast, some of us have demonstrated in a recent study[61] that the observed long-period reduction[96] has been related to a heterogeneous process in which well-arranged hard-domain ensembles can be discriminated from hard domain ensembles that have failed. The apparent unusual peak shift has been a consequence of the fact that the well-arranged hard-domain ensembles experience stress relief. The relief has been a reaction on the sacrifice of weaker hard-domains. Sacrificed hard domains are fragmented, but then the distance to their neighbors (long period) does not decrease as is essential for the other model[96, 87]. Instead, it jumps up reaching the value that is related to the actual macroscopic strain[61]. This mechanism has been found by a CDF analysis. It cannot be seen directly in the SAXS pattern, because it applies to a smaller fraction of hard domains. Thus their discrete scattering effect is low and the visible peak in the SAXS pattern is dominated by the relief process. Moreover, in all materials there may be a portion of uncorrelated matter (like in material PU-HI) whose straining cannot be monitored by SAXS at all, because there regularity does not even exist.

The long-period lag in PU-Y indicates that the mentioned sacrifice mechanism is probably active here, as well. In this case, an observed increase of Q presents only a part of the contrast enhancement, since another part of the real increase is simultaneously sacrificed by destroying hard domains and thus reducing v_h .

4.3.5 Lateral Hard Domain Extension

The breadth e_h of the domain peak in the CDF is some measure of the average lateral extension of the hard domains in the direction perpendicular to the strain (transverse direction). Such lateral extensions have been discussed in detail in previous work[247]. e_h can be determined for all materials that contain hard domains and thus exhibit particle scattering. Figure 4.3.5 presents the results. The reasons for changes can be quite complex, because only an average over the remnant domains is observed. We would tend to relate the steep decrease of PU-HI to the fact that its hard domains do not interact with each other mechanically. So they can orient more easily with their long axes parallel to the strain.

In the other materials we find ensembles of hard domains, which form a network, because they are physically crosslinked by short tie molecules among them. Here the hard domains play the role of spreaders in a (here: three-dimensional) fishing net. Under uniaxial strain the spreaders hold the meshes open in transverse direction. Figure 4.3.5 demonstrates a decay of spreading that is similar for all materials with hard domains that act as physical crosslinks. Increasing polyol functionality (I \rightarrow Y \rightarrow X) appears to slightly reduce the network spread.

4.3.6 Analysis of Bonart's Longitudinal Structure

Figure 4.3.3 demonstrates that the discrete scattering of most samples is not very pronounced. This makes it difficult to analyze the CDFs of several materials quantitatively. Thus we additionally analyze the projection[193] $\{I\}_1(s_3)/V$ of the fiber diagram on

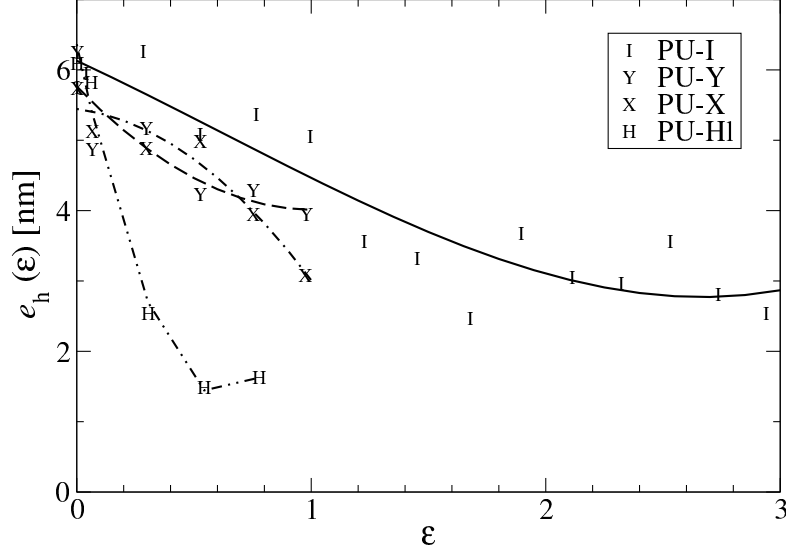


Figure 4.3.5: Extension e_h of hard domains transverse to the straining direction as a function of the macroscopic strain ε

the straining direction s_3 . Bonart has called this 1D scattering curve the “longitudinal structure”. It describes[216, 222] the sequence of chord lengths (thicknesses) of hard domains and soft-phase gaps measured in the direction of strain. Moreover, the area below the curve, $\int \{I\}_1(s_3)/V ds_3 = Q$, is the scattering invariant that has already been introduced.

Figure 4.3.6 presents the evolutions of $\{I\}_1(s_3)/V$ in the tensile tests. Let us first discuss the two materials that exhibit 3D connectivity among their hard domains. For PU-I (Figure 4.3.6a) the indicated long-period peak moves to higher s_3 -values with increasing $\varepsilon > 1$. Thus further increasing a high strain, the long period decreases[96, 61]. Explanations have already been presented (fragmentation or sacrifice mechanism). In addition, the scattering power Q decreases significantly with increasing strain up to $\varepsilon \approx 2.5$. This demonstrates a decrease of v_h . Many hard domains are destroyed. So in the material that is showing the highest elongation at break ε_b , the stipulated hard domain stability[6] is not that high. PU-Y (Figure 4.3.6b) fails early. The initial invariant is quite similar to that of PU-I. On the other hand, the evolution of $\{I\}_1(s_3)$ is completely different: Firstly, with increasing strain a long period peak grows and moves in the regular direction, even if the movement is slower than expected. This has been described quantitatively in Figure 4.3.4. Secondly, the invariant Q is increasing. Nevertheless, the curves $\{I\}_1(s_3)/V$ demonstrate that the increase is not as big as it seems in the direct comparison of the scattering intensities (Figure 4.3.3). Thus orientation of the scattering entities is also an important factor. However, we have already discussed indications that even in this material hard domains are sacrificed. Under this premise the decrease of v_h must be accompanied by a considerable increase of the contrast $|\rho_h - \rho_s|$ resulting in the observed net increase of Q . Thus the additional mechanism that lets PU-Y fail as compared to

4.3 Failure Mechanisms of Crosslinked PUE with Poorly Developed Domain Structure

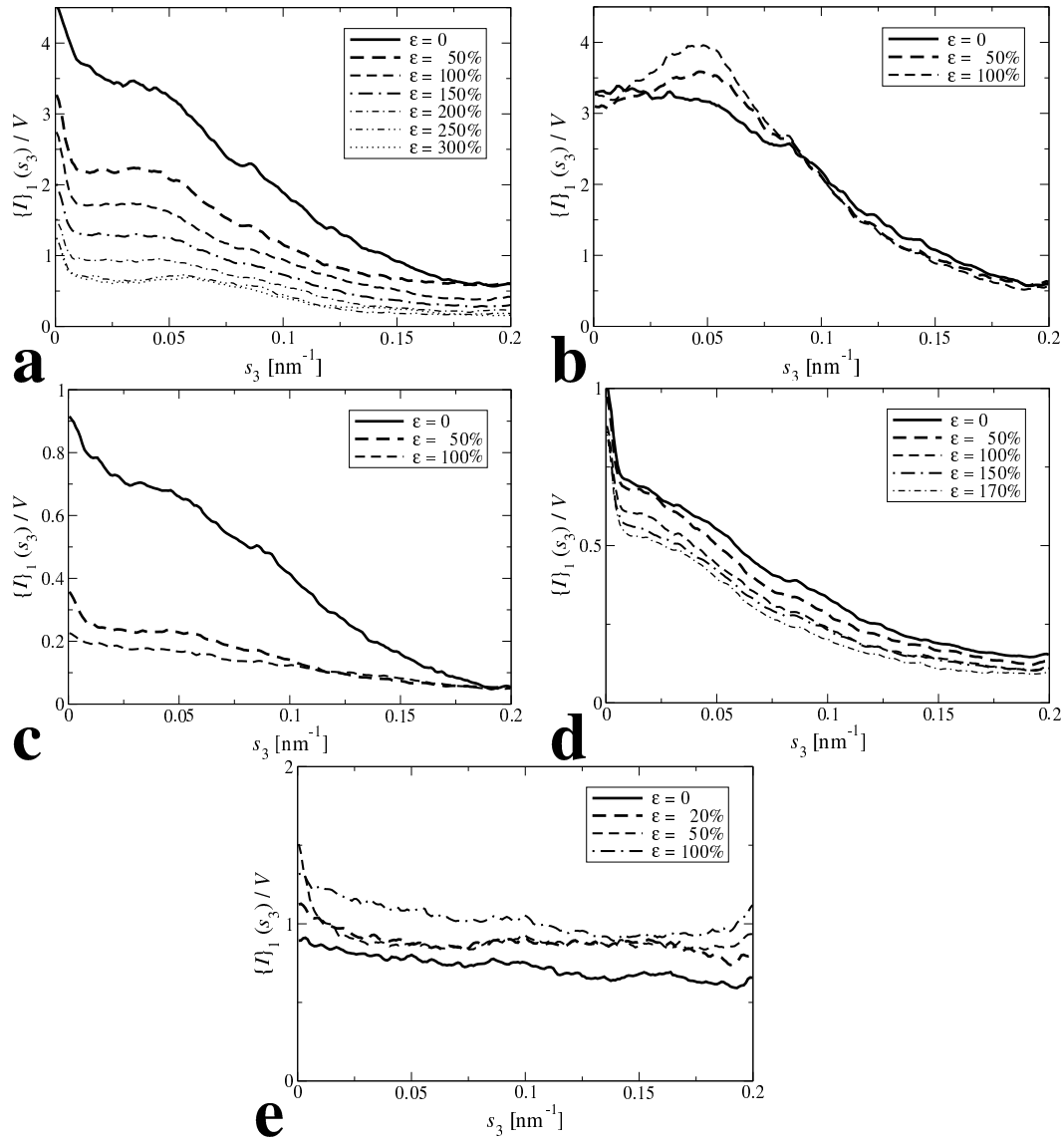


Figure 4.3.6: Variation of the longitudinal structure $\{I\}_1(s_3)$ during the tensile test as a function of the macroscopic strain ε for the studied materials. **a)** PU-I, **b)** PU-Y, **c)** PU-X, **d)** PU-HI, **e)** PU-Hs

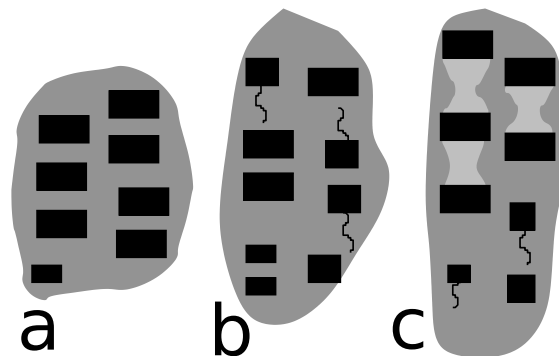


Figure 4.3.7: Suggested straining mechanisms in material containing correlated hard domains. a) Low strains. Hard domains (black) in a homogeneous soft matrix. b) Sacrifice mechanisms. Broken domains with dangling chains. c) Loop-hole mechanisms if hard domains are too stable (PU-Y): Volume increase between domains leads to density decrease (light gray). between hard domains that act as spreaders.

PU-I is most probably a reduction of the soft-phase density among well-arranged hard domains.

Now let us sketch a failure mechanism that is compatible with our observations. The morphology in both PU-I and PU-Y is characterized by a 3D arrangement of hard domains seized by tie molecules. In response to the mechanical load the tie molecules get taut and a peculiar[61] straining mechanism sets in: the sacrifice of weak hard domains creates locally extended entities that break some meshes and serve the macroscopic strain. In PU-I the initial moderate heterogeneity of the morphology is conserved, although more and more hard domains are broken. ε_b is high because at any excess strain there are just enough weak hard domains to be blown (like fuses).

In PU-Y the hard domains appear more stable than with PU-I. Thus the sacrifice process cannot create sufficient relief. The material is extended, but between the hard domains the lateral contraction of the soft material is restricted. Volume increase at constant mass leads to density decrease between the hard domains. Thus high hard-domain stability [6] may force the morphology to turn more heterogeneous by forming an additional phase of soft material with reduced density. We speculate that related peak stresses in the soft phase may initiate the macroscopic failure of the elastomer.

Figure 4.3.7 presents a sketch of the indicated straining and failure mechanisms. Figure 4.3.7a sketches the oriented morphology at low strain. In Figure 4.3.7b the sacrifice mechanism is sketched: although tie molecules block further straining, the nanostructure can serve the strain by starting to sacrifice hard domains. Figure 4.3.7c sketches the case of PU-Y where the required volume increase between rigid hard domains is accomplished by density decrease (shades of gray) similar to the mechanism known from hard-elastic polyolefins[246].

Figure 4.3.6c demonstrates the structure evolution for the material PU-X. Here the

4.3 Failure Mechanisms of Crosslinked PUE with Poorly Developed Domain Structure

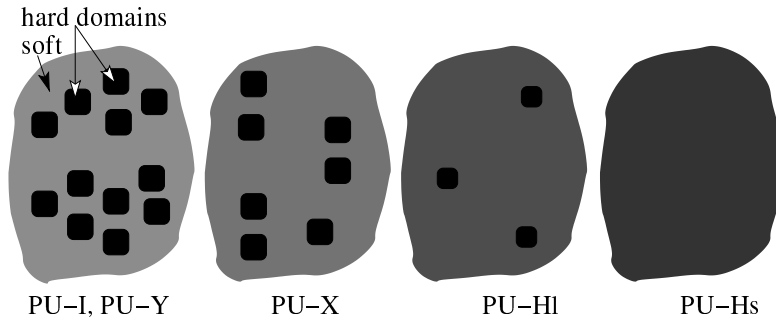


Figure 4.3.8: Sketch of the local arrangements of hard domains and the phase separation for the studied materials.

CDFs have shown that hard domains are only interconnected in 1D threads. The scattering power of PU-X is considerably lower than that of PU-I and PU-Y. This indicates that there are considerably less hard domains in PU-X than in the previously discussed materials with lower functionality of the polyols. Only small strains are required to destroy the nanostructure. Macroscopically the material fails at a strain just above 1.0.

The scattering patterns of the material PU-HI are dominated by particle scattering (cf. Figure 4.3.3) that is related to an ensemble of uncorrelated hard domains. Figure 4.3.6d shows the response of this particle scattering to strain. The invariant Q is small, but there is only little decrease during the tensile test. This result demonstrates that only few of the hard domains are destroyed. A possible cause that may prevent hard domains from destruction has already been discussed. The sparse hard domains are not interconnected by short tie molecules. The fair mechanical performance of PU-HI may be explained by a stabilizing effect of each isolated hard domain similar to that of a filler particle in a rubber.

Figure 4.3.6e presents the longitudinal structure for the material PU-Hs. The scattering is a plain density fluctuation background, the SAXS of an unstructured material. Nevertheless, the background scattering is quite high. The reason may be that in the polyurethane chains blocks of different electron density (related to hard modules and soft modules) are randomly distributed. With increasing strain ε the density fluctuation background increases slightly. This increase is most probably no chain orientation effect, because we have found that Bonart's transverse[222, 193] scattering, $I_2(s_{12})$, does not change as a function of ε .

In summary, the SAXS sees a different kinds of scattering entities for the five materials that have been studied. Figure 4.3.8 presents an overview of the local arrangements of hard domains that is found. The darker the background, the more hard modules are mixed into the soft phase. The more dense the material is populated with hard domains, the more complex is their arrangement. 3D arrangement is only found in the well phase-separated materials with bi- or trifunctional polyols (PU-I and PU-Y).

Finally, let us discuss the hard-domain loss during the tensile test for those materials that both contain hard domains, and simultaneously appear to fulfill the condition

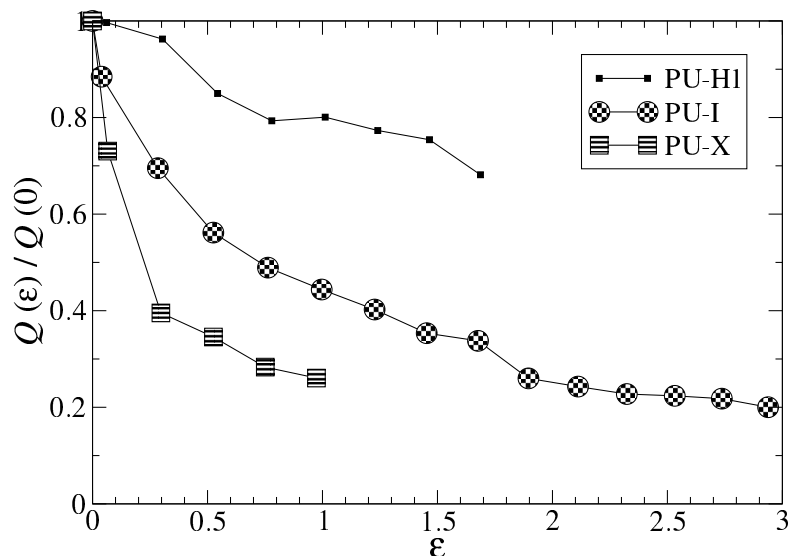


Figure 4.3.9: The materials with hard domains and (nearly) constant soft-phase density. Relative decrease of the invariant Q during the tensile test as a function of ϵ . The symbol hatching indicates uncorrelated domains, 3D correlation, and 1D correlation

$\rho_s \approx const.$ in the tensile experiment. Figure 4.3.9 presents the relative changes of the respective invariants, $Q(\epsilon)/Q(0)$. Assuming that the soft-domain density is not decreasing in an already nicely performing material, $v_h(\epsilon)$ can be determined essentially from these data. If, moreover, $v_h < 0.3$ then already $Q(\epsilon)/Q(0) \approx v_h(\epsilon)/v_h(0)$ approximates the fraction of remnant hard domains quite well. Application of this approximation demonstrates that PU-I and PU-X can lose nearly 80% of their hard domains without macroscopic failure.

4.3.7 Polyol Architecture and Microstructure

A series of propylene oxide polyether polyols has been produced with different molecular weights and topologies. The polyol for making PU-I is standard polypropylene glycol (PPG 2000) with $f = 2$ and $M_{th} = 2000$ g/mol. The polyol for producing PU-Hs has a PPG 2000 backbone, but is bifurcated at both ends. Because of this bifurcation M_{th} has increased somewhat, but M_e has been reduced by a factor of 2. The polyols for making PU-Y, PU-X and PU-HI have nominally the same M_e as PPG 2000, but their M_{th} are higher because they have a higher functionality (3, 4 and 4 respectively). PUEs have been produced from these polyols using BD as a chain extender and the MDI as an isocyanate at a constant hard segment content of about 30 wt%. Propylene oxide polyether polyols are non-crystallizing polyols. Therefore PUEs produced from such polyols are, compared to PUEs produced from crystallizing polyols like some polyesterols, relatively poor in mechanical properties. To compensate for this drawback these polyols

4.3 Failure Mechanisms of Crosslinked PUE with Poorly Developed Domain Structure

are often branched, the most common functionality being $f = 3$. The polyols with $f = 4$ have been produced for scientific interest. The PUE produced from PPG 2000 (PU-I) is linear in nature and is in that respect similar to the TPUs that have been studied previously[60, 61]. The other PUEs all are thermosets as they are chemically cross-linked. Because of the non-crystallizing nature of the soft segments and the relatively low HSC these PUEs are relatively soft. In such soft polymers the presence of a covalent polymer network through the use of branched polyols has a strong impact on the tensile behavior, as crosslinking reduces the extensibility of the polymer chains. During the PUE synthesis phase separation sets in when the solubility of hard blocks has fallen below the solubility limit in the reacting liquid. Hard domains are formed. The formation process is dependent on the chain mobility and therefore dependent on the nature and topology of the polyol. An increase in functionality and a decrease in molecular weight of the polyol delay the onset of phase segregation, which in turn may decrease the final phase separation and reduce the size and stability of the hard domains. The basic scattering profiles $\{I\}_1(s_3)$ at zero strain (Figure 4.3.6) show clearly that the overall extent to which phase separation has occurred is dependent on the type of polyol employed to produce the PUE. The most dramatic observation is that bifurcation of the basic PPG 2000 backbone (in PU-Hs), generates a material that is largely phase mixed as it shows neither discrete SAXS nor particle scattering. Due to its high f and low M_e (cf. Table 3.2) phase separation appears largely suppressed.

Of the 5 PUEs only PU-Y (Figure 4.3.6b) shows a clear scattering maximum and a relatively high level of overall scattering, indicating high levels of phase separation and periodicity. PU-I (Figure 4.3.6a) shows a similar scattering intensity as PU-Y, but a clear maximum is lacking which indicates that the arrangement is less perfect. PU-X and PU-HI (Figure 4.3.6c and d, respectively) show less scattering than PU-I and PU-Y, indicating increased phase mixing and poor domain formation. A tentative explanation could be that first the phase mixing effect of increased functionality from 2 to 3 is overridden by the increased molecular weight (from 2000 to 4000), but at a further increase in functionality (from 3 to 4) the extensive cross-linking during the synthesis restricts reptation and molecular motion required for microphase separation.

4.3.8 Conclusion

Notions concerning the morphological deformation and failure mechanisms in poorly structured polyurethane elastomers have been stimulated by our study. This is due to a combination of a suitable high flux (wiggler) SAXS beamline, a suitable set of materials, and an analysis that combines pattern interpretation, a CDF analysis, and the quantitative analysis of projections. Limitations originate from the physical and electronic constraints of the detector[248], which does not match the high photon flux of 3rd generation storage rings. With a modern PILATUS-1M detector it would have even been possible to approach industrially relevant strain rates.

As we proceed beyond an interpretation of the scattering patterns and exploit the potential of the SAXS theory, the microstructure information becomes more detailed. During our evaluation the idea of a nearly homogeneous morphology has been superseded

4 Results and Discussion

by the notion of a heterogeneous structure with interacting components. In this view good mechanical performance is no longer directly related to high stability[6] of the hard domains. Instead, a complex dynamic principle may become important: Pay attention to a changing number of components and balance their interactions.

The present series of PUE is based on the same monomers, but the polyol architecture varies drastically. The polyols are linear (I), Y- X- and H-shaped and the molecular weight and equivalent weight M_e have been varied independently. The I-shaped polyol gives an essential linear PUE that is thermoplastic, all other polyols result in thermoset PUEs. The polymer morphology and its changes upon strain on a nano-scale have been studied by SAXS measurements. In this work only one mechanical property has been considered: the elongation at break ε_b . We have shown that the developed polymer morphology and the deformation of the hard domains under stress strongly depend on the type of polyol employed. The strongest phase separation has been obtained for PU-I and PU-Y. Increasing the functionality of the polyol to 4 results in increased phase mixing (PU-X and PU-H). This has been attributed to a combined effect of functionality and molecular weight of the polyol and its effect on the phase separation process during the synthesis of the PUE. In the tensile tests in the polymer morphology on a nano-scale has also been found to strongly depend on the employed polyol. Here the dominant reason appears to be the variation of the network topologies. Of course, the question as to which polyol structure is the best for PUE applications, cannot be answered on the basis of this study because the requirements are different and numerous PUE recipes can be derived from the presented polyols. Nevertheless, it seems that the overall level of phase separation and the maintenance of this phase separated structure under stress is the highest for the PUEs produced from the I- and Y-shaped polyols. Therefore it appears not surprising that the most commonly employed propylene oxide polyether polyols in the technology to produce PUEs are polyols with a functionality of 2 and 3.

5 Summary and Outlook

The morphology of polyurethane is regulated by the phase separation. Some polyurethanes are poorly phase-separated, their scattering intensity at small angle is weak. For most of polyurethanes, the SAXS pattern under strain is not two-perfect-spot pattern on the meridian, this feature reflects the correlation of hard domains not only in the meridional directions but also in the oblique directions. The multi-dimensional CDF can show the correlation of hard domains in the meridional and oblique directions simultaneously. The 3D network-like hard phase can only be indicated by the discrete six-spot on the CDF. Not all the hard domains form the microfibrils with hard domains stacking along the elongation direction under strain, some hard domains are only correlated in the oblique directions even under high strain.

Owing to the combination of newly developed high-flux X-ray beamline and advanced two-dimensional data processing method, deeper insight into the relationship of structure-and-property of polyurethane elastomer is gained. The high-flux beamline enables us to collect SAXS pattern with high signal-to-noise ratio in a short time and to track the dynamic morphological evolution. The advanced data evaluation method CDF facilitates intuitively presenting the nanostructure in real space.

These advancements move the investigation of structure-and-property of polyurethane forward. Based on the advancements of hardware and software, some features of nanostructure evolution under strain are acquired.

- Tracking the variation of relative volume fraction of hard domains under strain of hand casting polyurethanes with different chemical compositions is performed by fitting of IDF which is computed from the Bonart's longitudinal projection. An empirical relationship of destruction quantity of hard domains and macroscopic elongation of polyurethanes is established. This equation links the nanostructure and macroscopic strain.
- Ageing effects on the nanostructure evolution under strain of a machine casting polyurethane aged at 150 °C for different time is studied. With increasing the ageing time, the content of hard phase decreases significantly, the hard segments and soft segments are mixing as the chemical degradation, the heterogeneity on the nanoscale becomes less distinct.
- Nanostructure evolution under strain of crosslinked polyurethanes with different polyol topologies is studied. All the polyols are based on the same monomers, but the architecture varies drastically. The polyols are linear (I), Y-, X-, and H-shaped. Only the PUE of I-shaped polyols exhibits thermoplastic, all the other PUEs with multiple arms exhibit thermoset.

5 Summary and Outlook

- PUEs of I- and Y-shaped polyols show the strongest phase separation. Increasing the functionality of polyol to 4 leads to poor phase separation. PUEs of I- and Y-shaped have the highest level of macroscopic elongation of materials under stress that is achieved by sacrifice of hard domains. The polyols with a functionality of 2 and 3 are most commonly employed to produce the commercial PUEs.
- In the hand-cast polyurethanes, most of the hard domains are placed in the soft matrix at random. Only a few hard domains are correlated. The domain sizes distribution of hard and soft domains are broad. The domain stacking can be described by the one-dimensional stacking model. In the machine-cast polyurethanes, the materials show better order than the hand-cast materials, the hard domains can be described by the combination model of duo and solo. Duo means two correlated hard domains. Solo means the isolated hard domains.

Outlook.

- We have only studied materials with a HSC=51%wt. However we do not know if the tensile domain consumption $c_{r,\varepsilon}$ is a function of HSC. A systematic variation of HSC will be investigated in the future. It should give information about whether one should normalize the initial value of the curves in Figure 4.1.15 instead of on 1 on HSC. The latter would be reasonable, if an absolute hard-domain consumption, $c_h = \text{HSC} c_{r,h}$, would turn out to be a characteristic parameter of the material.
- How the ageing effects of the other environments, e.g. high-energy radiation or moisture, affect the properties of PUEs should be studied.
- Variation of crosslinked morphology is only altered by architecture of polyols, we are also interested in the materials whose hard segments are crosslinked. It's also possible to alter the architecture of isocyanates and chain extenders, e.g. the tri- and quadri-isocyanate. How the crosslinked hard segments affect material properties should be investigated in the future.

Methodological Advancements. Methodological advancements to inspect more on the morphological variation should be planned in the future.

- It is reasonable to drive such experiments to the vicinity of the elongation at break. This requires some technical improvements concerning the synchrotron beamline (X-ray beam of higher intensity but still large diameter, very advanced detector) and the tensile tester (use of self-tightening grips).
- Combination of in-situ FTIR and straining of PUEs should be performed in the future as well. A quantitative analysis of failure-content of hard domains should be fitted from the absorbance peaks of FTIR curve. The numeric relationship of hard domain failure-content and elongation of material should be estimated as well.
- How to determine the absolute volume fraction of hard phase from the scattering power is also planned in the future.

- How the morphologies evolve at high straining rate is also our interests. Thus combination of a tensile machine with the high straining rate and beamline with high-flux and fast-readout detector is the hardware that can support our interests.
- How the morphologies fatigue in the oscillating straining is also planned. To hit this target, pre-strain should be well-designed. How the volume fraction of hard phase evolves in the fatigue process is our interest.

Bibliography

- [1] Bonart, R., *J. Macromol. Sci. Part B* 1968, 2, 115–138.
- [2] Bonart, R.; Morbitzer, L.; Hentze, G., *J. Macromol. Sci. Part B* 1969, 3, 337–356.
- [3] Bonart, R.; Müller, E. H., *J. Macromol. Sci. Part B* 1974, 10, 345–357.
- [4] Bonart, R.; Müller, E. H., *J. Macromol. Sci. Part B* 1974, 10, 177–189.
- [5] Stribeck, N., *J. Appl. Crystallogr.* 2001, 34, 496–503.
- [6] Bonart, R., *Angew. Makromol. Chemie* 1977, 58, 259–297.
- [7] Petrović, Z. S.; Ferguson, J., *Prog. Polym. Sci.* 1991, 16, 695–836.
- [8] Prisacariu, C., *Polyurethane Elastomers From Morphology to Mechanical Aspects*, Springer Vienna, Vienna, 2011.
- [9] Seymour, R. W.; Cooper, S. L., *Macromolecules* 1973, 6, 48–53.
- [10] Delebecq, E.; Pascault, J.-P.; Boutevin, B.; Ganachaud, F., *Chem. Rev.* 2013, 113, 80–118.
- [11] Sami, S.; Yildirim, E.; Yurtsever, M.; Yurtsever, E.; Yilgor, E.; Yilgor, I.; Wilkes, G. L., *Polymer*. 2014, 55, 4563–4576.
- [12] Leung, L. M.; Koberstein, J. T., *J. Polym. Sci. Polym. Phys. Ed.* 1985, 23, 1883–1913.
- [13] Leung, L. M.; Koberstein, J. T., *Macromolecules* 1986, 19, 706–713.
- [14] Koberstein, J. T.; Galambos, A. F.; Leung, L. M., *Macromolecules* 1992, 25, 6195–6204.
- [15] Koberstein, J. T.; Leung, L. M., *Macromolecules* 1992, 25, 6205–6213.
- [16] Pompe, G.; Pohlers, A.; Pötschke, P.; Pionteck, J., *Polymer*. 1998, 39, 5147–5153.
- [17] Versteegen, R. M.; Sijbesma, R. P.; Meijer, E. W., *Macromolecules* 2005, 38, 3176–3184.
- [18] Buckley, C.; Prisacariu, C.; Martin, C., *Polymer*. 2010, 51, 3213–3224.
- [19] Piril Ertem, S.; Yilgor, E.; Kosak, C.; Wilkes, G. L.; Zhang, M.; Yilgor, I., *Polymer*. 2012, 53, 4614–4622.
- [20] Caracciolo, P. C.; Buffa, F.; Abraham, G. A., *J. Mater. Sci. Mater. Med.* 2009, 20, 145–55.
- [21] Burattini, S.; Greenland, B. W.; Merino, D. H.; Weng, W.; Seppala, J.; Colquhoun, H. M.; Hayes, W.; Mackay, M. E.; Hamley, I. W.; Rowan, S. J., *J. Am. Chem. Soc.* 2010, 132, 12051–8.

Bibliography

- [22] Zhang, C.; Hu, J.; Chen, S.; Ji, F., *J. Mol. Model.* 2010, 16, 1391–9.
- [23] Clough, S. B.; Schneider, N. S.; King, A. O., *J. Macromol. Sci. Part B* 1968, 2, 641–648.
- [24] Koutsky, J. A.; Hien, N. V.; Cooper, S. L., *J. Polym. Sci. Part B Polym. Lett.* 1970, 8, 353–359.
- [25] Abouzahr, S.; Wilkes, G.; Ophir, Z., *Polymer.* 1982, 23, 1077–1086.
- [26] Abouzahr, S.; Wilkes, G. L., *J. Appl. Polym. Sci.* 1984, 29, 2695–2711.
- [27] Speckhard, T. A.; Strate, G. V.; Gibson, P. E.; Cooper, S. L., *Polym. Eng. Sci.* 1983, 23, 337–349.
- [28] Speckhard, T.; Hwang, K.; Cooper, S.; Chang, V.; Kennedy, J., *Polymer.* 1985, 26, 70–78.
- [29] Speckhard, T.; Gibson, P.; Cooper, S.; Chang, V.; Kennedy, J., *Polymer.* 1985, 26, 55–69.
- [30] Speckhard, T. A.; Cooper, S. L., *Rubber Chem. Technol.* 1986, 59, 405–431.
- [31] Martin, D. J.; Meijs, G. F.; Gunatillake, P. A.; Yozghatlian, S. P.; Renwick, G. M., *J. Appl. Polym. Sci.* 1999, 71, 937–952.
- [32] Laity, P. R.; Taylor, J. E.; Wong, S. S.; Khunkamchoo, P.; Norris, K.; Cable, M.; Chohan, V.; Andrews, G. T.; Johnson, A. F.; Cameron, R. E., *J. Macromol. Sci. Part B* 2005, 43, 95–124.
- [33] Aneja, A.; Wilkes, G. L., *Polymer.* 2003, 44, 7221–7228.
- [34] McLean, R. S.; Sauer, B. B., *Macromolecules* 1997, 30, 8314–8317.
- [35] Yanagihara, Y.; Osaka, N.; Murayama, S.; Saito, H., *Polymer.* 2013, 54, 2183–2189.
- [36] Saiani, A.; Rochas, C.; Eeckhaut, G.; Daunch, W. A.; Leenslag, J.-W.; Higgins, J. S., *Macromolecules* 2004, 37, 1411–1421.
- [37] Shilov, V. V.; Lipatov, Y. S.; Karabanova, L. V.; Sergeeva, L. M., *J. Polym. Sci. Polym. Chem. Ed.* 1979, 17, 3083–3093.
- [38] Neff, R.; Adedeji, A.; Macosko, C. W.; Ryan, A. J., *J. Polym. Sci. Part B Polym. Phys.* 1998, 36, 573–581.
- [39] Rinaldi, R. G.; Boyce, M. C.; Weigand, S. J.; Londono, D. J.; Guise, M. W., *J. Polym. Sci. Part B Polym. Phys.* 2011, 49, 1660–1671.
- [40] D'hollander, S.; Gommès, C. J.; Mens, R.; Adriaensens, P.; Goderis, B.; Du Prez, F., *J. Mater. Chem.* 2010, 20, 3475.
- [41] Qi, H.; Boyce, M., *Mech. Mater.* 2005, 37, 817–839.
- [42] Song, Y. M.; Chen, W. C.; Yu, T. L.; Linliu, K.; Tseng, Y. H., *J. Appl. Polym. Sci.* 1996, 62, 827–834.
- [43] Javni, I.; Zhang, W.; Petrović, Z. S., *J. Appl. Polym. Sci.* 2003, 88, 2912–2916.
- [44] Sekkar, V.; Gopalakrishnan, S.; Ambika Devi, K., *Eur. Polym. J.* 2003, 39, 1281–1290.
- [45] Hourston, D. J.; Williams, G.; Satguru, R.; Padget, J. D.; Pears, D., *J. Appl. Polym. Sci.* 1997, 66, 2035–2044.
- [46] Donnelly, M. J., *Polym. Int.* 1995, 37, 297–314.

- [47] Petrović, Z. S.; Guo, A.; Zhang, W., *J. Polym. Sci. Part A Polym. Chem.* 2000, 38, 4062–4069.
- [48] Blackwell, J.; Nagarajan, M.; Hoitink, T., *Polymer*. 1982, 23, 950–956.
- [49] Blackwell, J.; Lee, C. D., *J. Polym. Sci. Polym. Phys. Ed.* 1983, 21, 2169–2180.
- [50] Blackwell, J.; Lee, C. D., *J. Polym. Sci. Polym. Phys. Ed.* 1984, 22, 759–772.
- [51] Prisacariu, C.; Buckley, C.; Caraculacu, A., *Polymer*. 2005, 46, 3884–3894.
- [52] Lai, Y.-C.; Quinn, E. T.; Valint, P. L., *J. Polym. Sci. Part A Polym. Chem.* 1995, 33, 1767–1772.
- [53] Harpen, F. L. G. E. B., *11th Int. Workshop on Polymer Reaction Engineering. Book of Abstracts*, Tech. rep., 2013.
- [54] Rausch, K. W.; Sayigh, A. A. R., *Ind. Eng. Chem. Prod. Res. Dev.* 1965, 4, 92–98.
- [55] Yen, M.-S.; Kuo, S.-C., *J. Appl. Polym. Sci.* 1996, 61, 1639–1647.
- [56] Fan, L. H.; Hu, C. P.; Ying, S. K., *Polym. Eng. Sci.* 1997, 37, 338–345.
- [57] Bell, J. P., *J. Appl. Polym. Sci.* 1982, 27, 3503–3511.
- [58] Stribeck, A.; Jokari-Sheshdeh, F.; Pösel, E.; Eling, B.; in't Veld, P. J.; Goerigk, G. J.; Hoell, A., *J. Polym. Sci. Part B Polym. Phys.* 2015, 53, 1213–1223.
- [59] Van Bogart, J. W. C.; Gibson, P. E.; Cooper, S. L., *J. Polym. Sci. Polym. Phys. Ed.* 1983, 21, 65–95.
- [60] Stribeck, N.; Zeinolebadi, A.; Sari, M. G.; Frick, A.; Mikoszek, M.; Botta, S., *Macromol. Chem. Phys.* 2011, 212, 2234–2248.
- [61] Stribeck, N.; Zeinolebadi, A.; Harpen, F.; Luinstra, G.; Eling, B.; Botta, S., *Macromolecules* 2013, 46, 4041–4052.
- [62] Li, C.; Cooper, S., *Polymer*. 1990, 31, 3–7.
- [63] Li, C.; Goodman, S. L.; Albrecht, R. M.; Cooper, S. L., *Macromolecules* 1988, 21, 2367–2375.
- [64] Koberstein, J. T.; Stein, R. S., *J. Polym. Sci. Polym. Phys. Ed.* 1983, 21, 2181–2200.
- [65] Laity, P. R.; Taylor, J. E.; Wong, S. S.; Khunkamchoo, P.; Norris, K.; Cable, M.; Andrews, G. T.; Johnson, A. F.; Cameron, R. E., *Polymer*. 2004, 45, 5215–5232.
- [66] Sheth, J. P.; Aneja, A.; Wilkes, G. L., *Polymer*. 2004, 45, 5979–5984.
- [67] Sheth, J. P.; Klinedinst, D. B.; Wilkes, G. L.; Yilgor, I.; Yilgor, E., *Polymer*. 2005, 46, 7317–7322.
- [68] Yilgor, I.; Yilgor, E., *Polym. Rev.* 2007, 47, 487–510.
- [69] Das, S.; Cox, D. F.; Wilkes, G. L.; Klinedinst, D. B.; Yilgor, I.; Yilgor, E.; Beyer, F. L., *J. Macromol. Sci. Part B Phys.* 2007.
- [70] De, D.; Gaymans, R. J., *Macromol. Mater. Eng.* 2008, 293, 887–894.
- [71] De, D.; Gaymans, R. J., *Macromol. Mater. Eng.* 2009, 294, 405–413.
- [72] Castagna, A. M.; Pangon, A.; Choi, T.; Dillon, G. P.; Runt, J., *Macromolecules* 2012, 45, 8438–8444.

Bibliography

- [73] Tan, D.; Zhang, X.; Li, J.; Tan, H.; Fu, Q., *J. Biomed. Mater. Res. A* 2012, 100, 380–7.
- [74] Castagna, A. M.; Pangon, A.; Dillon, G. P.; Runt, J., *Macromolecules* 2013, 46, 6520–6527.
- [75] Odarchenko, Y. I.; Sijbrandi, N. J.; Rosenthal, M.; Kimenai, A. J.; Mes, E. P. C.; Broos, R.; Bar, G.; Dijkstra, P. J.; Feijen, J.; Ivanov, D. A., *Acta Biomater.* 2013, 9, 6143–9.
- [76] Chang, Z.; Zhang, M.; Hudson, A. G.; Orlor, E. B.; Moore, R. B.; Wilkes, G. L.; Turner, S. R., *Polymer.* 2013, 54, 6910–6917.
- [77] He, Y.; Zhang, X.; Runt, J., *Polymer.* 2014, 55, 906–913.
- [78] He, Y.; Xie, D.; Zhang, X., *J. Mater. Sci.* 2014, 49, 7339–7352.
- [79] Kaushiva, B.; Wilkes, G., *Polymer.* 2000, 41, 6987–6991.
- [80] Blackwell, J.; Ross, M., *J. Polym. Sci. Polym. Lett. Ed.* 1979, 17, 447–451.
- [81] Blackwell, J.; Gardner, K. H., *Polymer.* 1979, 20, 13–17.
- [82] Blackwell, J.; Nagarajan, M.; Hoitink, T., *Polymer.* 1981, 22, 1534–1539.
- [83] Christenson, C. P.; Harthcock, M. A.; Meadows, M. D.; Spell, H. L.; Howard, W. L.; Creswick, M. W.; Guerra, R. E.; Turner, R. B., *J. Polym. Sci. Part B Polym. Phys.* 1986, 24, 1401–1439.
- [84] Quay, J.; Sun, Z.; Blackwell, J.; Briber, R.; Thomas, E., *Polymer.* 1990, 31, 1003–1008.
- [85] Clough, S. B.; Schneider, N. S., *J. Macromol. Sci. Part B* 1968, 2, 553–566.
- [86] Briber, R. M.; Thomas, E. L., *J. Macromol. Sci. Part B* 2006, 22, 509–528.
- [87] Blundell, D. J.; Eeckhaut, G.; Fuller, W.; Mahendrasingam, A.; Martin, C., *Polymer.* 2002, 43, 5197–5207.
- [88] Blundell, D. J.; Eeckhaut, G.; Fuller, W.; Mahendrasingam, A.; Martin, C., *J. Macromol. Sci. Part B* 2004, 43, 125–142.
- [89] Laity, P. R.; Taylor, J. E.; Wong, S. S.; Khunkamchoo, P.; Norris, K.; Cable, M.; Andrews, G. T.; Johnson, A. F.; Cameron, R. E., *Polymer.* 2004, 45, 7273–7291.
- [90] Yilgör, I.; Yilgör, E.; Wilkes, G. L., *Polymer.* 2015, 58, A1–A36.
- [91] Bonart, R.; Morbitzer, L.; Müller, E. H., *J. Macromol. Sci. Part B* 1974, 9, 447–461.
- [92] Bonart, R.; Müller-Riederer, G., *Colloid Polym. Sci.* 1981, 259, 926–936.
- [93] Meyer, H.; Bonart, R., *Frontiers in Polymer Science*, vol. 71 of *Progress in Colloid & Polymer Science*, Steinkopff, Darmstadt, 1985.
- [94] Bonart, R.; Bötzel, F.; Schmid, J., *Makro Chem* 1987, 188, 907–919.
- [95] Schneider, N. S.; Desper, C. R.; Illinger, J. L.; King, A. O.; Barr, D., *J. Macromol. Sci. Part B* 1975, 11, 527–552.
- [96] Desper, C. R.; Schneider, N. S.; Jasinski, J. P.; Lin, J. S., *Macromolecules* 1985, 18, 2755–2761.
- [97] Cooper, S. L.; Tobolsky, A. V., *J. Appl. Polym. Sci.* 1966, 10, 1837–1844.
- [98] Seymour, R. W.; Estes, G. M.; Cooper, S. L., *Macromolecules* 1970, 3, 579–583.

- [99] Estes, G. M.; Seymour, R. W.; Cooper, S. L., *Macromolecules* 1971, 4, 452–457.
- [100] ALLEGREZZAJR, A.; SEYMOUR, R.; NG, H.; COOPER, S., *Polymer*. 1974, 15, 433–440.
- [101] Lin, S. B.; Hwang, K. S.; Tsay, S. Y.; Cooper, S. L., *Colloid Polym. Sci.* 1985, 263, 128–140.
- [102] Moreland, J. C.; Wilkes, G. L.; Turner, R. B., *J. Appl. Polym. Sci.* 1991, 43, 801–815.
- [103] Hernandez, R.; Weksler, J.; Padsalgikar, A.; Choi, T.; Angelo, E.; Lin, J. S.; Xu, L.-C.; Siedlecki, C. A.; Runt, J., *Macromolecules* 2008, 41, 9767–9776.
- [104] Pathak, J. A.; Twigg, J. N.; Nugent, K. E.; Ho, D. L.; Lin, E. K.; Mott, P. H.; Robertson, C. G.; Vukmir, M. K.; Epps, T. H.; Roland, C. M., *Macromolecules* 2008, 41, 7543–7548.
- [105] Tereshatov, V. V.; Makarova, M. A.; Senichev, V. Y.; Slobodinyuk, A. I., *Colloid Polym. Sci.* 2012, 290, 641–651.
- [106] Tereshatov, V. V.; Makarova, M. A.; Senichev, V. Y.; Volkova, E. R.; Vnutskikh, Z. A.; Slobodinyuk, A. I., *Colloid Polym. Sci.* 2014, 293, 153–164.
- [107] Lee, H. S.; Hsu, S. L., *J. Polym. Sci. Part B Polym. Phys.* 1994, 32, 2085–2098.
- [108] Lee, H. S.; Ra Yoo, S.; Won Seo, S., *J. Polym. Sci. Part B Polym. Phys.* 1999, 37, 3233–3245.
- [109] Reynolds, N.; Spiess, H. W.; Hayen, H.; Nefzger, H.; Eisenbach, C. D., *Macromol. Chem. Phys.* 1994, 195, 2855–2873.
- [110] Fu, B.; Hsiao, B.; Pagola, S.; Stephens, P.; White, H.; Rafailovich, M.; Sokolov, J.; Mather, P.; Jeon, H.; Phillips, S.; Lichtenhan, J.; Schwab, J., *Structural development during deformation of polyurethane containing polyhedral oligomeric silsesquioxanes (POSS) molecules*, 2001.
- [111] Christenson, E. M.; Anderson, J. M.; Hiltner, A.; Baer, E., *Polymer*. 2005, 46, 11744–11754.
- [112] Enderle, H. F.; Kilian, H. G.; Heise, B.; Mayer, J.; Hesse, H., *Colloid Polym. Sci.* 1986, 264, 305–322.
- [113] Martin, D. J.; Meijs, G. F.; Gunatillake, P. A.; McCarthy, S. J.; Renwick, G. M., *J. Appl. Polym. Sci.* 1997, 64, 803–817.
- [114] Chu, B.; Gao, T.; Li, Y.; Wang, J.; Desper, C. R.; Byrne, C. A., *Macromolecules* 1992, 25, 5724–5729.
- [115] Eceiza, A.; Martin, M.; de la Caba, K.; Kortaberria, G.; Gabilondo, N.; Corcuera, M.; Mondragon, I., *Polym. Eng. Sci.* 2008, 48, 297–306.
- [116] Miyano, W.; Inoue, E.; Tsuchiya, M.; Ishimaru, K.; Kojima, T., *J. Therm. Anal. Calorim.* 2001, 64, 459–465.
- [117] *Polytetrahydrofuran*, <http://en.wikipedia.org/wiki/Polytetrahydrofuran>.
- [118] Liu, L.-Z.; Yeh, F.; Chu, B., *Macromolecules* 1996, 29, 5336–5345.
- [119] Schubert, M. A.; Wiggins, M. J.; Anderson, J. M.; Hiltner, A., *J. Biomed. Mater. Res.* 1997, 35, 319–28.
- [120] Curgul, S.; Yilgor, I.; Yilgor, E.; Erman, B.; Cakmak, M., *Macromolecules* 2004, 37, 8676–8685.
- [121] Koerner, H.; Kelley, J. J.; Vaia, R. A., *Macromolecules* 2008, 41, 4709–4716.

Bibliography

- [122] Waletzko, R. S.; Korley, L. T. J.; Pate, B. D.; Thomas, E. L.; Hammond, P. T., *Macromolecules* 2009, 42, 2041–2053.
- [123] Laviolette, M.; Auger, M.; Désilets, S., *Macromolecules* 1999, 32, 1602–1610.
- [124] Boubakri, A.; Elleuch, K.; Guermazi, N.; Ayedi, H., *Mater. Des.* 2009, 30, 3958–3965.
- [125] Boubakri, A.; Haddar, N.; Elleuch, K.; Bienvenu, Y., *Mater. Des.* 2010, 31, 4194–4201.
- [126] Gorna, K.; Gogolewski, S., *Polym. Degrad. Stab.* 2003, 79, 465–474.
- [127] Dannoux, A.; Esnouf, S.; Amekraz, B.; Dauvois, V.; Moulin, C., *J. Polym. Sci. Part B Polym. Phys.* 2008, 46, 861–878.
- [128] Rosu, D.; Rosu, L.; Cascaval, C. N., *Polym. Degrad. Stab.* 2009, 94, 591–596.
- [129] Boubakri, A.; Haddar, N.; Elleuch, K.; Bienvenu, Y., *Comptes Rendus Mécanique* 2011, 339, 666–673.
- [130] Chaffin, K. A.; Buckalew, A. J.; Schley, J. L.; Chen, X.; Jolly, M.; Alkatout, J. A.; Miller, J. P.; Untereker, D. F.; Hillmyer, M. A.; Bates, F. S., *Macromolecules* 2012, 45, 9110–9120.
- [131] Padsalgikar, A.; Cosgriff-Hernandez, E.; Gallagher, G.; Touchet, T.; Iacob, C.; Mellin, L.; Norlin-Weissenrieder, A.; Runt, J., *J. Biomed. Mater. Res. Part B Appl. Biomater.* 2015, 103, 159–168.
- [132] Chaffin, K. A.; Chen, X.; McNamara, L.; Bates, F. S.; Hillmyer, M. A., *Macromolecules* 2014, 47, 5220–5226.
- [133] Aou, K.; Ge, S.; Mowery, D. M.; Zeigler, R. C.; Gamboa, R. R., *Polymer*. 2015, 56, 37–45.
- [134] Chattopadhyay, D.; Webster, D. C., *Prog. Polym. Sci.* 2009, 34, 1068–1133.
- [135] Gunatillake, P. A.; Martin, D. J.; Meijs, G. F.; McCarthy, S. J.; Adhikari, R., *Aust. J. Chem.* 2003, 56, 545.
- [136] Levchik, S. V.; Weil, E. D., *Polym. Int.* 2004, 53, 1585–1610.
- [137] Kazmierczak, M. E.; Fornes, R. E.; Buchanan, D. R.; Gilbert, R. D., *J. Polym. Sci. Part B Polym. Phys.* 1989, 27, 2189–2202.
- [138] Percus, J. K.; Yevick, G. J., *Phys. Rev.* 1958, 110, 1–13.
- [139] Tang, Q.; He, J.; Yang, R.; Ai, Q., *J. Appl. Polym. Sci.* 2013, 128, 2152–2161.
- [140] Gibson, P. E.; Van Bogart, J. W. C.; Cooper, S. L., *J. Polym. Sci. Part B Polym. Phys.* 1986, 24, 885–907.
- [141] Debye, P.; Bueche, A. M., *J. Appl. Phys.* 1949, 20, 518–525.
- [142] Huitron-Rattinger, E.; Ishida, K.; Romo-Uribe, A.; Mather, P. T., *Polymer*. 2013, 54, 3350–3362.
- [143] Madkour, T. M.; Mohamed, S. K., *J. Appl. Crystallogr.* 2013, 46, 980–992.
- [144] Tian, Q.; Almásy, L.; Yan, G.; Sun, G.; Zhou, X.; Liu, J.; Krakovsky, I.; Veres, M.; Rosta, L.; Chen, B., *Express Polym. Lett.* 2014, 8, 345–351.
- [145] Awad, W. H.; Wilkie, C. A., *Polymer*. 2010, 51, 2277–2285.

- [146] Sui, H.; Ju, X.; Liu, X.; Cheng, K.; Luo, Y.; Zhong, F., *Polym. Degrad. Stab.* 2014, 101, 109–113.
- [147] Li, Y.; Gao, T.; Liu, J.; Linliu, K.; Desper, C. R.; Chu, B., *Macromolecules* 1992, 25, 7365–7372.
- [148] Saiani, A.; Novak, A.; Rodier, L.; Eeckhaut, G.; Leenslag, J.-W.; Higgins, J. S., *Macromolecules* 2007, 40, 7252–7262.
- [149] Mang, J. T.; Peterson, P. D.; Orlor, E. B.; Wroblewski, D. A.; Langlois, D. A.; Espada, L. I.; Hjelm, R. P., *Neutron News* 2003, 14, 26–28.
- [150] Beachell, H. C.; Son, C. P. N., *J. Appl. Polym. Sci.* 1963, 7, 2217–2237.
- [151] Bruckmoser, K.; Resch, K., *Macromol. Symp.* 2014, 339, 70–83.
- [152] Yang, W.; Macosko, C.; Wellinghoff, S., *Polymer*. 1986, 27, 1235–1240.
- [153] Tatai, L.; Moore, T. G.; Adhikari, R.; Malherbe, F.; Jayasekara, R.; Griffiths, I.; Gunatillake, P. A., *Biomaterials* 2007, 28, 5407–17.
- [154] Servay, T.; Voelkel, R.; Schmiedberger, H.; Lehmann, S., *Polymer*. 2000, 41, 5247–5256.
- [155] Hu, W.; Koberstein, J. T., *J. Polym. Sci. Part B Polym. Phys.* 1994, 32, 437–446.
- [156] Christenson, E. M.; Anderson, J. M.; Hiltner, A., *J. Biomed. Mater. Res.* 2004, 70A, 245–255.
- [157] Chuang, F., *Polym. Degrad. Stab.* 2007, 92, 1393–1407.
- [158] Schömer, M.; Seiwert, J.; Frey, H., *ACS Macro Lett.* 2012, 1, 888–891.
- [159] Güney, A.; Hasirci, N., *J. Appl. Polym. Sci.* 2014, 131, n/a–n/a.
- [160] Mingjie, H.; Wei, F.; Le, G.; Weibing, W.; Xinghai, L.; Chi, H., *Polym. Bull.* 2014, 71, 2671–2693.
- [161] Killis, A.; LeNest, J. F.; Gandini, A.; Cheradame, H., *J. Polym. Sci. Polym. Phys. Ed.* 1981, 19, 1073–1080.
- [162] Fayolle, B.; Gilormini, P.; Diani, J., *Colloid Polym. Sci.* 2009, 288, 97–103.
- [163] Cristiano, A.; Marcellan, A.; Keestra, B. J.; Steeman, P.; Creton, C., *J. Polym. Sci. Part B Polym. Phys.* 2011, 49, 355–367.
- [164] Smith, T. L., *J. Polym. Sci. Polym. Phys. Ed.* 1974, 12, 1825–1848.
- [165] Klinedinst, D. B.; Yilgör, I.; Yilgör, E.; Zhang, M.; Wilkes, G. L., *Polymer*. 2012, 53, 5358–5366.
- [166] Balizer, E.; Fedderly, J.; Lee, G.; Bartyczak, S.; Mock, W., *Powder Diffr.* 2012, 26, 149–154.
- [167] Kimura, I.; Ishihara, H.; Ono, H.; Yoshihara, N.; Nomura, S.; Kawai, H., *Macromolecules* 1974, 7, 355–363.
- [168] Hoffmann, K.; Bonart, R., *Die Makromol. Chemie* 1983, 184, 1529–1546.
- [169] Wang, C. B.; Cooper, S. L., *Macromolecules* 1983, 16, 775–786.
- [170] Li, C.; Han, J.; Huang, Q.; Xu, H.; Tao, J.; Li, X., *Polymer*. 2012, 53, 1138–1147.
- [171] Petrovic, Z. S.; Javni, I.; Divjakovic, V., *J. Polym. Sci. Part B Polym. Phys.* 1998, 36, 221–235.
- [172] Zachmann, H., *Nucl. Instruments Methods Phys. Res. Sect. B Beam Interact. with Mater. Atoms* 1995, 97, 209–215.

Bibliography

- [173] Porod, G., *Colloid Polym. Sci.* 1951, 124, 83–114.
- [174] Debye, P.; Anderson, H. R.; Brumberger, H.; Anderson, J. H. R.; Brumberger, H., *J. Appl. Phys.* 1957, 28, 679–683.
- [175] Dijkstra, A.; Kortleve, G.; Vonk, C. G., *Colloid Polym. Sci.* 1966, 210, 121–123.
- [176] Vonk, C. G.; Kortleve, G., *Kolloid-Zeitschrift Zeitschrift für Polym.* 1967, 220, 19–24.
- [177] Kortleve, G.; Vonk, C. G., *Kolloid-Zeitschrift Zeitschrift für Polym.* 1968, 225, 124–131.
- [178] Vonk, C. G., *J. Appl. Crystallogr.* 1973, 6, 148–152.
- [179] Strobl, G. R.; Schneider, M., *J. Polym. Sci. Polym. Phys. Ed.* 1980, 18, 1343–1359.
- [180] Santa Cruz, C.; Stribeck, N.; Zachmann, H. G.; Balta Calleja, F. J., *Macromolecules* 1991, 24, 5980–5990.
- [181] Méring, J.; Tchoubar, D., *J. Appl. Crystallogr.* 1968, 1, 153–165.
- [182] Tchoubar, D.; Méring, J., *J. Appl. Crystallogr.* 1969, 2, 128–138.
- [183] Levitz, P.; Tchoubar, D., *J. Phys. I* 1992, 2, 771–790.
- [184] Ruland, W., *Colloid Polym. Sci.* 1977, 255, 417–427.
- [185] Ruland, W., *Colloid & Polym. Sci.* 1978, 256, 932–936.
- [186] Stribeck, N.; Ruland, W., *J. Appl. Crystallogr.* 1978, 11, 535–539.
- [187] Guinier, A.; Fournet, G., *Small-angle scattering of X-rays*, Wiley, 1955.
- [188] Guinier, A., *X-ray diffraction: in crystals, imperfect crystals, and amorphous bodies*, Courier Dover Publications, 1994.
- [189] Hosemann, R.; Bagchi, S. N., *Direct analysis of diffraction by matter*, North-Holland Pub. Co., 1962.
- [190] Balta-Calleja, F. J.; Vonk, C. G., *X-ray scattering of synthetic polymers*, Elsevier Amsterdam, 1989.
- [191] Glatter, O.; Kratky, O., *London, NY* 1982.
- [192] Feigin, L. A.; Svergun, D. I.; Taylor, G. W., *Structure analysis by small-angle X-ray and neutron scattering*, Springer, 1987.
- [193] Stribeck, N., *X-Ray Scattering of Soft Matter*, Springer, Heidelberg, 2007.
- [194] Strobl, G. R.; Schneider, M. J.; Voigt-Martin, I. G., *J. Polym. Sci. Polym. Phys. Ed.* 1980, 18, 1361–1381.
- [195] Hermans, J. J., *Recl. des Trav. Chim. des Pays-Bas* 1944, 63, 211–218.
- [196] Hosemann, R., *Zeitschrift Phys.* 1950, 127, 16–40.
- [197] Stribeck, N., *J. Appl. Crystallogr.* 2006, 39, 237–243.
- [198] Vonk, C. G., *Colloid Polym. Sci.* 1979, 257, 1021–1032.
- [199] Stribeck, N.; Nöchel, U.; Almendárez Camarillo, A.; Roth, S. V.; Dommach, M.; Bösecke, P., *Macromolecules* 2007, 40, 4535–4545.

- [200] Stribeck, N., *Colloid Polym. Sci.* 1993, 271, 1007–1023.
- [201] Förster, S.; Apostol, L.; Bras, W., *J. Appl. Crystallogr.* 2010, 43, 639–646.
- [202] Stribeck, N., *J. Phys. IV Proc.* 1993, 3, 507–510.
- [203] Stribeck, N.; Almendarez Camarillo, A.; Cunis, S.; Bayer, R. K.; Gehrke, R., *Macromol. Chem. Phys.* 2004, 205, 1445–1454.
- [204] Stribeck, N., *J. Polym. Sci. Part B Polym. Phys.* 1999, 37, 975–981.
- [205] Crist, B., *J. Macromol. Sci. Part B* 2000, 39, 493–518.
- [206] Crist, B., *J. Polym. Sci. Part B Polym. Phys.* 2001, 39, 2454–2460.
- [207] Crist, B., *Macromolecules* 2003, 36, 4880–4890.
- [208] Reinhold, C.; Fischer, E. W.; Peterlin, A., *J. Appl. Phys.* 1964, 35, 71.
- [209] Hall, I. H.; Mahmoud, E. A.; Carr, P. D.; Geng, Y. D., *Colloid Polym. Sci.* 1987, 265, 383–393.
- [210] Hanna, S.; Windle, A., *Polymer*. 1988, 29, 207–223.
- [211] Voigt-Martin, I. G.; Mandelkern, L., *J. Polym. Sci. Part B Polym. Phys.* 1989, 27, 967–991.
- [212] Stribeck, N., *Colloid & Polym. Sci.* 1989, 267, 301–310.
- [213] Stribeck, N.; Bosecke, P.; Polizzi, S., *Colloid Polym. Sci.* 1989, 267, 687–701.
- [214] Stribeck, N., *Colloid & Polym. Sci.* 1992, 270, 9–16.
- [215] *Projection-slice Theorem*, 2015.
- [216] Bonart, R., *Kolloid-Zeitschrift und Zeitschrift für Polym.* 1966, 211, 14–33.
- [217] Stribeck, N., *Colloid Polym. Sci.* 2002, 280, 254–259.
- [218] Butterworth, S., *Wirel. Eng. (also Call. Exp. Wirel. Wirel. Eng.* 1930, 7, 536–541.
- [219] Flores, A.; Pietkiewicz, D.; Stribeck, N.; Roslaniec, Z.; Baltá Calleja, F. J., *Macromolecules* 2001, 34, 8094–8100.
- [220] *Autocorrelation*, <https://en.wikipedia.org/wiki/Autocorrelation>.
- [221] Crist, B.; Morosoff, N., *J. Polym. Sci. Polym. Phys. Ed.* 1973, 11, 1023–1045.
- [222] Stribeck N., in Cebe, P.; Hsiao, B. S.; Lohse, D. J., eds., *Am. Chem. Soc. Symp. Ser.*, vol. 739 of *ACS Symposium Series*, American Chemical Society, Washington, DC, 2000 pp. 41–56, pp. 41–56.
- [223] Li, Y.; Gao, T.; Chu, B., *Macromolecules* 1992, 25, 1737–1742.
- [224] Ylgör, E.; Ylgör, I.; Yurtsever, E., *Polymer*. 2002, 43, 6551–6559.
- [225] Pichon, P. G.; David, L.; Meechin, F.; Sautereau, H., *Macromolecules* 2010, 43, 1888–1900.
- [226] Galambos, A. F., *Ph.D. thesis* 1990.
- [227] Stribeck, N.; Nöchel, U.; Funari, S. S.; Schubert, T., *J. Polym. Sci. Part B Polym. Phys.* 2008, 46, 721–726.

- [228] Stribeck, N., *TOPAS*, <http://www.chemie.uni-hamburg.de/tmc/stribeck/downloads.htm>.
- [229] Stribeck, N., in *Nano- Micromechanics Polym. Blends Compos.*, Carl Hanser Verlag GmbH & Co. KG, 2009 pp. 267–299, pp. 267–299.
- [230] Buhmann, M. D., *Acta Numer.* 2000 2000, 9, 1–38.
- [231] Vonk, C. G., *J. Appl. Crystallogr.* 1973, 6, 81–86.
- [232] Ruland, W., *J. Appl. Crystallogr.* 1971, 4, 70–73.
- [233] Rathje, J.; Ruland, W., *Colloid Polym. Sci.* 1976, 254, 358–370.
- [234] Stribeck, N.; Li, X.; Eling, B.; Pösel, E.; in't Veld, P. J., *J. Appl. Crystallogr.* 2015, 48, 313–317.
- [235] Stribeck, N.; Camarillo, A. A.; Bayer, R. K., *Macromol. Chem. Phys.* 2004, 205, 1463–1470.
- [236] Zeinolebadi, A.; Stribeck, N.; Vuluga, Z.; Schloen, C.; Botta, S.; Sari, M. G., *Polym. Adv. Technol.* 2013, 24, 693–704.
- [237] Li, X.; Stribeck, N., *Manuscript* 2015.
- [238] Stribeck, N.; Li, X.; Kogut, I.; Moritz, H.-U.; Eling, B.; Goerigk, G. J.; Hoell, A., *Macromol. Mater. Eng.* 2015, 300, 699–711.
- [239] Born, L.; Crone, J.; Hespe, H.; Müller, E. H.; Wolf, K. H., *J. Polym. Sci. Polym. Phys. Ed.* 1984, 22, 163–173.
- [240] Tien, Y.; Wei, K., *Polymer.* 2001, 42, 3213–3221.
- [241] Hergenrother, R. W.; Wabers, H. D.; Cooper, S. L., *Biomaterials* 1993, 14, 449–458.
- [242] Miller, J. A.; Cooper, S. L., *J. Polym. Sci. Polym. Phys. Ed.* 1985, 23, 1065–1077.
- [243] Peterlin, A., *J. Mater. Sci.* 1971, 6, 490–508.
- [244] Stribeck, N.; Li, X.; Zeinolebadi, A.; Pösel, E.; Eling, B.; Funari, S., *Macromol. Chem. Phys.* 2015, in print.
- [245] Camberlin, Y.; Pascault, J. P., *J. Polym. Sci. Polym. Chem. Ed.* 1983, 21, 415–423.
- [246] Noether, H. D., *Int. J. Polym. Mater.* 1979, 7, 57–82.
- [247] Stribeck, N.; Nöchel, U.; Funari, S. S.; Schubert, T.; Timmann, A., *Macromol. Chem. Phys.* 2008, 209, 1992–2002.
- [248] Gabriel, A., *Rev. Sci. Instrum.* 1977, 48, 1303.

List of Hazardous Substances

— — —

Index

- AFM, 5
- Ag-Behenate, 37
- Architecture, 32
- ATR-FTIR, 34
- Autocorrelation, 15, 29
- Average soft-domain height, 53

- BASF, 33
- BD, 31
- BESSY II, 35
- Bi-continuous, 5
- Bonart, 26
- Branched, 33
- Butterworth, 28

- CDF, 13, 37
- Chain extender, 31
- Chain extenders, 5
- Chemical crosslinking, 12
- Code, 41
- Companded function, 24
- Connectivity, 73, 76
- Convolution, 28
- Correlation function, 13, 17
- Critical length, 6
- Cross-correlation, 15, 29

- Debye, 13
- DESY, 34
- Dilute solution, 30
- Domain destruction, 7
- Domain orientation, 6
- Domain size, 6

- Edge effects, 28
- Edge enhancement, 20
- Edge-enhanced, 38
- Equatorial streak, 73
- Extrapolation, 37

- Failure mechanisms, 12, 78
- FFT, 25

- Fiber plane, 37
- Fiber symmetry, 37
- Fiducial marks, 35
- Form factor, 14
- Fourier Transform, 24
- Fraunhofer approximation, 24
- FTIR, 34
- Functionality, 75

- Gaussian distribution function, 22
- Ghost function, 20
- Gradient, 28

- Hand-cast, 48
- Hard segment content, 4
- Hard-domain consumption, 58
- High frequency, 27
- hL-distribution, 23
- Horizontal flip, 29
- Horizontal projection, 26
- HQEE, 31
- HSC, 33

- IDF, 13
- IDF Fitting, 22
- Injection-molded, 31
- Interconnectivity, 5
- Interference function, 18, 24
- ipyChord, 42
- Isocyanates, 5

- Lateral extensions, 75
- Long-period, 74
- Longitudinal projection, 26, 38
- Lorentz Correction, 29
- Low frequency, 27
- Low-pass Filter, 27
- Low-pass filtering, 37

- Machine-cast, 48
- Macroscopic strain, 35
- MDI, 31

Mellin convolution, 22
 Microfibril, 71
 Model-free, 15
 Moderate frequency, 27

 Network, 75
 Network-like, 7
 Nonlinear regression, 53

 Orthogonal property, 24

 Pair distribution function, 15
 PCL, 31
 Physically crosslinked, 75
 Polydispersity, 13
 Polyol architecture, 80
 Polyols, 5
 Polytetrahydrofuran, 8
 Porod, 13
 Post-annealing, 10
 Processing conditions, 5
 Projection slice theorem, 25
 Propyleneoxide, 33
 PTHF, 31
 PV-WAVE, 1
 Python, 1

 Radial-basis function, 37
 Reinhold distribution, 23
 Ribbon-like, 5, 11
 Ruland, 13

 Sacrifice, 78
 Sacrifice-and-relief, 48
 Sandwiched, 7
 Scattering invariant, 76
 Staining, 34
 Strain rate, 7
 Strain-at-break, 43
 Strain-induced crystallization, 8
 Stress relief, 75
 Stress-strain, 35
 Strobl, 13
 Structure factor, 14
 Superposition, 29

 Taut, 78
 TEM, 7, 34, 44
 Tensile test, 34
 Test bars, 35
 Thread-like, 12
 Tie molecules, 78
 TPU, 12
 TV-camera, 35

 Vertical Projection, 26
 Voids, 73
 Volume fraction, 84
 Vonk, 13

 WAXS, 34

 Yellowing, 11

Curriculum Vitae

Xuke Li

Born in May 17th, 1985; Henan, P.R. China

Work Experience.

10.2011-08.2015 Ph.D. Student at Institute for Technical and Macromolecular Chemistry, Department of Chemistry, Faculty of Mathematics, Informatics and Natural Sciences, University Hamburg

Education.

08.2008-07.2011 Studies at State Key Lab of Polymer Physics and Chemistry, Changchun Institute of Applied Chemistry, Chinese Academy of Sciences. Degree: Master of Natural Science.

08.2004-06.2008 Studies at Department of Applied Physics, School of Science, Northwestern Polytechnical University, Xi'an China. Degree: Bachelor of Science.

Research Experience.

- Relationship of Structure-and-Property of Polyurethane Elastomer Investigated by In-situ SAXS (Small-angle X-ray Scattering). (Current Thesis, 10.2011-Present)
- Crystallization of Poly(methylene-1,3-cyclopentane) Investigated by In-situ SAXS , WAXS (Wide-angle X-ray Scattering) and DSC (Differential Scanning Calorimetry). (Master Thesis, 08.2008-07.2011)
- Crystallization of Metal Alloys Melt by High-energy Laser under Ultrasound Levitation. (Bachelor Thesis, 02.2008-06.2008)

List of Publications

Journal Articles

- *Xuke Li*, Norbert Stribeck, Imke Schulz, Farhad Jokari-Sheshdeh, Elmar Pösel, Berend Eling, Günter Johannes Goerigk, Armin Hoell, Nanostructure Evolution of a Thermal-aged PTHF-segmented Polyurethane during Extension, Manuscript, 2015
- *Xuke Li*, Norbert Stribeck, IpyChord: A Python-based Package for Computing 2D Chord Distribution Function, Manuscript, 2015
- Almut Stribeck, *Xuke Li*, Ahmad Zeinolebadi, Elmar Pösel, Berend Eling, Sérgio Funari, Hand-cast Thermoplastic Polyurethanes. Nanostructure Evolution under Strain Monitored by SAXS, Macromolecular Chemistry and Physics 2015, in print
- Norbert Stribeck, *Xuke Li*, Berend Eling, Elmar Pösel, Pieter in't Veld, Quasiperiodicity and the Nanoscopic Morphology of Some Polyurethanes, Journal of Applied Crystallography 48(2) (2015), 313-317. DOI:10.1107/S1600576715000874
- Norbert Stribeck, *Xuke Li*, Igor Kogut, Hans-Ulrich Moritz, Berend Eling, Günter Johannes Goerigk, Armin Hoell, Morphological Failure Mechanisms in Tensile Tests of Crosslinked Polyurethanes with Poorly Developed Domain Structure, Macromolecular Materials and Engineering, in print, DOI:10.1002/mame.201500007
- Fabio Aquino, Norbert Stribeck, *Xuke Li*, Ahmad Zeinolebadi, Stefan Buchner, Gonzalo Santoro, Variation of PVDF Morphology due to Radial Cold Flow in a Flexible Pipe, Macromolecular Materials and Engineering 2015, Polymer Materials Science, submitted.
- Norbert Stribeck, Konrad Schneider, Ahmad Zeinolebadi, *Xuke Li*, Catalina-Gabriela Sanporean, Zina Vuluga, Stela Iancu, Monica Duldner, Gonzalo Santoro, Stephan Roth, Studying Nanostructure Gradients in Injection-molded Polypropylene Montmorillonite Composites by Microbeam Small-angle X-ray Scattering, Science and Technology of Advanced Materials, 15(2014), 015004. DOI:10.1088/1468-6996/15/1/015004

Oral Presentations

- *Xuke Li*, Norbert Stribeck: Nanostructure Evolution of TPU under Plain Strain and Cyclic Loading Monitored by In-Situ SAXS, 9th International Conference on X-Ray Investigation of Polymer Structure (XIPS 2013), 03.12-06.12.2013, Zakopane, Poland.

- *Xuke Li*, Almut Stribeck, Igor Kogut, Hans-Ulrich Moritz, Berend Eling, Elmar Poeselt, Günter Goerigk, Armin Hoell: Morphological Failure Mechanisms of Cross-linked Polyurethanes, European Polymer Federation Congress 2015 (EPF2015), 21.06-26.06.2015, Dresden, Germany.

Poster Presentations

- *Xuke Li*, Norbert Stribeck: ipyChord: a Python-based Package to Compute the Chord Distribution Function, DESY Photon Science Users' Meeting 2015, 28.01-30.01.2015, DESY, Hamburg, Germany.
- *Xuke Li*, Ahmad Zeinolebadi, Berend Eling, Stefan Botta, Norbert Stribeck: Nanostructure Evolution of TPU Under Plain Strain and Cyclic Loading Monitored by In-situ SAXS, Polymer Blends 2014, 05.03-06.03.2014, Halle, Germany.
- *Xuke Li*, Norbert Stribeck, Ahmad Zeinolebadi, Frauke Harpen, Gerrit Luinstra, Berend Eling, Stephan Botta, Nanostructure Evolution of TPU under Plain Strain and Cyclic Loading Monitored by In-situ Small Angle X-ray Scattering, DESY Photon Science Users' Meeting 2014, 29.01-31.01.2014, DESY, Hamburg, Germany.

Acknowledgments

First of all, I would like to express my most sincere gratitude to Prof. Dr. Almut Stribeck, for being an exceptional advisor. This thesis would not be a reality without her patient support. She tirelessly taught me knowledge concerning the fundamental theory of X-ray scattering, she showed me how to evaluate the SAXS data, and she taught me how to organize a research job from the basic experimental works to interpretation of data and writing a scientific manuscript. Except the academic fields, she also taught me problem-solving-oriented thinking, critical thinking, self-motivated. Her workable instructions promote me considerably.

I would like to thank Dr. Berend Eling (BASF) and Dr. Elmar Pösel (BASF) for providing samples and many helpful discussions during the cooperation. Many thanks are given Igor Kogut (TMC) and Imke Schulz (TMC) for supplying samples as well. Helpful suggestions from them facilitate to complete this thesis.

Many thanks are given to Günter Goerigk (BESSY II) and Armin Hoell (BESSY II) for experimental support at the synchrotron radiation facility. Sergio Funari, Rainer Gehrke and Stephan Botta (HASYLAB, DESY) are also acknowledged for the experimental support.

I am grateful to all of my colleagues in the University Hamburg, Dr. Ahmad Zeinolebadi, Fabio Aquino, Farhad Jokari-Sheshdeh, Almut Barck. Some Chinese students, Dr. Hui Zhao, Xiaojun Wu, Lirong He, Shaojian Lin and Jiaojiao Shang also help me a lot. You offer me strength and joy, motivation and recreation. But words can not describe my gratitude.

Finally, many special thanks are given to my family for their invaluable support.

Eidesstattliche Erklärung

Hiermit erkläre ich an Eides statt, dass die vorliegende Dissertationsschrift selbstständig und allein von mir angefertigt wurde. Sämtliche verwendete Quellen sind als solche gekennzeichnet worden.

I hereby declare on oath, that I have written the present dissertation by my own and have not used other than the acknowledged resources and aids.

Xuke Li

Hamburg den September 23, 2015

Xuke Li